TECHNISCHE UNIVERSITÄT WIEN

MedAustron

DIPLOMARBEIT

Estimation of the Single Event Upset Rate in the Dose Delivery System at MedAustron

zur Erlangung des akademischen Grades

Diplom-Ingenieur

im Rahmen des Studiums

Technische Physik

eingereicht von

Lukas Pfaffenbichler
Matrikelnummer 01527594

ausgeführt bei
EBG MedAustron GmbH
und am
Atominstitut der Fakultät für Physik der TU Wien

Betreuung
Assistant Prof. DI Dr.techn. Albert Hirtl (TU Wien / Atominstitut)
DI Dr.techn. Lukas Jägerhofer (MedAustron)

Wien, 14. Februar 2023

(Unterschrift VerfasserIn) (Unterschrift Betreuer)

Acknowledgements

At first, I want to thank EBG MedAustron GmbH, especially Lukas Jägerhofer, for enabling me to work on my thesis in the form of an internship in his team. He provided excellent support and was always able to connect me to the people with the means and knowledge needed to keep progressing. In addition to that, he managed to keep me as an intern after my initial internship, which allowed me to work on a new project in the radiation protection division. He also encouraged me to apply for a PhD position at CERN, which I am really looking forward to.

Also, I would like to thank Claudia Lenauer for her support regarding questions about FLUKA and flair, as well as the commitment and effort she put towards helping me with my thesis. Additionally, I want to thank Michael Deutsch who was able to assist me with all FLUKA, flair, and Python-related questions that I had, as well as DI Dr. Oliver Triebl of the MDS division, for the help he provided with his knowledge of both single event upsets and the dose delivery system. I also want to thank Leopold Schorn, the individuals I've already mentioned, and everyone else at MedAustron for making me feel welcome and giving me a terrific work atmosphere.

I also like to thank Prof. DI Dr. techn. Albert Hirtl from the Technical University of Vienna for his excellent supervision and his commitment to reviewing my thesis. He went above and beyond to assist me in meeting my deadline.

Special thanks go out to Sandra. She provided me with continuous love and support over the course of my studies, and she was always there to keep me motivated, calm, and focused during the final stretch.
Last but not least, I want to thank my parents. They not only provided me with moral but also generous financial support, which allowed me to put my main focus on my studies.

Abstract

MedAustron is a particle accelerator facility that uses hadron therapy for cancer treatment in humans. The gantry, an array of magnets used for beam guidance around the patient, is now integrated into the regular treatment process. New beam angles in the direction of sensitive electronics are to be commissioned for even more effective patient treatment, making it necessary to investigate the effect of the radiation on these sensitive electronics. The main concern is Single Event Upset (SEU) rates in the components of the Dose Delivery System (DDS).
An SEU can occur when high energy hadrons ($> 20\,\mathrm{MeV}$), intermediate energy neutrons ($0.2\,\mathrm{MeV}$ to $20\,\mathrm{MeV}$) or thermal neutrons ($\approx 25\,\mathrm{meV}$) deposit enough energy inside a random access memory (RAM), a field programmable gate array (FPGA) or a processor to generate a charge Q_{dep} over a threshold value Q_{crit}. This results in a bit flip, which can cause information corruption, which in turn can lead to disruptions in the beam line operation.
The DDS is responsible for steering the particle beam and cross-checking the delivered dose in real time. Although errors in this system are not critical for patient safety, they could lead to downtime of the beam line, which in turn would result in fewer treatments. For a gantry angle of 60° a radiation field of secondary particles is expected at the position of the electronics rack where the sensitive components of the DDS are located. This mixed field results from scattering of the particle beam in a steel plate above the rack, which is used as a floor of the irradiation room.
To get an estimate of the risk for an SEU, the fluence of thermal neutrons (THNs) Φ_{THN}, high energy hadrons and Weibull weighted intermediate energy neutrons, grouped under the expression high energy hadron equivalent (HEHeq), Φ_{HEHeq}, is investigated at the positions of the sensitive components using FLUKA (FLUktuierende KAskade), a Monte Carlo (MC) code environment used for simulation of particle and matter interactions. The fluences can then be used to calculate cross sections and subsequently SEU rates.
The goal is to get an understanding of the magnitude of the SEUs happening. In order to obtain the fluences, the geometry of the DDS rack is implemented with silicon region of interests (ROIs) in the places of the sensitive electronics. Literature values for SEU cross sections are used to get an estimation of the amount of SEUs occurring.
Analysis of the simulation results shows that there is a non-negligible risk of SEUs when using the gantry with energies greater than $150\,\mathrm{MeV}$ at 60°.

Zusammenfassung

MedAustron ist ein Ionentherapiezentrum, das mittels eines Synchrotrons beschleunigte Protonen und Kohlenstoffionen zur Krebstherapie bei Menschen verwendet. Im neusten Behandlungsraum wurde eine Protonen-Gantry, eine Anordnung von unterschiedlichen Magneten, installiert, welche es ermöglicht, den Teilchenstrahl um den Patienten zu bewegen. Um immer effektivere Therapiemöglichkeiten zu bieten werden neue Strahlrichtungen, und somit neue Gantry Winkel, kommissioniert. Der nächste gewünschte Winkel beträgt 60° und es wird vermutet, dass durch diesen Winkel verstärkt Streufelder von Sekundärteilchen in Elektronikbauteilen entstehen. Diese Sekundärteilchen können sogenannte Single Event Upsets (SEUs) in Komponenten der Elektronik des Dose Delivery System (DDS) auslösen und so zur Störung des Betriebs führen.
SEUs treten auf, wenn hochenergetische Hadronen (high energy hadrons (HEHs)) mit Energien von mehr als 20 MeV, Neutronen mittlerer Energie (intermediate energy neutrons (INs), 0.2 MeV to 20 MeV) oder thermische Neutronen (thermal neutrons (THNs), $\approx$ 25 meV) genug Energie in einem random access memory (RAM), field programmable gate array (FPGA) oder Prozessor deponieren, dass diese Energie eine Ladung Q_{dep} über einem Schwellwert Q_{crit} erzeugt. Diese Ladung kann zu einem Bit-Flip führen, was wiederum zur Korruption gespeicherter und verarbeiteter Daten führen kann.
Das Dose Delivery System (DDS) ist zuständig für die Lenkung des Teilchenstrahls und zur Verifizierung der applizierten Dosis und Strahlparameter in Echtzeit. Störungen in diesem System sind grundsätzlich nicht kritisch in Bezug auf Patientensicherheit, sie können aber zu unerwünschten Stehzeiten der Strahllinie und somit zu Ausfällen von Behandlungen führen.
Um abschätzen zu können, wie hoch das Risiko von SEUs ist, werden Monte Carlo (MC) Simulationen mithilfe von FLUKA (FLUktuierende KAskade), einem MC Programm spezialisiert auf die Simulation von Interaktionen von Teilchen und Materie, durchgeführt. Bei diesen Simulationen werden die Fluenzen der thermischen Neutronen, Φ_{THN}, der hochenergetischen Hadronen und der Neutronen mittlerer Energie, welche unter dem Begriff hochenergetische Hadronen und äquivalente Teilchen zusammengefasst werden, Φ_{heheq}, im Bereich der Elektronik des DDS ausgewertet. Mittels sogenannten SEU Wechselwirkungsquerschnitten kann man aus den durch die Simulationen gewonnenen Fluenzen SEU Raten berechnen.
Das Ziel dieser Arbeit ist es, eine Abschätzung der Größenordnung dieser SEU Raten zu bekommen. Dazu wird die Geometrie des Racks der DDS Elektronik mit entsprechenden Volumen zur Auswertung der Fluenzen implementiert.

Die Analyse der Simulationen ergibt, dass durch einen Gantry Winkel von 60° und Protonenenergien über 150 MeV eine nicht verlässigbare Anzahl an SEUs auftreten. Detailliertere Simulationen können bei Bedarf durchgeführt werden, um mögliche SEU Risiken besser abschätzen zu können als es im Rahmen dieser Arbeit möglich war. Diese Arbeit gibt Hinweise darauf, welche Bereiche dabei besonders zu beachten sind. Weiters wäre es auch empfehlenswert über Mitigationsmaßnahmen nachzudenken, zum Beispiel den Standort des DDS Racks zu verändern.

Contents

1 Introduction

MedAustron, a particle accelerator facility located in Wiener Neustadt, Lower Austria, uses particle beams with energies ranging from 62.4 MeV to 252.7 MeV for protons and 120 MeV/nucleon to 400 MeV/nucleon for carbon ions for cancer treatment in humans [1]. Proton and ion therapy provides the advantage of a favorable depth-dose profile, the so-called Bragg-peak, indicated by the pink and green lines in figure 1.1, compared to radiation therapy with photons, indicated in grey. This feature of allows for precise deposit of the maximum dose in a well defined region and keeps the radiation to surrounding healthy tissue to a minimum. The arrows in figure 1.1 indicate the difference in the deposited dose on the way though the tissue. As it is shown, radiation with photons results in a higher deposited dose in the surface layer of the tissue and also a higher dose beyond the tissue, whereas radiation with protons provides the maximum dose at the desired location.

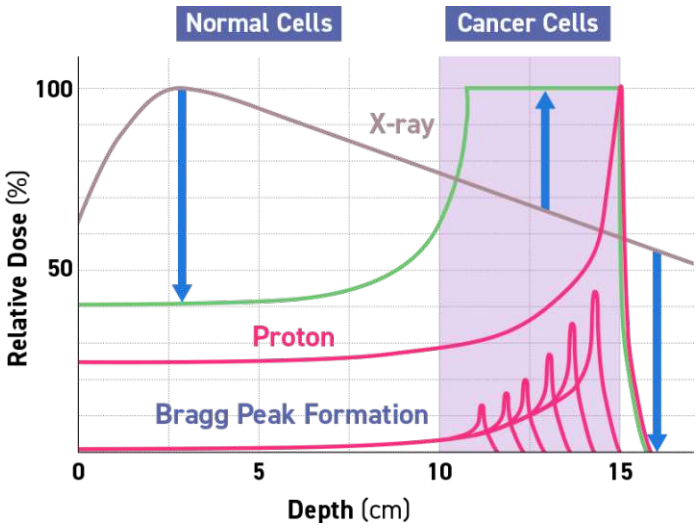

Figure 1.1: A comparison of the depth-dose profile of proton/ions and photons [2]. Radiation with protons allows for dose deposition in a well defined region, as indicated by the pink and green lines. Pink lines correspond to protons at a single energy and are used to construct the so-called spread out Bragg peak (SBOP), illustrated in green. The dose deposition achieved with photons is indicated in grey.

This depth-dose comparison is also illustrated in figure 1.2. It can be seen that, when comparing a single radiation angle, photon beams deposit the maximum amount of their energy in the surface region of the tissue whereas the proton beam deposits the maximum amount of the energy in a well defined depth. This opens up the possibility of treating cancerous tissue in hard-to-reach regions such as the brain stem, the prostate, or the spinal cord [3].

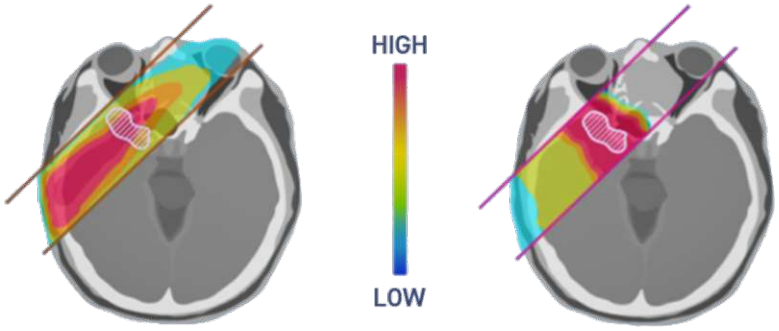

Figure 1.2: Comparison of the dose deposition of photon therapy (left) and proton therapy (right) [2]. The shaded white area indicates the treatment volume, where the maximum dose deposition is desired. Outside this volume the deposited dose should be as low as possible. When using multiple angles, dose deposition with photons can be improved.

A new proton gantry (see figure 1.3), an array of magnets that allows the guidance of the particle beam around the patient, was recently taken into operation and is now included into the regular treatment process.

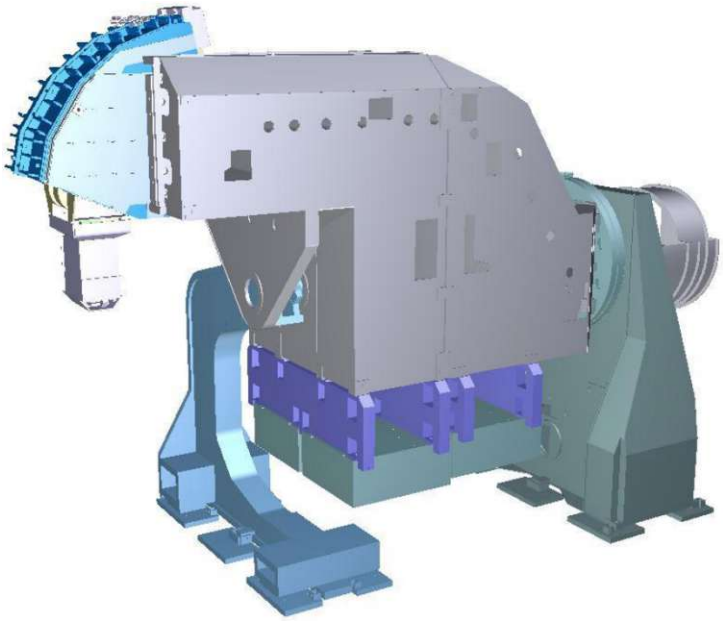

Figure 1.3: A 3D model of the gantry designed for MedAustron, based on the PSI Gantry 2 model with the beam nozzle on the left [4]. It is a construct of different types of magnets that are used to guide and focus the beam, as well as several other important components.

New beam angles are being commissioned for even more effective dose delivery to the cancerous tissue. At certain beam angles, a radiation field of protons and secondary particles is expected to be produced at the rack in which the electronics for the Dose Delivery System (DDS) are located. The DDS is responsible for steering the particle beam and cross-checking the delivered dose in real time. It consists of an ionization chamber and strip chambers, used for verifying the beam position, particle energy, and particle rate, and a rack, which contains the control elements for the system. This rack is located outside of the irradiation room below a 2.5 cm thick steel floor, slightly outside of the beam line (figure 1.4). The position of the ionization chamber in the beam line is shown in figure 1.5. The location of the rack in relation to the beam can be seen in figure 1.4a and the rack itself can be seen in figure 1.4b.

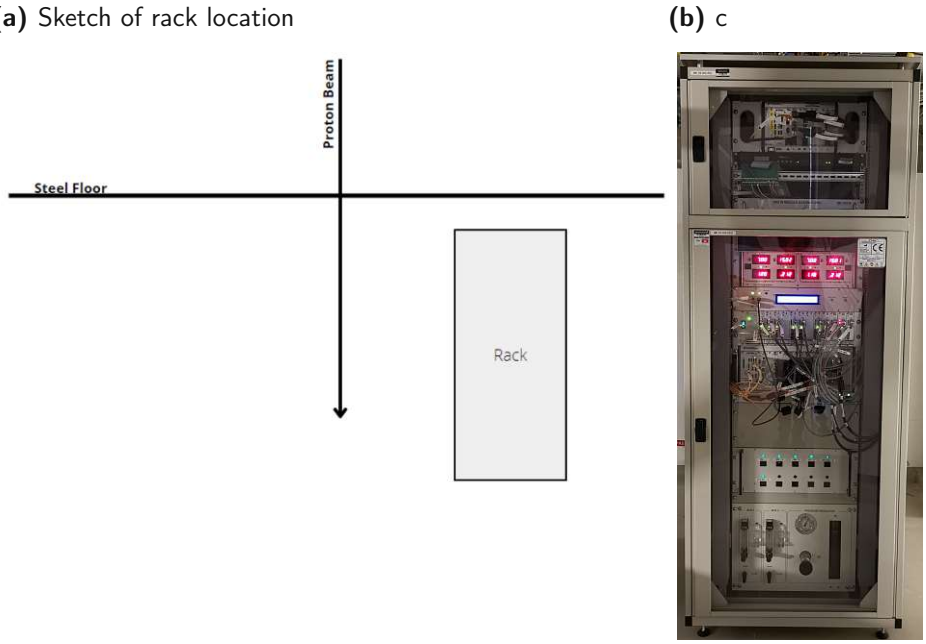

Figure 1.4: A sketch of where the electronics rack containing the control elements of the DDS is approximately located in relation to the beam origin (left) and a picture of the rack (right).

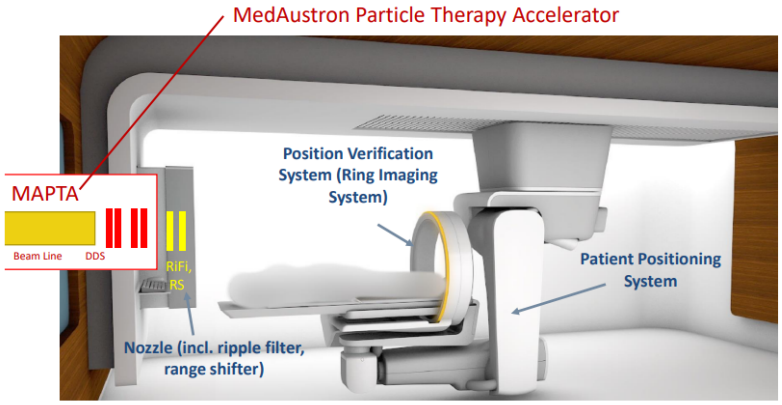

Figure 1.5: An illustration of where the ionization chamber of the DDS is located in the treatment line [5]. In this case a horizontal beam is used. The patient is positioned on the table in the center of the image which can be moved, using a 3D positioning system. Ripple filters are passive energy modulators used to broaden the Bragg peak of the beam [6]. A range shifter consists of uniform slabs of material and is used for broadening the beam and further reducing the energy of the particles [7]. The ring imaging system is a cone beam CT [8] used for verification of the patient position. The proton beam is accelerated and transported by the MedAustron Particle Therapy Accelerator (MAPTA) beam line.

Semiconductor-based electronic components, such as random access memorys (RAMs) and field programmable gate arrays (FPGAs), are increasingly susceptible to effects induced by ionizing radiation, for example single-bit flips called Single Event Upsets (SEUs). When a charged particle strikes the sensitive node in a semiconductor device, it can produce a current pulse following the ionization process that occurs [9], as illustrated in figure 1.6. This results in the necessity of studying the effects of the radiation on the electronic components used in the DDS.
Although faults in this system are not critical for patient safety, according to the Medical Device Safety (MDS) division of MedAustron [10], they can nevertheless cause downtime of the beam line, which leads to fewer patient treatments.

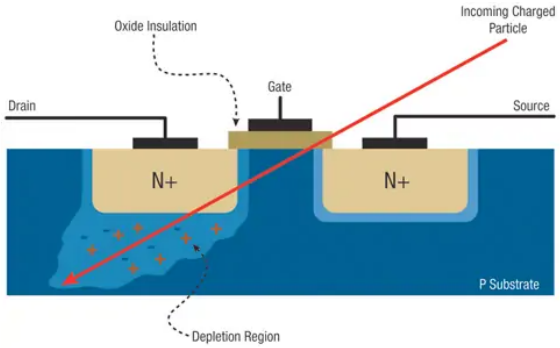

Figure 1.6: Illustration of how a charged particle can induce a charge inside a semiconductor, which is used for RAMs and FPGAs. This generated charge can in turn produce an SEU [11].

Several topics are discussed in the scope of this thesis. In chapter 2, the effects of radiation to electronics are discussed. This includes the classifications and interaction mechanisms for thermal neutrons (THNs) and high energy hadron equivalent (HEHeq) particles, as well as the process for the calculation of the cross-sections and SEU rates. In chapter 3, the tools for the simulation and calculation are introduced. Chapter 4 presents the results obtained from the simulations and calculations. Chapter 5 is focused on discussion of the simulation results. In chapter 6, a conclusion following the results achieved in the scope of this thesis is given, and an outlook for further steps is presented.

2 Physical and Technological Background

In this chapter, relevant terms used in this thesis are introduced. It includes explanations for interactions of charged particles with matter, explains terms like the particle fluence, describes different particle types and why they are important in the case of Single Event Upset (SEU) rate calculation, and gives an introduction and overview for the different types of Single Event Effects (SEEs).

2.1 Physical Background

While traversing a material, charged particles interact with the atoms of this material in different ways. These different types of interactions, as well as the terms 'particle fluence', 'high energy hadron', 'intermediate energy neutron', 'high energy hadron equivalent (HEHeq)' and 'thermal neutron', are introduced in this section.

2.1.1 Interactions of Particles with Matter

The dominant interaction processes for energy loss of charged particles in matter are Coulomb interactions with the electrons of the atomic shell, Coulomb scattering with the nucleus, and nuclear reactions, as seen in figure 2.1. In a first-order approximation, protons continuously lose kinetic energy through repeated inelastic Coulomb interactions with the shell electrons of the atoms. The interaction with the electrons does not affect the trajectory of the proton much, since its mass is much higher than that of an electron. A proton passing close to the nucleus experiences a repulsive elastic Coulombic interaction, which deflects the proton substantially due to the high mass of the nucleus. Non-elastic interactions of the proton with the nucleus are less frequent but have a more profound effect on the beam. When a proton is able to overcome the Coulomb barrier of the nucleus, it is absorbed. Due to the energy gain, the nucleus may emit a proton, deuteron, triton or other heavier ion, or even one or more neutrons. Bremsstrahlung is theoretically possible but has a negligible effect when using proton beams with therapeutic energies. Table 2.1 shows an overview of the proton interaction types, targets of the interactions, ejectiles of the interactions, the influence on the primary beam, and dosimetric effects [12].

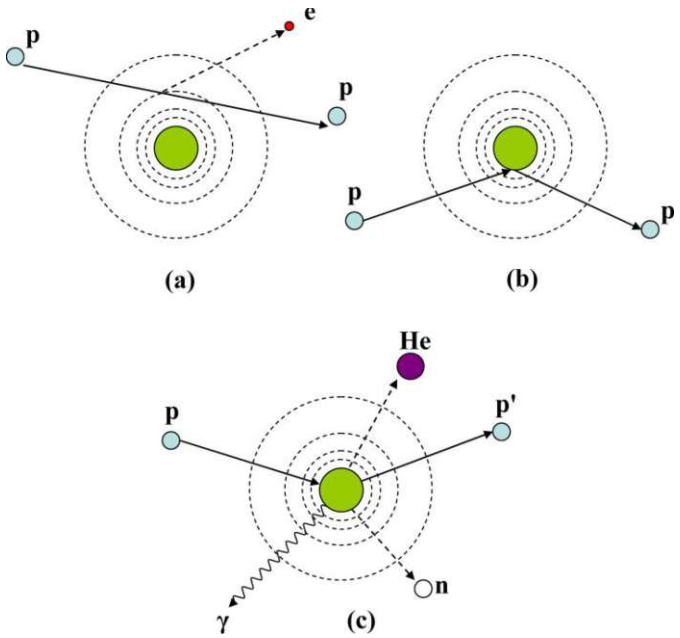

Figure 2.1: The main types of interactions for protons with matter are: a) energy loss through Coulomb interactions; b) deflection of proton trajectory through repulsive Coulomb scattering at the nucleus; c) creation of secondary particles through non-elastic nuclear interactions. e: electron, p: proton, n: neutron, He: Helium, γ: gamma rays [12].

The energy loss rate of charged particles in matter can be described by the Bethe-Bloch equation [13]

$$-\left\langle \frac{\mathrm{d}E}{\mathrm{d}x} \right\rangle = \frac{4\pi}{m_e c^2} \cdot \frac{\rho_{el} Z^2}{\beta^2} \cdot \left(\frac{e^2}{4\pi\varepsilon_0} \right)^2 \cdot \left[\ln\left(\frac{2m_e c^2 \beta^2}{I_{mat} \cdot (1-\beta^2)} \right) - \beta^2 - \frac{\delta}{2} - \frac{C}{Z} \right]. \quad (2.1)$$

The symbols in equation (2.1) are the following:

- m_e: electron mass
- Z: charge of the material
- ρ_{el}: electron density
- I_{mat}: excitation potential of the material
- c: speed of light

Interaction	Target	Ejectiles	Influence on Primary Particle	Dosimetric Manifestation
Inelastic Coulomb Scattering	Electrons of atomic shell	Primary proton, ionization electrons	Quasi-continuous energy loss	Energy loss determines range of beam in patient
Elastic Coulomb Scattering	Atomic nucleus	Primary proton, recoil nucleus	Change of trajectory	Determines lateral sharpness
Non-elastic nuclear reaction	Atomic nucleus	Secondary protons and heavier ions, neutrons, gamma rays	Removal of primary protons from beam	Primary fluence, generation of stray neutrons, generation of gammas
Bremsstrahlung	Atomic nucleus	Primary proton, Bremsstrahlung photon	Energy loss, change of trajectory	Negligible

Table 2.1: Overview of the proton interaction types, the targets, the principle ejectiles, the influence on the projectile and some dosimetric manifestations [12].

- β: ratio of velocity of the particle to the speed of light, $\frac{v}{c}$
- ϵ_0: vacuum permittivity
- $\frac{C}{Z}$: shell correction term
- $\frac{\delta}{2}$: correction for ultrarelativistic particles

The mean energy deposited per unit length travelled by a particle $\frac{\mathrm{d}E}{\mathrm{d}x}$ is called the stopping power. The unit used is $\frac{\mathrm{MeV}}{\mathrm{cm}}$ and in general it is normalized by the material density ρ to get independence from the state of the matter. This leads to a quantity called mass stopping power or linear energy transfer (LET) [14]

$$\mathrm{LET} = -\frac{1}{\rho}\frac{\mathrm{d}E}{\mathrm{d}x}\,. \tag{2.2}$$

Bragg Peak

The graph of the LET as a function of the thickness of an absorber is called the Bragg Curve, seen in the red curves in figure 2.2. This curve attributes its distinct shape to the main factors influencing the energy loss, which are the square of the nuclear charge Z^2 and the inverse square of the particle velocity β^{-2}. These factors are responsible for giving the curve its significant peak right before the particle is stopped. This peak is the reason why radiation therapy with ions is advantageous compared to therapy using X-rays [15].

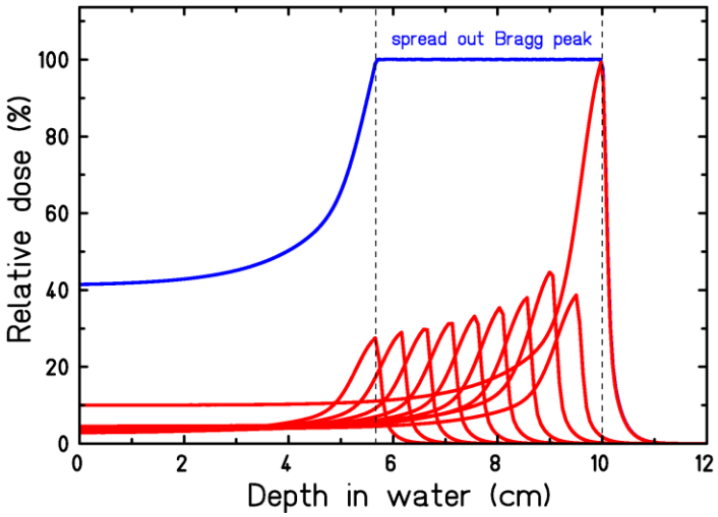

Figure 2.2: The superposition of the red Bragg Curves, meaning using particles of different energies, leads to the formation of a so-called spread out Bragg peak (SBOP), shown in blue. This SBOP allows for dose deposition in a larger region [16].

Range of Ions in Matter

The Bethe-Bloch equation describes the energy loss of charged particles in small distance increments $\mathrm{d}x$. At a certain distance, however, the particle has lost all of its energy and is stopped in the target material. This distance, also referred to as the particle range, can be described by the continuous slowing down approximation (CSDA) [17]

$$R_{\mathrm{CSDA}} = \int_0^L \mathrm{d}x = \int_{E_0}^0 \left(-\frac{\mathrm{d}E}{\mathrm{d}X}\right)^{-1} dE = \int_{E_0}^0 \left(\frac{1}{S(E)}\right) \mathrm{d}E. \tag{2.3}$$

Equation (2.3) however, only describes the mean range for a particle with initial energy E_0. Due to fluctuations in the energy loss, as well as elastic and inelastic reactions, not every particle will stop at the exact same range. This effect, also known as range straggling, is illustrated figure 2.3.

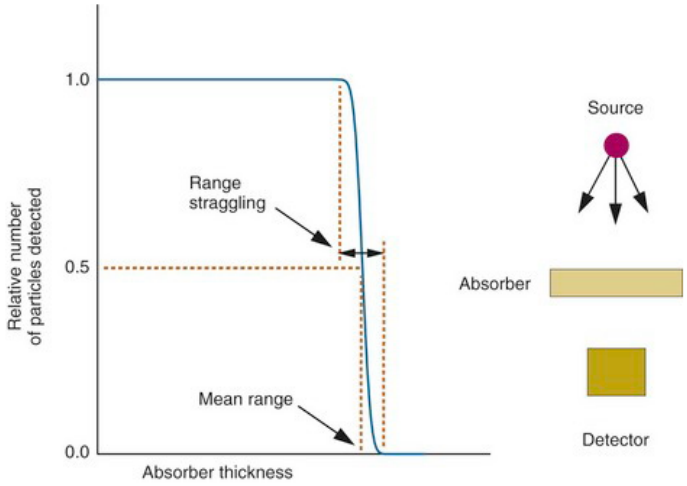

Figure 2.3: The relative number of particles in the detector over the thickness of an absorber with range straggling illustrated [18].

Interactions with the Atomic Shell

Interactions with electrons in the atomic shell lead to the ionization or excitation of the atoms. The collisions with electrons dominate the energy loss of charged particles through matter up to a few MeV for electrons and positrons, up to a few GeV for muons and up to even higher energies for charged hadrons. A charged particle will undergo many collisions with electrons an will lose a substantial amount of energy due to this [19].

Elastic Nuclear Reactions

Elastic scattering with the nucleus of an atom is called Rutherford or Coulomb scattering [20]. Multiple interactions can result in a substantial change of direction of travel proportional to the length traveled in the material. This Multiple Coulomb Scattering phenomenon is described by the theory of Molière [21] and illustrated in figure 2.4.

Inelastic Nuclear Reactions

In addition to the already mentioned interactions, a proton can interact with the nucleus non-elastically. This kind of interaction transforms the nucleus irreversibly by absorbing

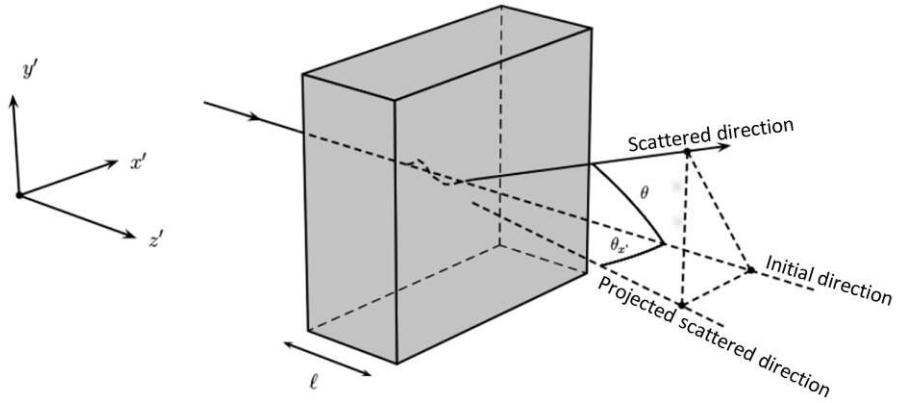

Figure 2.4: Multiple Coulomb scattering: Change of trajectory of a proton travelling though an absorber with thickness l [22]. Θ denotes the scattering angle in relation to the initial direction of the proton and $\Theta_{x'}$ denotes the projection of this angle onto the x'-z' plane.

a proton and possibly emitting a neutron. The absorption of protons leads to a small decrease in the delivered dose due to the missing primary particles, though most of this effect is compensated by the liberation of secondary protons and other ions [12]. This process of a proton being lost in the nucleus of an atom is called fluence loss. It leads to the production of secondary particles like neutrons, recoil nuclei, and secondary protons, while the de-excitation of the nucleus can also lead to the production of photons [23].

Coulomb Barrier

The minimum energy required by two nuclei for nuclear reactions to occur is referred to as the Coulomb barrier. For a nuclear reaction, the nuclei need to get close enough to overcome the Coulomb force. Since they are electrically neutral, neutrons are not affected by the Coulomb barrier and can potentially initiate a nuclear reaction at lower energies compared to protons. The Coulomb potential is given by [24]

$$U_{\text{coul}} = k\frac{q_1 q_2}{r} = \frac{1}{4\pi\epsilon_0}\frac{q_1 q_2}{r} = k\frac{Z_1 Z_2 e^2}{r}, \tag{2.4}$$

where $k = 8.9876 \times 10^9 \, \frac{\mathrm{N\,m^2}}{\mathrm{C^2}}$ is the Coulomb constant, ϵ_0 is the permittivity of free space, q_1 and q_2 are the charges of the interacting particles, Z_1 and Z_2 are the atomic numbers, and r is the interaction radius. The Coulomb barrier in the non-elastic cross section for a proton-silicon interaction can be seen in figure 2.5. The plot is produced using the

Evaluated Nuclear Data File (ENDF) library, which is a core nuclear reaction database containing recommended, evaluated cross sections, spectra, angular distributions, fission product yields, photo-atomic and thermal scattering data, with emphasis on neutron induced reactions [25].

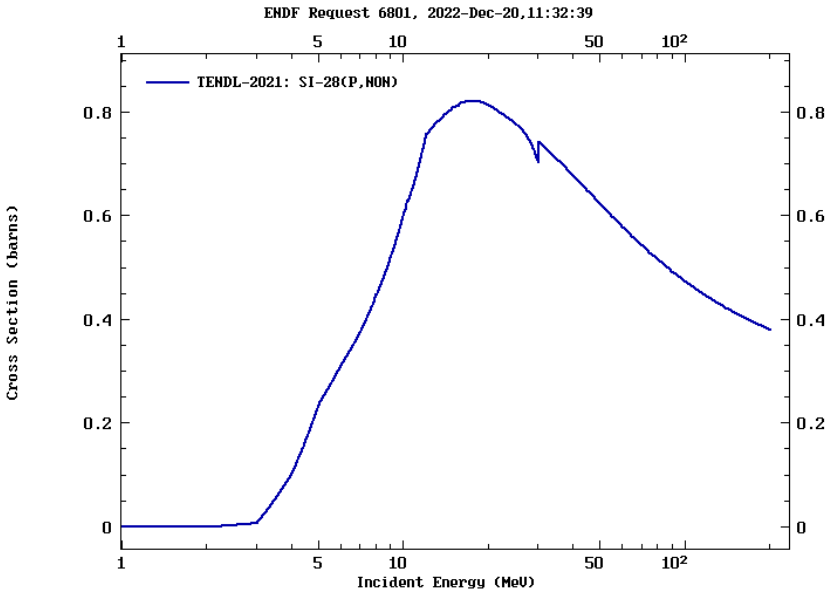

Figure 2.5: The inelastic cross section of a proton-Si interaction which shows the highest value at about 20 MeV[25]. The minimum energy required for inelastic interaction is around 4 MeV and illustrates the Coulomb barrier.

2.1.2 Particle Fluence

The average distance travelled by a particle inside a material before interacting with it is called the mean free path λ. The inverse of this quantity is called the macroscopic cross section Σ and describes the interaction probability per unit distance. These two quantities are material dependent as well as dependent on the energy and the particle type. The following derivation for the fluence is based on [26]. For N identical particles the number of interactions R happening in a given time interval is proportional to the distance travelled l times the interaction probability per unit distance Σ, written as

$$R = N \cdot \Sigma \cdot l. \tag{2.5}$$

From equation (2.5) the time derivative can be formed, defining the reaction rate

$$\frac{\mathrm{d}R}{\mathrm{d}t} = \dot{R} = N \cdot \Sigma \cdot \frac{\mathrm{d}l}{\mathrm{d}t} = N \cdot \Sigma \cdot v, \tag{2.6}$$

where v denotes the average particle velocity. The average particle density at position r is $n(r, v) = \frac{\mathrm{d}N}{\mathrm{d}V}$ and the reaction rate inside a volume element $\mathrm{d}V$ is found to be

$$\frac{\mathrm{d}\dot{R}}{\mathrm{d}V} = n(r, v) \cdot v \cdot \Sigma. \tag{2.7}$$

$\dot{\Phi} = n(r, v) \cdot v$ is a quantity called flux density or fluence rate with dimensions of $[\frac{1}{\mathrm{m}^3}\frac{\mathrm{m}}{\mathrm{s}}]$ which is equal to $[\frac{1}{\mathrm{m}^2\,\mathrm{s}}]$. The particle fluence is obtained through the time integral of the fluence rate and reads as

$$\Phi(r, v) = n(r, v)\,\mathrm{d}l. \tag{2.8}$$

In practice, two definitions for the particle fluence Φ are used today. For the first, which is used in Monte Carlo (MC) simulations, the fluence is measured as the length of the track segments contained within a sampling volume and can be written as

$$\dot{\Phi}(v)\,\mathrm{d}t = \frac{\mathrm{d}N(v)}{\mathrm{d}V}\,\frac{\mathrm{d}l(v)}{\mathrm{d}t}\,\mathrm{d}t = \lim_{\Delta V \to 0} \frac{\sum_i l_i(v)}{\Delta V}. \tag{2.9}$$

This definition allows for the scoring of the particle fluence in small volumes of any shape [26], which is why it is used in MC-codes like FLUKA.
A second definition, not to be confused with the MC definition, is the amount of particles $\mathrm{d}N$ crossing a small sampling sphere of area $\mathrm{d}A$ according to the International Commission on Radiological Units and Measurements (ICRU), defined as

$$\Phi = \frac{\mathrm{d}N}{\mathrm{d}A} \tag{2.10}$$

and visualized in figure 2.6 [27]. This definition is not used for fluence calculation in the methods applied in this thesis.

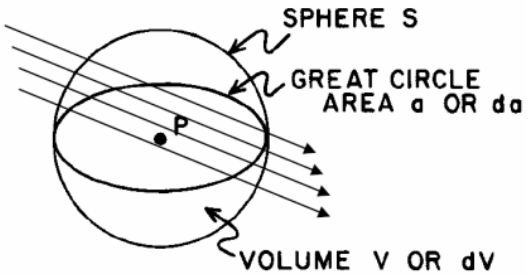

Figure 2.6: Visualisation of the definition of the particle fluence according to ICRU [27].

In figure 2.7 a particle fluence spectrum with the relevant regions regarding Single Event Upsets (SEUs), such as thermal neutrons (THNs) and high energy hadrons (HEHs), is

presented. The space in between these two regions is called the intermediate energy neutrons (INs) and they are weighted by specific factor related to their energy. The IN fluence and HEH fluence are then usually combined to form the so-called high energy hadron equivalent (HEHeq) fluence.

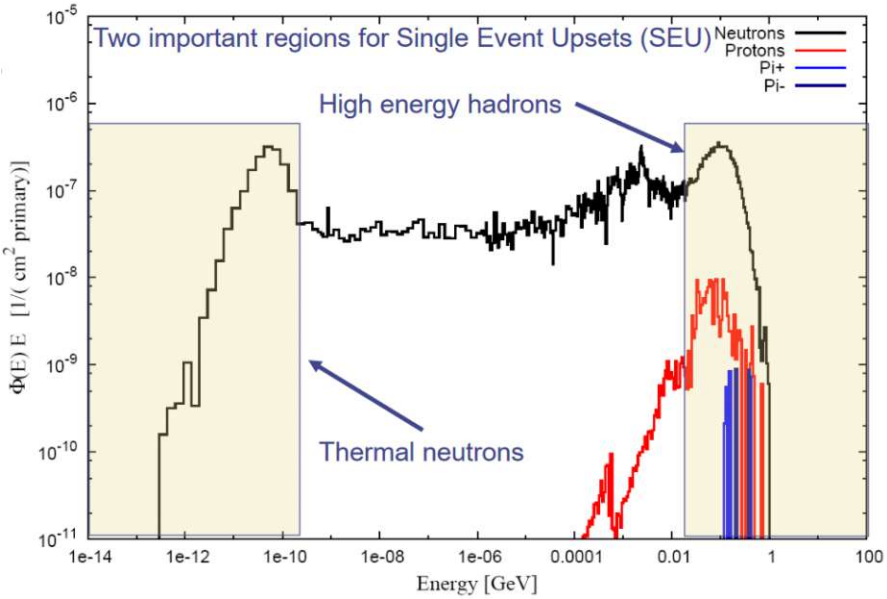

Figure 2.7: Plot of the relevant particle fluences with regards to SEUs. The image is taken from the FLUKA Advanced course [28].

2.1.3 High Energy Hadrons

Subatomic particles composed of quarks and anti-quarks are referred to as hadrons. According to their composition, they form protons, neutrons, pions and kaons.
High energy hadrons (HEHs) are defined as hadrons with energies above 20 MeV. Above this energy all hadrons are considered equally effective in inducing SEUs due to their similar inelastic cross sections in silicon [29, 30]. Resulting from this, a constant cross section for hadrons above 20 MeV can be assumed, called the saturation cross section [30]. The Single Event Effects (SEEs) induced by high energy hadrons (HEHs) are mainly due to the inelastic nuclear interactions between the particle and the material. Below 20 MeV, charged hadrons, namely protons, pions and kaons, are still able to ionize atoms because the Coulomb barrier for nuclear reactions is around a few MeV. Proton ranges are however limited at these energies, so they might not pass though the packaging of the sensitive components or the energy deposition might not be sufficient for indirect ionization [30]. Indeed, the stopping power of protons above 10 MeV is too small to directly

ionize atoms. The proton SEU cross section increases by up to a factor of 3 when the reactions transition from nuclear reactions to direct ionization.

The differential flux of hadrons above 20 MeV in units of $[\frac{\text{particles}}{\text{cm}^2\,\text{s}}]$ [26, 31, 32] can be written as

$$\phi_{\text{HEH}} = \int_{20\,\text{MeV}}^{\infty} \sum_{i=1}^{3} \frac{\mathrm{d}\phi_i(E)}{\mathrm{d}E}\,\mathrm{d}E = \int_{20\,\text{MeV}}^{\infty} \frac{\mathrm{d}\phi_{\text{HEH}}(E)}{\mathrm{d}E}\,\mathrm{d}E, \tag{2.11}$$

where i denotes the index for the different hadrons considered in the calculation process. To obtain the fluence for the HEH particles in $[\frac{\text{particles}}{\text{cm}^2}]$, the flux from equation (2.11) has to be integrated over time [26, 32], yielding

$$\Phi_{\text{HEH}} = \int_{t_0}^{t_1} \int_{20\,\text{MeV}}^{\infty} \frac{\mathrm{d}\phi_{\text{HEH}}(E)}{\mathrm{d}E}\,\mathrm{d}E\,\mathrm{d}t = \int_{t_0}^{t_1} \phi_{\text{HEH}}(E)\,\mathrm{d}t. \tag{2.12}$$

Equation (2.12) now represents the HEH fluence for the time interval $t_0 \rightarrow t_1$.

2.1.4 Intermediate Energy Neutrons

Below the 20 MeV threshold most of the SEUs are generated by neutrons. The corresponding SEU cross sections are highly energy dependent and have to be measured in special neutron facilities [33]. The flux for these particles is measured between the threshold energy E_{th}, below which the SEU cross section is considered to be zero and 20 MeV. This flux has to be weighted by a specific Weibull function [34] $w(E)$ of a reference random access memory (RAM) [30, 33]. The particle flux for these intermediate energy neutrons (INs) is described by [26, 31]

$$\phi_{\text{IN}} = \int_{E_{\text{th}}}^{20\,\text{MeV}} w(E)\,\frac{\mathrm{d}\phi_{\text{n}}(E)}{\mathrm{d}E}\,\mathrm{d}E. \tag{2.13}$$

The generic Weibull response function $w(E)$ is described by

$$w(E) = 1 - \exp\left(-\left(\frac{E - E_{\text{th}}}{W}\right)^{s}\right), \tag{2.14}$$

where E_{th} is the threshold energy, s is the shape parameter, also called the slope of the distribution, and W is the width parameter, which is responsible for spreading out the distribution. Equation (2.14) corresponds to the three parameter Weibull cumulative distribution function (CDF) [31, 34, 35] and is illustrated in figure 2.8.

As the possibility of an SEU is equally likely for HEH and IN, these two fluxes are combined to the high energy hadron equivalent (HEHeq) flux accoring to [26, 31],

$$\phi_{\text{HEHeq}} = \int_{E_{\text{th}}}^{20\,\text{MeV}} w(E)\,\frac{\mathrm{d}\phi_{\text{n}}(E)}{\mathrm{d}E}\,\mathrm{d}E + \int_{20\,\text{MeV}}^{\infty} \sum_{i=1}^{3} \frac{\mathrm{d}\phi_i(E)}{\mathrm{d}E}\,\mathrm{d}E. \tag{2.15}$$

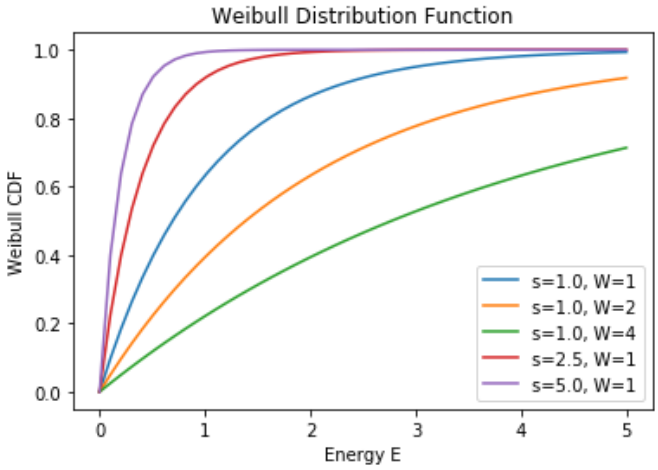

Figure 2.8: Plot of the 3-parameter Weibull cumulative distribution function (CDF) for different parameters s and W with fixed E_{th}.

To obtain the fluence in $[\frac{\text{particles}}{\text{cm}^2}]$, the flux from equation (2.15) is integrated over a time interval $t_0 \rightarrow t_1$

$$\Phi_{\text{HEHeq}} = \int_{t_0}^{t_1} \phi_{\text{HEHeq}} \, \mathrm{d}t. \tag{2.16}$$

This fluence is then used for the calculation of the SEU rate resulting from HEHeq particles.

2.1.5 Thermal Neutrons

Thermal energy neutrons, or thermal neutrons (THNs) are neutrons with energies around 25 meV. They are responsible for soft Single Event Effects, namely SEUs and Single Event Transients (SETs). One of the processes in which THNs can generate energy in silicon components is through the ^{10}B(n,α)^{7}Li neutron capture reaction $^{10}\text{B} + \text{n} \rightarrow {}^{7}\text{Li} + {}^{4}\text{He}$ [36] as seen in figure 2.9.

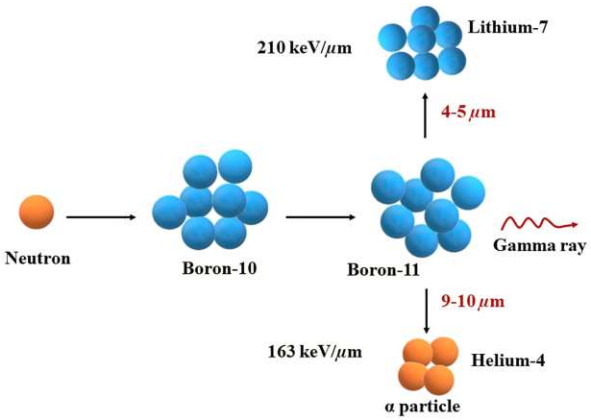

Figure 2.9: Illustration of the ^{10}B(n,α)^{7}Li neutron capture process [37]. By capturing a thermal neutron the boron nucleus is excited and decays into Li and an α-particle while sending out photons. Boron is a commonly used dopant in semiconductors.

For the THN the flux is defined in equation (2.17). It is the product of the differential neutron flux ϕ_n and a weighing function w_THN, which is decreasing as the inverse square root of the energy [26, 31, 32]:

$$\phi_\mathrm{THN} = \int_0^\infty w_\mathrm{THN}(E)\,\frac{\mathrm{d}\phi_\mathrm{n}(E)}{\mathrm{d}E}\,\mathrm{d}E = \int_0^\infty \sqrt{\frac{0.025\,\mathrm{eV}}{E[\mathrm{eV}]}}\,\frac{\mathrm{d}\phi_\mathrm{n}(E)}{\mathrm{d}E}\,\mathrm{d}E. \tag{2.17}$$

As with the HEHeq fluence, the THN fluence as seen in equation (2.18) is calculated by integrating the flux from equation (2.17) over the time interval $t_0 \to t_1$:

$$\Phi_\mathrm{THN} = \int_{t_0}^{t_1} \phi_\mathrm{THN}\,\mathrm{d}t. \tag{2.18}$$

The fluences for HEHeq particles from equation (2.16) and THN from equation (2.18) are each multiplied by the corresponding SEU cross sections and added up to calculate SEUs rates in sensitive components, as will be shown in section 2.2.3.

2.2 Radiation Effects in Electronics

Radiation effects on electronics are an important research topic due to the inherent downsizing of the components. The smaller sizes make them more and more susceptible to radiation-induced effects. In general, the damage mechanisms from radiation to electronics can be classified into two categories: cumulative effects and SEEs which are explained in the following sections. In figure 2.10 the different effects are shown.

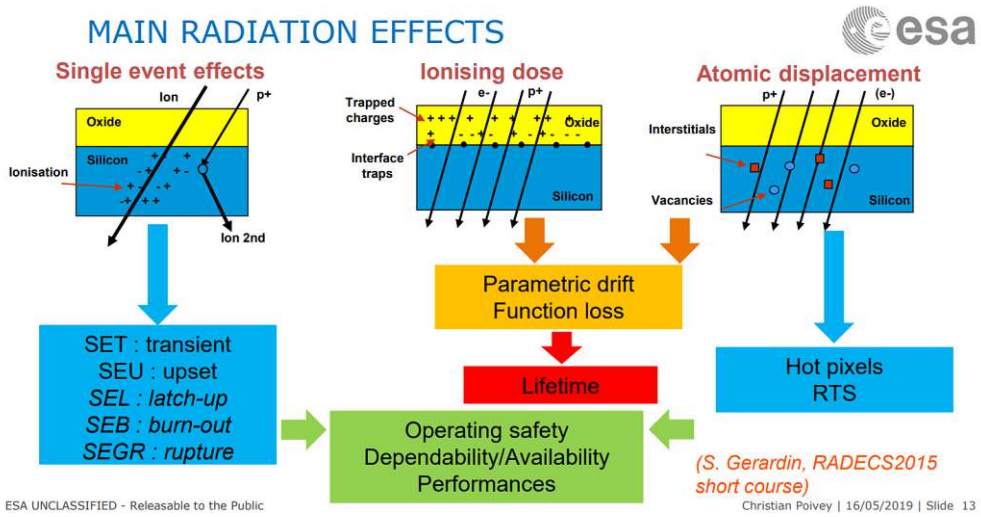

Figure 2.10: An overview of the different radiation effects by the European Space Agency (ESA) [38]. The total ionizing dose and the atomic displacement are classified as cumulative effects. An overview for the definitions of the Single Event Effects is found in table 2.3.

2.2.1 Cumulative Effects

Continuous exposure to radiation during the active lifetime of electronics leads to cumulative effects. These effects include permanent damage, which results in the components getting out of specification. For cumulative effects, the only fix is to exchange the components. Cumulative effects include the total ionizing dose (TID) and displacement damage (DD).

2.2.1.1 Total Ionizing Dose

Charged particles and photons can ionize the atoms of a material when they penetrate it. They can interact with the electrons in the atomic shell, which can be considered as an electron-hole pair creation process in semiconductors. To describe this effect, the term

total ionizing dose (TID) is used. The main concern with the TID is the degradation and performance deterioration of the circuits affected by the radiation which can lead to malfunctions and a system failure.
As the TID is the cumulative effect of the LET, the value for the TID is obtained by multiplying the LET by a constant (k =1.602 $\times$ 10^{-4} $\frac{\text{Gy mg}}{\text{MeV}}$ [31]) to convert it from eV to J and the fluence Φ

$$TID = k \cdot LET \cdot \Phi. \tag{2.1}$$

Commonly, the unit used to present the TID is Gray [Gy], which replaced the old unit radiation absorbed dose [rad].
The main factor of the TID is that it alters the conductive properties of the material. These alterations can be seen, for example, as increased leakage current and threshold voltage shifts. In semiconductors used for microelectronics, defects resulting from TID result in the accumulation of trapped charges in the oxide layers of the components. Electron-hole pairs formed in the material (e.g., SiO_2) by ionization may not all recombine. Some move due to the applied electric field, and due to their higher mobility, electrons might be able to exit the oxide layer into the bulk material where they can recombine with holes. This leads to trapped holes in defect centers in the oxide, which impact the properties of the component negatively [39, 40].
The device degradation by TID includes:

- **Increased leakage current:** In n-channel (NMOS) transistors, the free leakage paths and the interface can be reversed due to the generation of charges in the semiconductor. This results in parasitic leakage currents, which lead to increased power consumption and degraded timings.
- **Threshold voltage shifts:** The threshold voltage V_{th} of a MOSFET is the minimum gate-to-source voltage needed in order to create a conducting path. When exposed to radiation, V_{th} can be lowered, which leads to errors in operation.

2.2.1.2 Displacement Damage

In general, all structural damage to the crystal lattice of a device caused by high-energy particles is called displacement damage (DD). It is defined as the total energy deposited through all non-ionizing processes.
The DD is the cumulative effect of the non-ionizing energy loss (NIEL), a physical quantity that describes the total non-ionizing energy loss as a particle travels though a medium. This quantity is useful for prediction of the radiation damage and therefore the prediction of the lifetime of components exposed to radiation [41]. By transferring their momentum to the atoms and displacing them from their position in the crystal lattice, high-energy particles create vacancies and interstitials or so-called Frenkel-pairs. The number of produced Frenkel-pairs is referred to as the number of displacements, and

their density is called the displacement per atom (DPA) [42]. When the energy of the incoming particle is high enough, it can displace several atoms at once, and the displaced atoms can also displace other atoms, resulting in a displacement cascade. An explanation for the effects of the energy transfer to an atom in a crystal lattice is illustrated in figure 2.11.

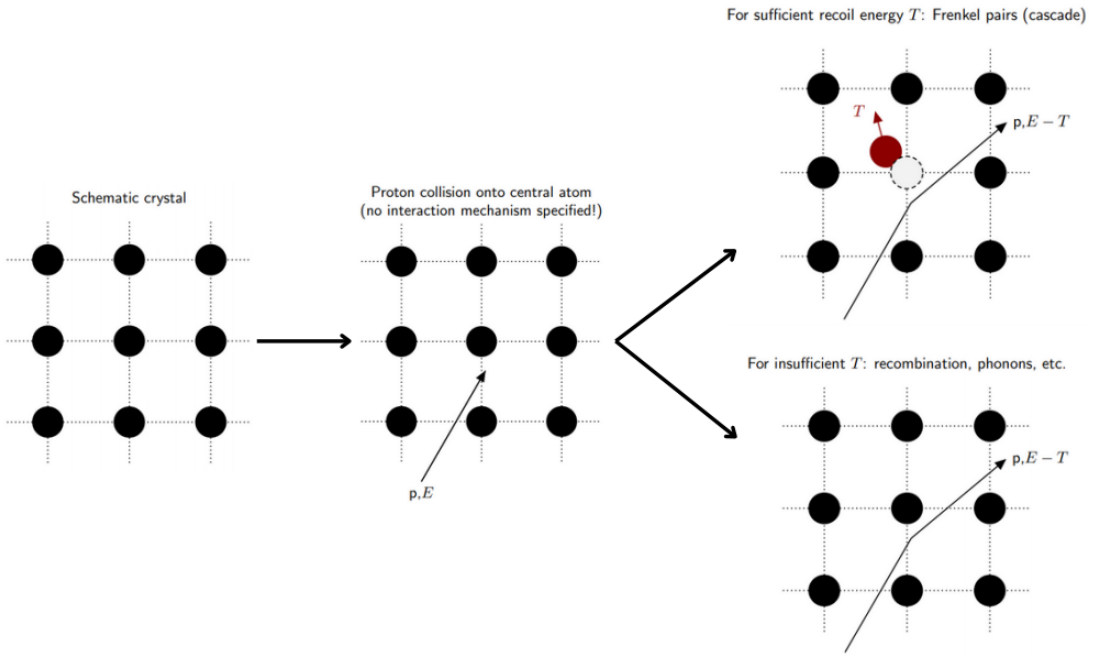

Figure 2.11: An explanation of the displacement damage by showing the effects on an atom in a crystal lattice. When a proton collides with the atoms in a crystal lattice two distinctions have to be made. The first case is that the proton carries sufficient recoil energy T to dislocate an atom of its lattice position, resulting in so-called Frenkel pairs. For insufficient recoil energy, the atom remains in its position and the proton is scattered on its way though the absorber [43].

Some of the effects occurring due to DD are:

- **Gate-oxide breakdown:** The accumulation of DD defects might lead to a short circuit in the insulating layer of the gate oxide bulk in some extreme cases. This could lead to the destruction of the structure due to the heat.
- **Gain degradation:** DD creates recombination centres which leads to a decreased lifetime of some charge carriers. This increases the necessary input bias current, leading to a reduction in gain.

- **Charge traps and hot pixels in camera sensors:** DD affects image sensors in particular. Defect clusters in the pixel array can act as regions with increased dark signal in some cases. This dark signal leads to distinct bright spots in images. Defects can also act as traps for photogenerated charges in some cases, reducing the charge transfer efficiency and leading to signal streaks in the image.

The number of Frenkel-pairs can be estimated as a function of the threshold energy E_{th} and the recoil energy T of the atom. For different materials the damage threshold energy E_{th} varies and can be seen for some selected materials in table 2.2.

Material	E_{th} **[eV]**
Li	10
Graphite	30-35
C	20
Si	25
Cu	30-40
Pb	25

Table 2.2: Values for E_{th} for different material from [43]. In this thesis only the value for Si is of interest.

A rough estimate of the number of produced Frenkel-pairs can be made according to Kinchin-Pease [43, 44]

$$N_{\text{F}} = \frac{T}{E_{\text{th}}}\Theta(T > E_{\text{th}}). \tag{2.2}$$

A better estimation is achieved by using the industry standard by Norgett, Robinson and Torrens [43, 45]

$$N_{\text{NRT}} = \kappa L(T)\frac{T}{2E_{\text{th}}}. \tag{2.3}$$

In equation (2.3) $\kappa = 0.8$ and is called the defect efficiency while $L(T)$ measures the fraction of T that goes into nuclear stopping [43]. For operational definition of the DD the unit DPA is used as an indicator. The number of Frenkel-pairs is related to the DPA by the relation [43]

$$DPA = \frac{1}{\rho}\sum_i N_i N_{\text{F},i}, \tag{2.4}$$

where N_i is the number of projectiles per unit volume with interaction type i, $N_{\text{F},i}$ is the number of Frenkel-pairs resulting from interaction type i and ρ is the number of target atoms per unit volume. To help with interpretation, a factor of 0.01 DPA means that 1 out of 100 atoms is displaced.

2.2.2 Single Event Effects

A Single Event Effect (SEE) is a stochastic effect that can result, as the name indicates, even from a single particle depositing energy in the sensitive volume of a device. This class of radiation effects is not cumulative and can occur anytime when a device is exposed to radiation. In the collective class of SEEs there is the distinction between hard errors and soft errors. Hard errors are destructive effects where an event leads to permanent physical damage. Soft errors are non-destructive and can be corrected by a re-write of the information or restart of the system [26, 31, 46–48].
The fundamental SEE process works as following [49]:

1. **Charge generation:** An incident particle interacts with the material and produces free charge carriers (electrons and holes).
2. **Charge recombination and collection:** The charge carriers move by diffusion and drift through the material to a sensitive node while also recombining.
3. **Circuit response:** The additional charge on the node alters the voltage that ultimately leads to SEEs. Voltage glitches can propagate throughout a circuit.

Charge Generation:

The interactions between the incident particle and the material can be classified in three groups:

1. Elastic Coulomb scattering between the incident particle and the electrons of the target material
2. Elastic Coulomb and nuclear scattering between the incident particle and the nucleus of the target material
3. Inelastic scattering between the incident particle and the nucleus of the target material

Charge recombination and collection:

The mechanisms responsible for charge movement are charge drift described by Ohm's law [50]

$$J_{\text{drift}} = q \cdot n \cdot \mu_q \cdot E \tag{2.5}$$

and charge diffusion described by Fick's law [51]

$$J_{\text{diffusion}} = \pm q \cdot D \cdot \frac{\mathrm{d}n}{\mathrm{d}x}\,. \tag{2.6}$$

In equation (2.6) the $\pm$ is the distinction between electrons and holes and D is the diffusion coefficient, which can be written as

$$D = \frac{k_B \cdot T \cdot \mu_q}{q}, \tag{2.7}$$

also known as the Einstein-Smoluchowski equation [52]

In equations (2.5) - (2.7), q is the electron charge, n is the number of electrons/holes per cm^3, μ_q is the mobility of the electrons/holes in $\frac{\mathrm{cm}^2}{\mathrm{V\,s}}$, E is the electric field intensity in $\frac{\mathrm{V}}{\mathrm{cm}}$, k_B is the Boltzmann constant and $\frac{\mathrm{d}n}{\mathrm{d}x}$ is a concentration gradient.
The recombination processes of electrons and holes are Shockley-Read-Hall recombination and Auger recombination, which occur at the same time [53, 54].

Circuit Response:

The system reacts to the generated voltage spike. In sequential elements, a bit-flip can occur if the spike is high enough. Logic gates used for combinational logic elements, like AND-, OR- and NOR-gates[1], can be effected by the strike of an ionizing particle, which in turn can affect other combinational and sequential element further ahead in the circuit (see figure 2.12). This can lead to the storage of wrong information [49, 56, 57].

[1] A NOR-gate is a sort of electronic logic gate. A HIGH (1, true) output is achieved, if both inputs to the gate are LOW (0, false). A LOW output is obtained, if one or both inputs have a HIGH signal [55].

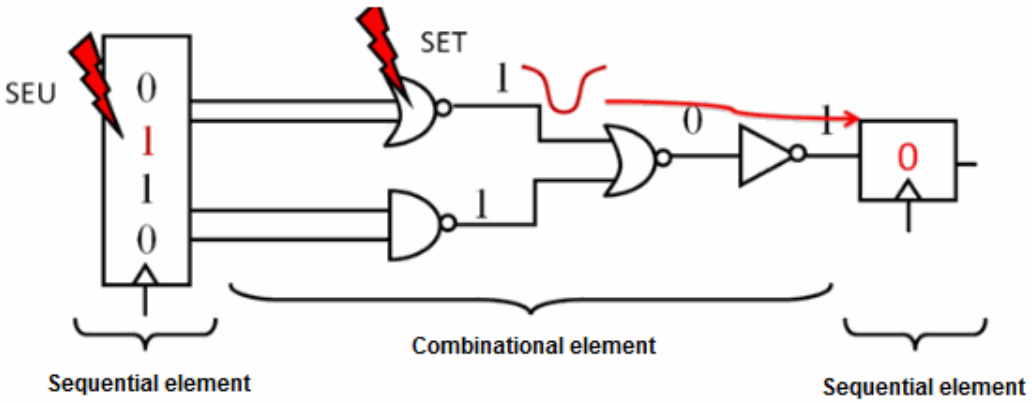

Figure 2.12: The effects of an ionizing particle spike on a circuit. A strike of an ionizing particle in a sequential element, shown on the far left, can induce a bit flip or SEU in this register, altering the stored information. When striking a combinational element, as illustrated by a strike in a NOR-gate, a transient pulse is produced at the output, which can be propagated to the next sequential element, resulting in a wrong stored logical value. This is called a Single Event Transient (SET) [56, 57].

An overview of the different types of SEEs including their descriptions, is presented in table 2.3.

	SEE	Abbreviation	Description
Soft Errors	Single Event Upset	SEU	Single bit flip in a memory, can be restored by rewriting the information. No permanent damage to the device is produced.
	Single Event Functional Interruption	SEFI	Like a SEU but in an important register of a microprocessor or field programmable gate array (FPGA). Leads to interruption of the proper operation of a circuit.
	Single Event Transient	SET	Voltage/Current pulse in the node of combinational logic. Error can be propagated in digital devices.
	Multiple Cell Upset	MCU	Same mechanism as SEU but with multiple bit flips in different memory cells.
	Multiple Bit Upset	MBU	Similar to MCU but the multiple bit flips occur in the same memory cell.
Hard Errors	Single Event Latch-up	SEL	The particle can turn on a parasitic structure in an integrated circuit. The transistors keep each other saturated until a system power-down.
	Single Event Gate Rupture	SEGR	A rupture of the gate oxide in a power MOSFET.
	Single Event Burnout	SEB	The activation of a parasitic bipolar junction transistor (BJT) which leads to an abrupt increase of the current and subsequent failure of the device.

Table 2.3: Overview over the different types of SEEs due to radiation to electronic components [26, 31, 46–48]. This thesis focuses on SEUs in random access memorys (RAMs) and FPGAs.

Field programmable gate arrays (FPGAs) can roughly be divided into two sub-categories, flash-based logic arrays using nonvolatile memory cells, and static RAM (SRAM)-based FPGAs using SRAM cells to store their configuration patterns, which are transferred to the FPGA upon power-up. Figure 2.13 shows the result of an alpha particle striking the routing matrix of a Flash FPGA and an SRAM-based FPGA. As the figure indicates, flash FPGAs are not susceptible to SEUs, due to the fact that the configuration data is available all the time, whereas SRAM-based FPGAs can suffer from functional failure after the hit of an ionizing particle, due to the fact, that the configuration data is only loaded on power-up.

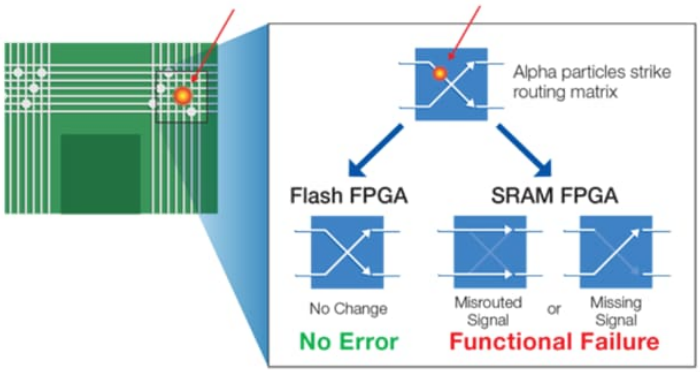

Figure 2.13: The strike of an ionizing particle in the routing matrix results in an SEE in an SRAM based FPGA but not in a flash-based FPGA [58]. Flash FPGAs use nonvolatile memories to store the configuration data, which enables them to retain the configurations. SRAM-based FPGAs only load configuration data on power-up, which makes them susceptible to configuration changes.

2.2.2.1 Single Event Upset

A change of state of a latched logic cell from $0 \rightarrow 1$ or from $1 \rightarrow 0$ due to an ionizing particle hitting a sensitive node of an electronic component (RAM, FPGA) is called a Single Event Upset (SEU). Showers of thermal neutrons, intermediate energy neutrons, and high energy hadrons can induce SEUs by interacting with the electronic circuits [59]. The interactions of HEHeq and THN with matter are discussed in the previous sections 2.1.3 to 2.1.5. SEUs are non destructive or so-called soft errors as can be seen in the overview presented in table 2.3. This means, the error can be remedied by rewriting or resetting the logic element it occurred in.

2.2.3 Single Event Upset Rate Calculation

The SEU rate can be calculated as a product of the particle cross sections σ_i and the differential particle fluences $\frac{\mathrm{d}\Phi_i(E)}{\mathrm{d}E}$. It can then be calculated according to [31]

$$N_{\mathrm{SEU}} = \sum_{i=1}^{M} \int_0^\infty \sigma_i(E) \cdot \frac{\mathrm{d}\Phi_i(E)}{\mathrm{d}E} \, \mathrm{d}E. \tag{2.8}$$

As equation (2.8) shows, it is dependent on the particle types and the energy. It represents the sum over the particles of interest, denoted with the index i. The relevant particle types for SEUs in silicon-based electronic components are THN and HEHeq. This allows for the energy dependent SEU rate from equation (2.8) to be decomposed as a function of constant cross sections as follows [31]

$$\begin{aligned} N_{\mathrm{SEU}} &= \sum_{i=1}^{M} \int_0^\infty \sigma_i(E) \cdot \frac{\mathrm{d}\Phi_i(E)}{\mathrm{d}E} \, \mathrm{d}E \\ &= \int_0^\infty \sigma_{\mathrm{THN}}(E) \cdot \frac{\mathrm{d}\Phi_{\mathrm{THN}}(E)}{\mathrm{d}E} \, \mathrm{d}E + \int_0^\infty \sigma_{\mathrm{HEHeq}}(E) \cdot \frac{\mathrm{d}\Phi_{\mathrm{HEHeq}}(E)}{\mathrm{d}E} \, \mathrm{d}E \\ &= \sigma_{\mathrm{THN}} \int_0^\infty w_{\mathrm{THN}}(E) \cdot \frac{\mathrm{d}\Phi_{\mathrm{THN}}(E)}{\mathrm{d}E} \, \mathrm{d}E + \sigma_{\mathrm{HEHeq}} \int_0^\infty w_{\mathrm{HEH}}(E) \cdot \frac{\mathrm{d}\Phi_{\mathrm{HEHeq}}(E)}{\mathrm{d}E} \, \mathrm{d}E \\ &= \sigma_{\mathrm{THN}} \cdot \Phi_{\mathrm{THN}} + \sigma_{\mathrm{HEH}} \cdot \Phi_{\mathrm{HEHeq}}. \end{aligned} \tag{2.9}$$

The simplified form that is left after the rearrangement is [28, 31]

$$N_{SEU} = \sigma_{\mathrm{HEHeq}} \cdot \Phi_{\mathrm{HEHeq}} + \sigma_{\mathrm{THN}} \cdot \Phi_{\mathrm{THN}}. \tag{2.10}$$

In order to calculate the SEU rate, one needs the SEU cross sections for THN and HEHeq. The literature values used for calculation in the scope of this thesis for σ_{THN} and σ_{HEHeq} can be found in table 3.2 in section 3.3.1.

2.2.4 Cross Section Calculation

SEU cross sections for HEHeq can be calculated by [31, 60]

$$\sigma_{\text{HEHeq}} = \frac{N_{Q_{\text{dep}}>Q_{\text{crit}}}}{\Phi_{\text{HEHeq}}}. \tag{2.11}$$

The principle behind this equation is, that the particles depositing a charge Q_{dep} higher than the threshold charge Q_{crit} in the sensitive volume of the silicon components are counted. $N_{Q_{\text{dep}}>Q_{\text{crit}}}$ describes the amount of times the critical charge was deposited in the volume. This value is divided by the total fluence Φ_{HEHeq} and returns a value in dimension of [cm^2]. This cross section can then be normalized to one bit in the device, resulting in a cross section per bit [$\frac{\text{cm}^2}{\text{bit}}$].
The deposited charge Q_{dep} can be calculated using [61]

$$Q_{\text{dep}} = \frac{E_{\text{dep}}[\text{MeV}]}{22.5\,[\text{MeV/pC}]}, \tag{2.12}$$

which gives a relation between energy deposited in the sensitive volume and charge generated.

2.3 MedAustron

MedAustron is a particle accelerator facility where particle beams with energies ranging from 62.4 MeV to 252.7 MeV for protons and 120 MeV/nucleon to 400 MeV/nucleon for carbon ions are used for cancer treatment in humans [1] as well as research applications. A proton gantry, based on the design of the PSI Gantry 2 [62] is installed in irradiation room 4 (IR4) to rotate the beam around the patient. For precise dose application in the tissue, a so-called Dose Delivery System (DDS) is used to monitor and guide the beam.

2.3.1 Accelerator Line

The acceleration of the particles happens in 4 steps (figure 2.14):

1: Ion sources

2: Linear accelerator (LINAC)

3: Synchrotron

4: Extraction line

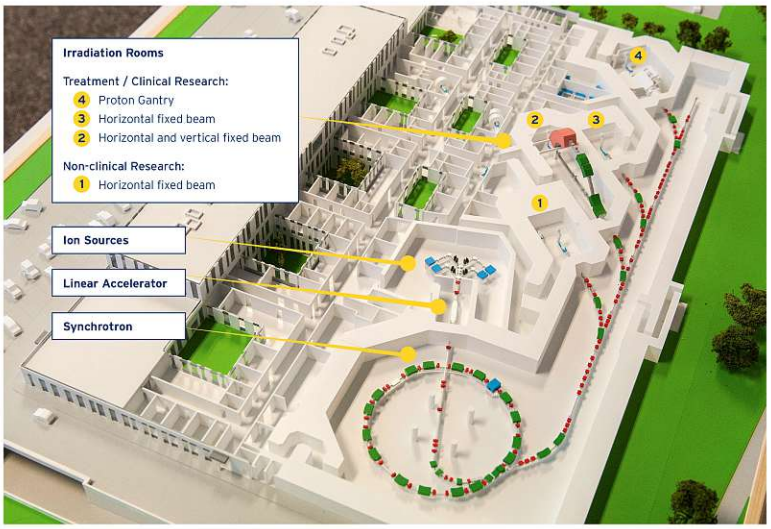

Figure 2.14: The acceleration line of the MedAustron Particle Therapy Accelerator (MAPTA) [63]. Starting from the ion sources, different types of ions are produced. After extraction they are accelerated by a LINAC. Then they are injected into the synchrotron and are accelerated until they reach the desired energies. Upon reaching this energy, the ions are extracted and transferred to the IRs through the extraction line.

At the ion sources H_3^+, C^{4+} and ^4He ions can be produced. Electron cyclotron resonance (ECR) ion sources are used and the extraction energy of the ions is 8 keV/u. After extraction they are accelerated by the LINAC to reach an energy of 7 MeV/u. Up to this point, the acceleration line is referred to as the 'low-energy beam transfer' (LEBT) section. After exiting the LINAC the ions pass a carbon foil to strip electrons off of the ions to obtain protons from H_3^+ and C^{6+} from C^{4+}. This section is called the Medium Energy Beam Transfer (MEBT). The ions are then injected into the synchrotron ring. They are bunched and accelerated by a radio frequency cavity until they reach the requested energy. After reaching the energy the ions are extracted and transported to the irradiation rooms (IRs) via the so-called extraction line. From injection until extraction the section is called High Energy Beam Transfer (HEBT) [64]. The extraction line is used to transport the accelerated particles towards the IRs 1 to 4. IR1 is equipped with a fixed horizontal beam line and dedicated to research, IR2 features a horizontal and vertical beam intersecting at a common isocenter for clinical use, IR3 has a horizontal beam and IR4 is equipped with a rotating proton gantry for flexible treatment angles.

2.3.2 Proton Gantry - Irradiation Room 4

At MedAustron, the irradiation room 4 (IR4) is the newest of the three IRs available for clinical usage and provides the most flexibility in the treatment process due to the proton gantry. The gantry is based on the design of the PSI Gantry 2 [62, 65], shown in figure 2.15, and allows for a large rotation of the beam nozzle around the patient due to its unique construction. The commissioned rotational angle of the gantry for radiation purposes is 180°. This rotation is the key to efficient tumor treatment, even in hard-to-reach places. Pictures of IR4 with the gantry can be seen in figures 2.16a and 2.16b and pictures of the gantry itself are featured in figure 2.17.

The gantry system presented in figure 2.15 consists of three dipole magnets, labeled $A_{1\text{-}3}$ and seven quadrupoles, labeled as $Q_{1\text{-}7,C}$. W_T and W_U are sweeper magnets which are essential elements used for beam scanning. W_T is used for beam displacement in the transversal direction and W_U displaces the beam in the dispersive plane. The design of the gantry is very compact, and it would be fairly difficult to further reduce the dimensions of the construction. $M_{1\text{-}3}$ are beam profile monitors, which are diagnostic elements and P are vacuum pumps. S_y is a steering magnet and $H_{1,2}$ are sextupole magnets which are also used as steering devices. X denotes the location of the X-ray tube [65].

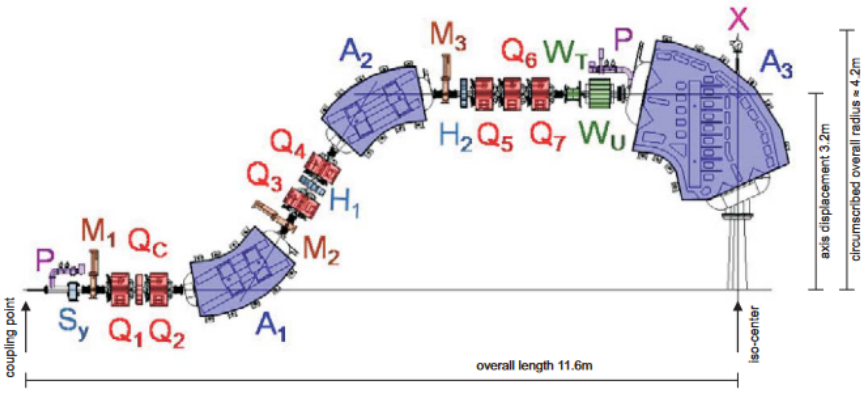

Figure 2.15: A technical drawing of the array of magnets forming the gantry used at MedAustron for proton beam guidance [66] which is based on the PSI Gantry 2 [62]. $A_{1\text{-}3}$ are dipoles, $Q_{1\text{-}7,C}$ are quadrupoles, W_T and W_U are sweeper magnets, $M_{1\text{-}3}$ are profile monitors, P are vacuum pumps, S_y is a steering magnet, $H_{1,2}$ are sextupole magnets and X is the location of the X-ray tube [65].

(a) The IR4 during the construction phase **(b)** The finished IR4 as it is now

Figure 2.16: Two pictures of the IR4 to show the implementation of the rotational angle of the beam nozzle around the patient [67]. On picture (a) IR4 is seen during the construction phase, with the last bending magnet in green above the roller shutter. In (b) the finished IR4 with the installed beam nozzle in the roller shutter and the treatment table, held by the patient positioning system is seen.

2.3.3 Dose Delivery System

In order to provide the prescribed amount of dose to the cancerous tissue, it is necessary to check and modify the lateral dose profile. New dose delivery systems are able to provide such fluence-modulated lateral dose profiles. By using monoenergetic beamlets with well-defined penetration depths, highly conformal dose distributions are achieved across the tissue [68]. A synchrotron allows for a wide range of energies and particle counts, resulting in the possibility of fully three-dimensional dose delivery. The target volume is segmented into several layers orthogonal to the direction of the particle beam and irradiated by a superposition of beamlets, each applying a distinct particle count at a well-defined position.
To perform such operations, it is necessary to have a precise, fast, accurate, and redundant[2] Dose Delivery System (DDS). It monitors the particle flux for each beamlet, requests the proper beam settings at the start of each spill, and steers the beam by controlling the steering magnets [68].

[2]The DDS is completely independent from the synchrotron. The Medical Device Regulation (MDR) (§16.2) requires reliable monitoring and control of the delivered dose, beam type, energy, and quality of radiation.

(a) The proton gantry before installation of beam line components

(b) The proton gantry with some features of the IR4 installed

(c) Gantry in a 90° position, top part is seen

Figure 2.17: Pictures of the proton gantry, which is used to guide the beam around the patient. Top pictures are from [67].

3 Material and Methods

In this chapter, the simulation method and software tools and methods for calculating the SEU rates are presented.

3.1 Monte Carlo Method

The Monte Carlo (MC) method in numerical analysis is a technique used to obtain sample values of a variable for a given problem by using a sequence of random numbers. The used calculation process is an artificial construct, usually a computer program, that represents the analyzed problem mathematically. Sample values are obtained by selecting specific numbers from appropriate ranges using probability distributions for these variables. MC calculations and experiments will give a result that is a possible or representative outcome of the modeled process. Both contain uncertainties that can often be reduced by repeated measurements and quantified using statistical analysis [69]. MC simulations converge with an efficiency of $\frac{1}{\sqrt{N}}$ compared to the converging efficiency of $\frac{1}{\sqrt[d]{N}}$ of traditional methods, where d denotes the dimension of the problem. This means that the efficiency of MC simulations is better if the dimension of the problem is greater than 2. The applications of MC simulations are widespread over several different fields, ranging from simulating physical phenomena, applications in finances and business and even in library sciences. This is due to the fact that particularly difficult mathematical problems can be solved and that the computational speeds and the memory capacity of modern computers allow extremely rapid development in all those mentioned fields [26, 70].

MC simulations in the application of radiation therapy are based on complex concepts. This section provides an overview of the underlying principles of the collision-by-collision simulation of particle transport. Two different approaches have to be considered, the analog particle transport for the case of uncharged particles like photons, and the condensed history (CH) technique for the simulation of charged particles. The content of this section is based on the book 'Monte Carlo Techniques in Radiation Therapy' [71].

3.1.1 Analog Particle Transport

When hitting the surface of a homogeneous medium, the interaction probability $p(s)$ of a photon after a path length of s is described by the attenuation law

$$p(s)\,\mathrm{d}s = \mu(E)e^{-\mu(E)s}\,\mathrm{d}s, \tag{3.1}$$

where $\mu(E)$ is the linear attenuation coefficient of the medium for photons of energy E. If the medium is extended infinitely below the surface, the mean free path length s until interaction is calculated from the probability distribution

$$\langle s\rangle = \int_0^\infty \mathrm{d}s\, s\, p(s) = \mu(E)\int_0^\infty \mathrm{d}s\, s\, e^{-\mu(E)s} = \frac{1}{\mu(E)}. \tag{3.2}$$

This allows the expression of the attenuation law in equation (3.1) in terms of the number of free path lengths

$$p(\lambda)\,\mathrm{d}\lambda = e^{\lambda}\,\mathrm{d}\lambda, \tag{3.3}$$

where λ is defined as

$$\lambda = \frac{s}{\langle s\rangle} = \mu(E)s. \tag{3.4}$$

When the number of mean free path length is defined by

$$\lambda = \sum_{\text{start}}^{p} \mu_i(E)s_i \tag{3.5}$$

the calculation also works for heterogeneous geometries.
For the calculation of λ, the photon has to be tracked from the *Start* position on the surface through several different regions i, each containing different materials, until point P where the interaction happens. The line segment s_i has to be determined in every region i by using the corresponding attenuation coefficient μ_i. This describes a tracing mechanism used to calculate λ, which is essential in MC simulations in radiation therapy. The cumulative distribution function

$$P(\lambda) = \int_0^\lambda \mathrm{d}\lambda' p(\lambda') = \int_0^\lambda \mathrm{d}\lambda' e^{-\lambda'} = 1 - e^{\lambda'}, \quad P(0) = 0, \quad P(\infty) = 1 \tag{3.6}$$

is calculated by integrating the probability weight distribution function $p(\lambda)$ provided by the attenuation law in equation (3.1). This a monotonically increasing function in the interval $[0, \infty]$. The distance to the first interaction site λ_1 can be sampled by using a transformation method and a uniform random number ξ_1 from the interval $[0, 1)$

$$\xi_1 = 1 - e^{-\lambda_1} \Rightarrow \lambda_1 = -\ln(1 - \xi_1). \tag{3.7}$$

The notation of the interval means that the number 1 is never included in the sampling of random numbers.
When the geometric setup of the simulation is taken into account, the photon first gets tracked a number of λ_1 mean free path lengths to the first interaction point. There the type of interaction has to be sampled. For photons energies in the case of radiation therapy four processes are common: photoelectric absorption (A), Raleigh scattering (R), Compton scattering (C), and pair production (P). The total linear attenuation coefficient is composed of the sum of the linear attenuation coefficients as material parameters at the interaction site

$$\mu(E) \equiv \mu_{\text{tot}}(E) = \mu_{\text{A}}(E) + \mu_{\text{R}}(E) + \mu_{\text{C}}(E) + \mu_{\text{P}}(E). \tag{3.8}$$

The interval $[0, 1]$ is divided into four parts

$$\begin{aligned} &[P_0, P_1] : \text{photoelectric aborption} \\ &[P_1, P_2] : \text{Raleigh scattering} \\ &[P_2, P_3] : \text{Compton scattering} \\ &[P_3, P_4] : \text{pair production} \end{aligned} \tag{3.9}$$

where

$$P_0 = 0, \quad P_1 = P_0 + \frac{\mu_{\text{A}}}{\mu_{\text{tot}}}, \quad P_2 = P_1 + \frac{\mu_{\text{R}}}{\mu_{\text{tot}}}, \quad P_3 = P_2 + \frac{\mu_{\text{C}}}{\mu_{\text{tot}}}, \quad P_4 = 1. \tag{3.10}$$

The sampling of the interaction type is achieved by sampling a second uniform random number ξ_2 in the interval $[0, 1]$ and then checking in which sub-interval this number is located.
When the interaction type is known, the parameters of the secondary particles, namely energy and scattering angles, can be determined. Another factor that has to be considered are conservation laws. This transformation method does not work for this aspect in general, this is why the rejection technique is preferred.
These steps can be repeated with all secondary particles, including electrons and positrons. The simulation of a particle stops if it leaves the geometry of interest or its energy is decreased below a cutoff energy E_{cut}. Statistical accuracy of the results is increased by repeating this process for a large number of primary particles.

3.1.2 Charged Particle Transport

The fundamental process of simulating the transport of any particle type though matter is described in section 3.1.1. Generally, this is the standard simulation method for neutral particle because the free path lengths of photons are in the order of the size of the simulated geometry. Therefore, only a small number of interaction has to be simulated. For electrons and protons this is not the case as they would undergo a large number of

single interaction when considering energy ranges used in radiation therapy. This results in this method being impractical for the majority of transport issues in radiation therapy since it would take a long time to simulate the whole history of a single charged particle. Most of the interactions of the charged particles are elastic or semi-elastic though, meaning no energy or only a small amount of energy is being transferred from the particle to the matter. The particle direction is also changed only by small scattering angles. This allows for the formation of one CH step which consists of many elastic and semi-elastic events. This CH technique is mostly used for the simulation of particle transport in radiation scenarios nowadays.

All interactions of a charged particle are divided into soft and hard collisions as well as soft and hard bremsstrahlung production events by this implementation. For the collision events, they are distinguished by an arbitrary kinetic energy loss E_c and the bremsstrahlung production is differentiated using the parameter k_c. When a collision transfers an energy below the threshold of E_c to secondary electrons it is classified as a soft collision. Simulation of these events is is done implicitly through continuous energy transfer from the charged particle to the matter surrounding the particle track. The change of trajectory due to many small angles is simulated by one large multiple scattering angle. Hard collisions are simulated the same way as for photons, outlined in section 3.1.1. Secondary particles created through hard collisions carry a minimum energy of E_c. This lower threshold for hard collisions also provides the maximum energy and range of charged secondary particles produced during soft collisions. The range is bound to be smaller than the spatial resolution of the geometry. As for the parameter k_c, it has a similar meaning. This results in the fact that these two parameters, E_c and k_c, have to be chosen with care. If the parameters are chosen too small, the simulation will take a long time to complete. In many cases, both parameters are chosen to be equal.

Due to the approximate nature of the CH method, it is necessary to limit the maximum distance travelled in one CH step. This is done by introducing another user parameter, the global step size s_{max}, or the material- and mass density-dependent parameters s^i_{max}. Many MC codes determine this maximum step size based on the percentage maximum energy loss E_{step}. Using this approach, the step size is automatically related to the stopping power and mass density of the current material.

The end of one CH step is determined either by the next hard interaction or by the maximum step size. This results in the history of for example an electron looking like illustrated in figure 3.1. During CH steps the electron is moving in straight lines in general, contradicting the real electron path. At the end of each step or between the step limits the direction is changed due to multiple scattering, shown in figure 3.2a. In the case of changing the direction between the step limits, the so-called random hinge method, illustrated in figure 3.2b, is applied. In figure 3.1 it can be seen that the first CH step is limited by a hard Møller interaction. This type of interaction results in so-called delta electrons or secondary electrons. These delta electrons are simulated using the CH method until their energy drops below E_{cut} or if they are transported outside the

region of interest. Figure 3.1 also shows the limitation of a CH step due to the maximum step length and bremsstrahlung production events. The photons due to bremsstrahlung production events are simulated using the analog method described in section 3.1.1. The different components used to describe the charged particle path during one CH step are roughly outlined in the following subsections.

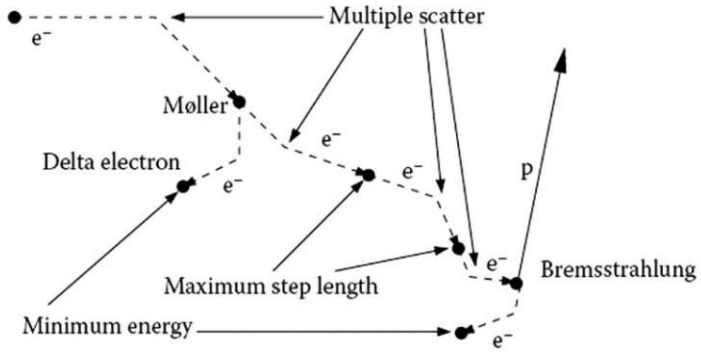

Figure 3.1: Sample particle history for an electron. Starting with a primary electron e^- (dashed line) undergoing multiple scattering, Møller interactions, and bremsstrahlung production events leading to secondary electrons (dashed lines) and secondary photons (solid lines) [71].

(a) Change of directory due to multiple scattering

(b) Change of directory due to random hinge

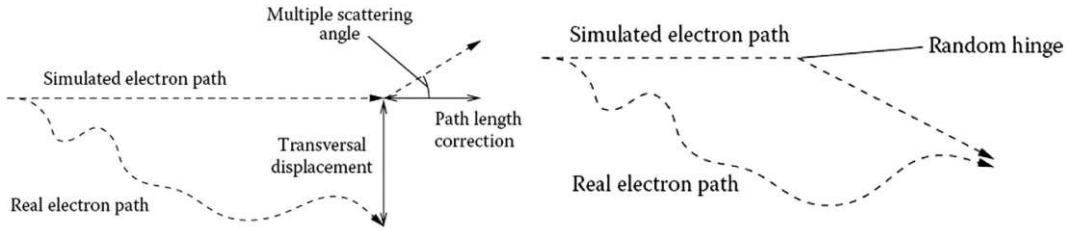

Figure 3.2: The simulated path of an electron in relation to the real path. Using the CH method with multiple scattering in figure (a) results in the necessity to correct the path length and a transverse displacement has to be taken into account. The random hinge method in figure (b) approximately takes the transverse displacement into account [71].

3.1.2.1 Continuous Energy Loss

Over the course of one CH step the charged particle continuously loses energy due to soft interactions. The restricted linear stopping power

$$L(\vec{r}, E, E_\mathrm{c}, k_\mathrm{c}) \equiv -\left(\frac{\mathrm{d}E}{\mathrm{d}s}\right)_\mathrm{res} = L_\mathrm{col}(\vec{r}, E, E_\mathrm{c}) + L_\mathrm{rad}(\vec{r}, E, k_\mathrm{c}) \tag{3.11}$$

describes the average energy loss $\mathrm{d}E$ per CH step length $\mathrm{d}s$ at point $\vec{r}$. The terms in the second part of equation (3.11) are called the restricted linear collision

$$L_\mathrm{col}(\vec{r}, E, E_\mathrm{c}) \equiv -\left(\frac{\mathrm{d}E}{\mathrm{d}s}\right)_\mathrm{res,col} = N(\vec{r}) \int_0^{E_\mathrm{c}} \mathrm{d}E' E' \sigma_\mathrm{col}(\vec{r}, E, E') \tag{3.12}$$

and the radiation stopping power

$$L_\mathrm{rad}(\vec{r}, E, k_\mathrm{c}) \equiv -\left(\frac{\mathrm{d}E}{\mathrm{d}s}\right)_\mathrm{res,rad} = N(\vec{r}) \int_0^{k_\mathrm{c}} \mathrm{d}k' k' \sigma_\mathrm{rad}(\vec{r}, E, k'). \tag{3.13}$$

$\sigma_\mathrm{col}(\vec{r}, E, E')$ and $\sigma_\mathrm{rad}(\vec{r}, k, k')$ are the collision and bremsstrahlung production cross sections. $N(\vec{r})$ denotes the number of scattering targets per unit volume at point $\vec{r}$. Upper limits of these integrations are E_c and k_c, restricting the energy transfer to secondary particles to these values.
The step length s during one CH step for an electon with initial energy E_0 and energy loss of ΔE is calculated by integrating equation (3.11), thus yielding

$$s = -\int_{E_0}^{E_1} \frac{\mathrm{d}E}{L(\vec{r}, E, E_c, k_c)} = \int_{E_1}^{E_0} \frac{\mathrm{d}E}{L(\vec{r}, E, E_c, k_c)}, \tag{3.14}$$

where $E_1 = E_0 - \Delta E$ is the energy left at the end of the step.

3.1.2.2 Multiple Scattering

During a CH step charged particles move in a straight line, thus contradicting reality, as illustrated in figure 3.2a. The probability of $p(\theta, \varphi)\,\mathrm{d}\theta\,\mathrm{d}\varphi$ that the electron is scattered within the multiple scattering angular section $([\theta, \theta + \mathrm{d}\theta], [\varphi, \varphi + \mathrm{d}\varphi]$ is modelled as a 2D Gaussian distribution

$$p(\theta, \varphi)\,\mathrm{d}\theta\,\mathrm{d}\varphi = \frac{\theta}{\pi \overline{\theta^2}(s)} \exp\left(-\frac{\theta^2}{\overline{\theta^2}(s)}\right) \mathrm{d}\theta\,\mathrm{d}\varphi, \tag{3.15}$$

where θ is the azimuthal multiple scattering angle, φ is the polar multiple scattering angle, and $\overline{\theta^2}$ is the mean square deflection angle after step length s. Two separate cumulative angular distributions are gained by equation (3.15)

$$P_\theta(\theta) = 1 - \exp\left(-\frac{\theta^2}{\overline{\theta^2}(s)}\right), \quad P_\varphi(\varphi) = \frac{\varphi}{2\pi}. \tag{3.16}$$

Using the transformation method outlined in section 3.1.1 and a uniform random number ξ_0 an angle θ is sampled as

$$\theta = \sqrt{-\overline{\theta^2}(s)\ln(1-\xi_0)}. \tag{3.17}$$

ξ_0 is sampled from the interval $[0, \xi_\theta^{\max}]$ where $\xi_\theta^{\max} < 1$. The polar angle φ is determined from a uniform distribution in $[0, 2\pi]$.
$\overline{\theta^2}(s)$ is calculated using the linear scattering power $T_s(\vec{r}, E)$, a material parameter depending on the atomic composition of the material in point $\vec{r}$ and the electron energy E, yielding

$$\overline{\theta^2}(s) = \int_0^s \mathrm{d}s' T_s(s', E). \tag{3.18}$$

Using well established MC code environments like FLUKA (FLUktuierende KAskade), Geant4 (GEomentry ANd Tracking 4), PHITS (Particle and Heavy Ion Transport Code System), and MCNP (Monte Carlo N-Particle Transport Code) ensures that the implementation of these calculation are done with great precision and reliability.
Before running a MC simulation in the case of a particle physics problem, using one of the above mentioned MC environments, the problem usually has to be defined according to the following steps [69]:

1. Geometry and material definition
2. Source term (particle type, source position, direction of travel, energy, number of particles)

When this is defined, the MC code will handle the following steps:

1. Random sampling of the outcome of events according to probability distributions
2. Secondaries of the same primary particle are transported before starting the next
3. Computation of the response: Random walk results are used to calculate the quantities of interest and the according statistical uncertainty

Since the RP department of MedAustron is specialized in using FLUKA for their simulation purposes, the simulations for this thesis are done using this particular MC tool.

3.2 FLUKA

FLUKA (FLUktuierende KAskade) is a multipurpose MC code environment used for simulating the interactions and transport of particles. It is developed at the European Organisation for Nuclear Research (CERN) and the Italian Institute for Nuclear Physics (INFN) and used for a wide range of applications, including accelerator design and shielding, radiation protection, particle physics, dosimetry, detector simulation, and hadrontherapy. FLUKA aims to provide the best physics model with regards to completeness and precision. As far as possible, FLUKA is based on well-tested microscopic models. It uses this 'microscopic' approach to provide a sound physical basis for every step. Performance optimization is achieved by comparing particle production data at single interaction level [72–74]. This preserves correlation within the interactions and among all shower components, and it even provides predictions when no experimental data are available [73]. The basic building block of FLUKA is the description of the hadron-nucleon (h-N) interaction for a broad energy range. This is essential in achieving a solid description of the hadron-nucleus and nucleus-nucleus interaction [74]. The schematic description of high energy hadron-nucleus (h-A) interactions can be achieved by the sequence of following steps [74]:

1. Glauber-Gribov cascade
2. (Generalized) IntraNuclear Cascade ((G)INC)
3. Preequilibrium emission
4. Evaporation, Fragmentation, Fission and final deexcitation

Glauber-Gribov Cascade

Using the Glauber formalism, elastic, quasi-elastic, and absorption h-A cross sections can be derived from free h-N cross sections and the nuclear ground state. Full description of this model is out of the scope of this thesis, further information is found in [74–80].

(Genralized) IntraNuclear Cascade

At high enough energies, h-A interactions can be described as a cascade of two-body interactions with regards to the projectile and the reaction products. A detailed description of this topic is out of scope of this thesis, refer to [74, 81, 82] for more information.

Preequilibrium

At lower energies than the π production threshold, a variety of preequilibrium models are developed [83] following two approaches:

- Quantum-mechanical multi-step model
- Exciton model

The quantum-mechanical multi-step model is very complex but provides a good theoretical background, while the exciton model relies on statistical assumptions, is simple and fast. To get more in-depth information on this topic, refer to [74, 82, 84–87].

Evaporation, Fission and Nuclear Break-up

In the last step of the FLUKA reaction chain, the nucleus is a thermally equilibrated system, which is characterized by its excitation energy. This excitation energy can be dissipated by 'evaporating' nucleons, fragments, γ rays, or even fission. More details for this step are presented in [74, 81, 82, 88, 89].

3.2.1 Scoring

Scoring in FLUKA describes the process of evaluating quantities at certain positions of the simulated setup. By using the built-in, pre-defined estimators provided by FLUKA, most of the commonly needed quantities can be scored. An estimator would be the MC equivalent of the result or measurement of a real experiment. As with real measurements, an estimator has a statistical error because it is obtained from a statistical distribution. FLUKA is able to score particle fluence, current, track length, energy spectra, Z spectra, energy deposition, dose, displacement damage, and more. In the course of this thesis, only the estimators for particle fluence, energy deposition, displacement damage, and dose are used.
A few of FLUKAs estimators and their according 'Scoring cards', expressed in capital letters, are:

- Energy deposition:
  → USRBIN
  → EVENTBIN
- Fluence:
  in relation to the position:
  → USRBIN
  in relation to the energy:
  → USRTRACK
  → USRCOLL
  → USRBDX

in relation to energy/other:

→ USRYIELD

- Activation:

  in relation to isotopes:

  → RESNUCLEI

  in relation to space:

  → USRBIN

Only USRBIN scoring cards are needed for the quantities used in the course of this thesis. This card allows for scoring by region, based on cylindrical coordinates and Cartesian coordinates. The latter requires the coordinates and dimensions in x, y, z and the number of steps ($N_\mathrm{x}, N_\mathrm{y}, N_\mathrm{z}$, refer to figure 3.6) this volume should be divided into, creating a voxel structure where the quantities of interest are scored and analyzed for each voxel. The particle fluence estimator is used to score the HEHeq and THN fluences in the sensitive volumes (SVs) of the components. Energy deposition estimators are used for the calculation of the deposited charge in a sensitive volume. Displacement damage (DD) estimators are used to get an idea of how much the atoms in the components are displaced from their initial positions on average. The dose estimators are needed to quantify the total ionizing dose (TID) accumulated by the components.

Particle fluence: Is expressed as particles per cm^2 but represents the density of particle tracks per primary particle. It is written as the length of particle tracks inside of a bin divided by the volume of the bin $[\frac{\mathrm{cm}}{\mathrm{cm}^3}]$. It is scored as particles per cm^2 per primary particle (pp) $[\frac{1}{\mathrm{cm}^2\,\mathrm{pp}}]$.

Dose: Scored as energy per unit mass per primary particle $[\frac{\mathrm{GeV}}{\mathrm{g\,pp}}]$

Displacement damage: Scores the displacement per atom (DPA) per primary particle.

Energy deposition: Scored as energy deposition density per primary particle $[\frac{\mathrm{GeV}}{\mathrm{cm}^3\,\mathrm{pp}}]$.

3.2.2 Geometry

Before implementing the simulation geometry, the first step was to identify the sensitive components. This was done in coordination with a Medical Device Safety (MDS) system architect of MedAustron. According to his expertise on the topic of Single Event Upsets, the sensitive components have been identified, as seen in the 'First Step' part of figure 3.3.

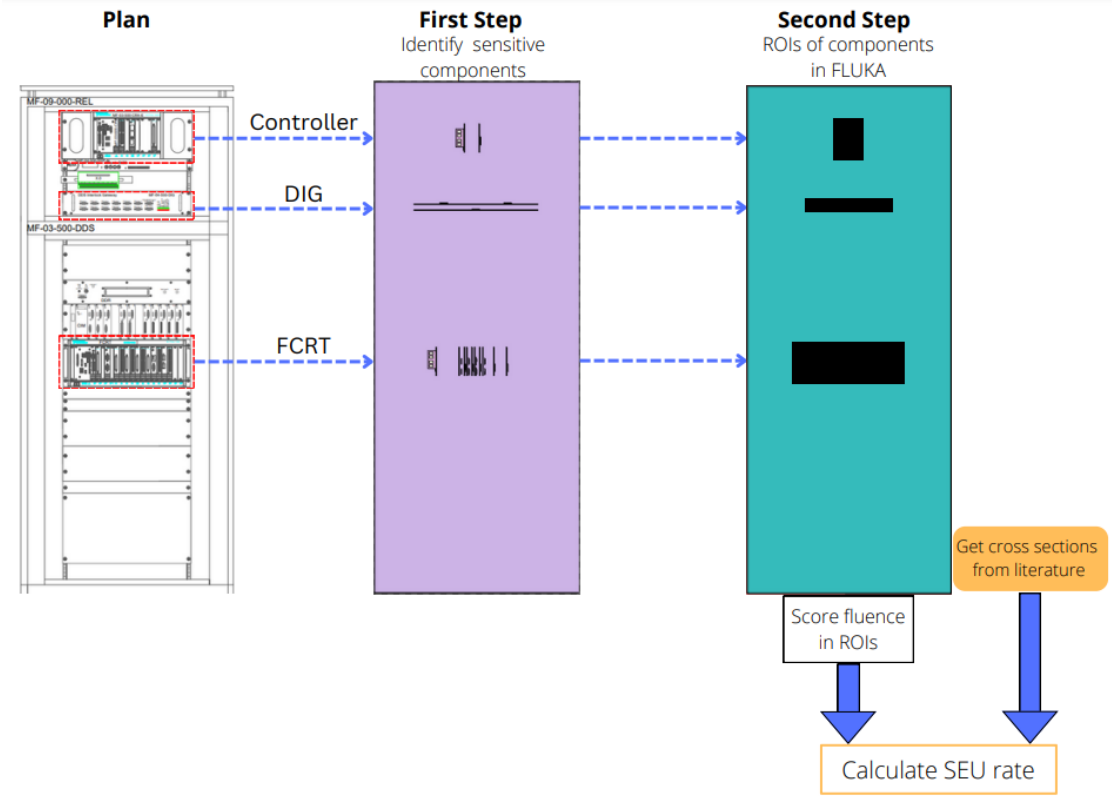

Figure 3.3: An illustration how the geometry of the rack and the components is implemented based on the region of interests (ROIs) identified.

The important modules regarding SEUs in the Controller according to the MDS system architect, are marked in red in figure 3.4. They are standard National Instruments (NI) modules, specifically the control unit NI PXI-8135, which contains an Intel i5-2510E processor and some RAM sticks, and the re-configurable digital I/O module NI PXI-7813R, which contains a Virtex-II 3M Gates FPGA.

The DDS Interlock Gateway (DIG) is a special configuration, and the important modules regarding SEUs are not standard modules as in the Controller. Here the important components are three ProASIC3 A3P1000 FPGAs.

In the Fast Controller - Real Time (FCRT) the important modules regarding SEUs, according are marked in red in figure 3.5. They are also standard NI modules, the controller unit NI PXI-8135, also containing an Intel i5-2510E processor and some RAM sticks, the re-configurable digital I/O modules NI PXI-7813 and PXI-7811R, containing a Virtex-II 3M Gates FPGA and a Virtex-II 1M Gates FPGA respectively, and the digital I/O modules NI PXI-6534, which contains two 32 MB RAMs and two different,

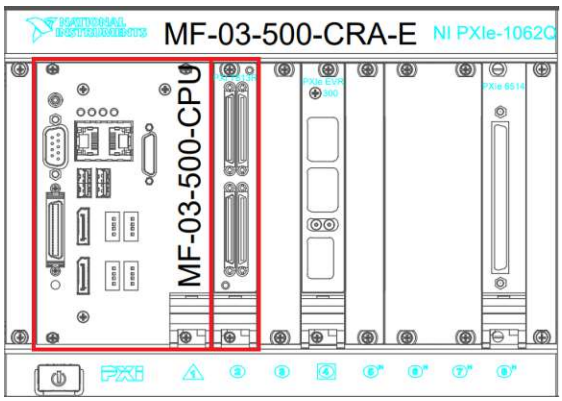

Figure 3.4: The NI PXIe-1062C module used for the Controller. The relevant modules, the control unit PXI-8135 and a PXI-7813R, are marked in red.

not further specified, FPGAs.

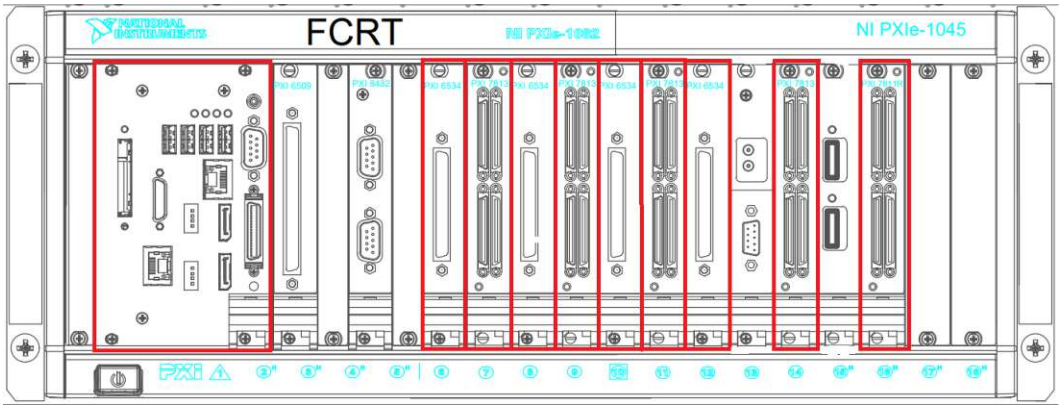

Figure 3.5: The combination of an NI PXIe-1082 module and an NI PXIe-1045 is used for the FCRT. The relevant modules, the control unit PXI-8135, four PXI-7813, four PXI-6534 and one PXI-7811R, are marked in red.

Such small components are difficult to model, and since the detailed positions of them were not known, the choice was to implement sensitive regions out of silicon surrounding the volume where the components are located. This is indicated in the 'Second Step' of figure 3.3. Using such volumes imposes an inherent error when analyzing for example the fluence to such regions. This is well known and why these results are used in combination with a benchmark simulation to get an estimation how much the fluence is increased.
The simulation geometry, consisting of the steel plate forming the floor of the IR above the rack, the electronics rack itself, and the volumes representing the sensitive compo-

nents, is implemented using the flair (FLuka Advanced InteRface) tool, an advanced user-friendly interface developed for editing FLUKA input files, executing the code, and visualizing the output files [90]. Basic schematics of the implemented simulation geometry can be seen in figure 3.7. As a particle source, a proton beam with a varying angle and energy is used. The geometry of the sensitive areas was implemented as blocks of silicon as a more detailed geometry would need a vast amount of primary particles simulated to get reliable statistics. These blocks of silicon are then used in the scoring process with the above-mentioned Cartesian scoring in a USRBIN. The ROIs are divided into small bins with the step sizes N_x, N_y, N_z, shown in figure 3.6, chosen in such a way, that the resulting bins can be summed up to represent the volume of the components in the area. By having a larger sensitive volume and breaking it down into smaller ones, the fluence in the area can be simulated and scored with a higher degree of precision.

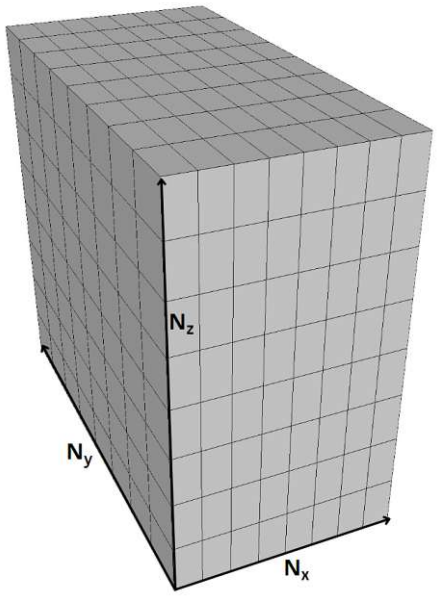

Figure 3.6: The binning of the ROIs illustrated using an arbitrary geometry and step size. The silicon volume is divided into several sub-volumes, which are added up to represent the volumes of the components in the ROIs. The division is done by specifying the number of steps in each direction N_x, N_y and N_z.

The ROI size for the Controller is $30 \times 20 \times 12\text{cm}^3$ with step sizes $N_x = 100$, $N_y = 12$ and $N_z = 10$. The resulting sub-volumes are $0.6\,\text{cm}^3$. The ROI size of the DDS Interlock

Gateway (DIG) is $50 \times 30 \times 4\text{cm}^3$ with $16 \times 10 \times 10$ steps. This puts the sub-volume of the DIG bins at $3.75\,\text{cm}^3$. For the Fast Controller - Real Time (FCRT) the size is $60 \times 20 \times 12\text{cm}^3$ and the steps are $200 \times 12 \times 10$ resulting in a sub-volume of $0.6\,\text{cm}^3$. The different sub-volume sizes are due to different important components in the ROIs. For example, in the DIG only FPGAs with a fairly large volume are of interest, whereas in the Controller and FCRT RAM sticks with far smaller silicon volumes are installed.

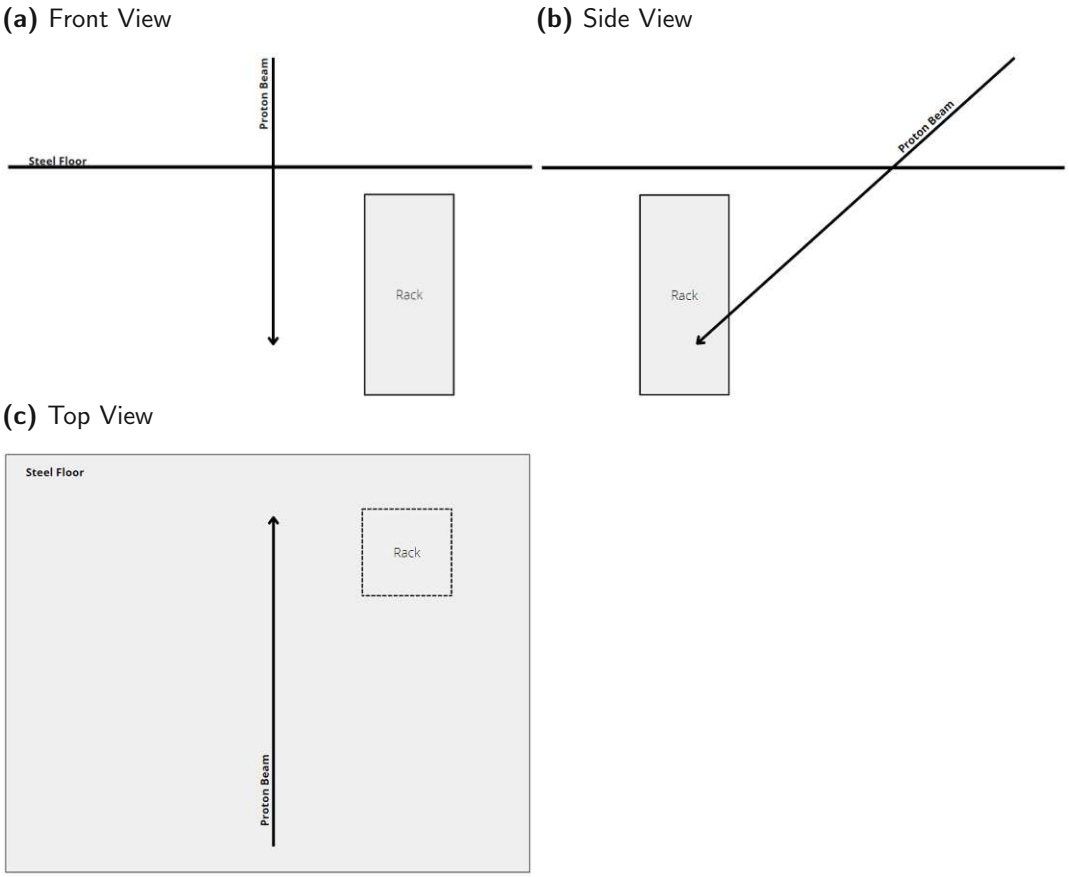

Figure 3.7: Schematic of the basic simulation setup for an arbitrary beam angle with (a)top view, (b)side view and (c)front view to get an understanding of the location of the rack in relation to the beam source and steel floor.

3.2.3 Simulation Uncertainties

Many input parameters for a realistic MC simulation have some kind of uncertainty. This not only applies to the geometrical specifications of the problem, the composition of the

material, and the cross-sections, but also to 'external' parameters, like temperature, pressure, external electromagnetic fields, etc., which are also needed for a realistic description of the problem [91]. Predicting the uncertainty of experimental observables produced by MC particle transport is known as uncertainty quantification. The uncertainties of an observable are derived as a final product from uncertainties in the above-mentioned parameters [92]. This mixture of uncertainties is illustrated in figure 3.8.

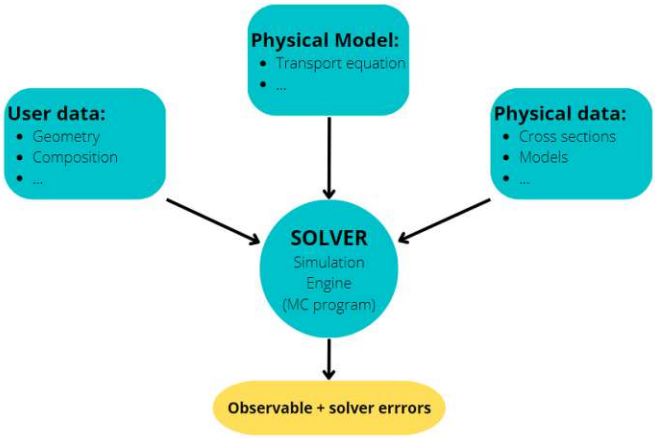

Figure 3.8: An overview of the different inputs, all containing uncertainties, for an MC simulation. [92]

Using an existing MC software to execute simulations, the input data from the MC user's perspective mostly focuses on the ones they are directly in control of, like the geometry, the material composition, etc. The ones often neglected are the ones provided by the software, which normally originate from other experiments [91]. According to [92] the quantification of the uncertainties in MC simulations can be summed up as follows:

- Uncertainties in the physical model (transport equation) can be neglected since the transport equation reflects the 'real world'. There are no other approximations in the model other than those resulting from MC sampling.
- The verification of the physical parameters used in the simulation, such as cross sections, employed models, etc., is of high importance in order to obtain reliable results[1].
- An accurate study of the experimental configuration by the MC user is necessary. A properly restricted set of parameters has to be selected since it is impossible to perform an uncertainty quantification over several hundred different parameters.

[1] Using well-established MC programs like FLUKA simplifies this process since experts are concerned with maintaining the physical parameters and ensuring as accurate results as possible.

This also means that the geometry of the simulation has to be implemented with the right amount of detail for reliable results.

The final result for the observable is obtained through statistical analysis of N MC simulation runs, as indicated in figure 3.9. A high number of runs reduces the significance of each simulation run's individual error, resulting in reduced uncertainty.

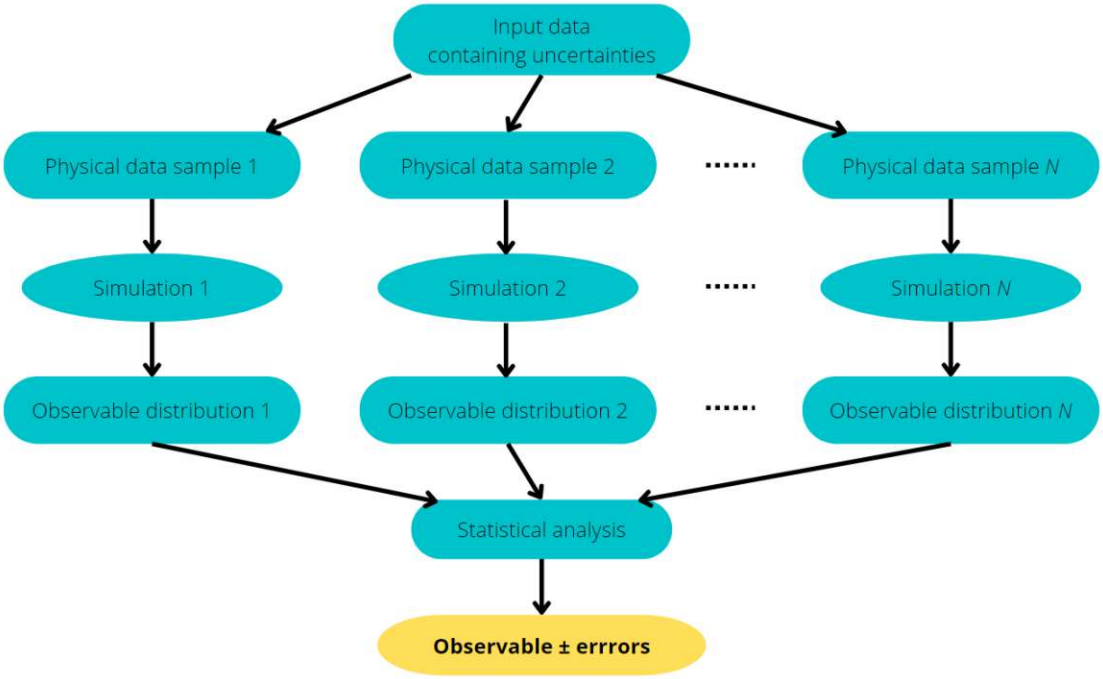

Figure 3.9: The observable, including errors, is obtained through the analysis of N independent MC simulation runs. This allows to reduce the impact of individual uncertainties of each run.

In general, it is possible to quantify the quality of a result based on the statistical error. Table 3.1 is based on an old version of the MCNP manual and is still considered reliable [93].

Relative Error	Quality of Result
50 % to 100 %	Garbage
20 % to 50 %	Factor of a few
10 % to 20 %%	Questionable
$< 10\,\%$	Generally reliable

Table 3.1: Quantification of the quality of a result obtained through MC simulations based on the statistical error from an old MCNP manual [93].

3.3 Data Processing

In this section, the calculation process for the SEU rate in the case of this thesis is explained.

3.3.1 Single Event Upset Rate Calculation

The calculation of the SEU rates in the components is achieved by taking example cross-sections of a radiation monitor according to [26]. These values are found in table 3.2.

Particle Type	Cross Section σ $[\frac{\text{cm}^2}{\text{bit}}]$
HEHeq	$3.1 \cdot 10^{-15}$
THN	$3.0 \cdot 10^{-14}$

Table 3.2: HEHeq and THN cross sections for a radiation monitor used at CERN from [26].

Taking the fluence data from the FLUKA simulation for each ROI, a mean value for the fluence in one bin is calculated by averaging the fluence in all bins according to

$$\Phi_{\text{avg}} = \frac{\sum_i \Phi_i}{N_{\text{bins}}}. \tag{3.1}$$

This average fluence is then used as a normalized fluence per sub-volume/bin. Using this value, a total fluence for the actual sensitive volume in the component is calculated by multiplying the average fluence by the number of active sub-volumes in the ROI. This means multiplying it by the number of bins the volume of the RAMs, FPGAs and processors correspond to.

The total SEU rate is then calculated by multiplying the obtained total fluence to the active components by the SEU cross sections from table 3.2 using equation (2.10)

$$N_{\mathrm{SEU}} = \Phi_{\mathrm{HEHeq}} \cdot \sigma_{\mathrm{HEHeq}} + \Phi_{\mathrm{THN}} \cdot \sigma_{\mathrm{THN}}. \tag{3.2}$$

This value corresponds to a SEU rate per bit since per-bit cross sections were used for calculation. To obtain the total amount of SEUs per component, this per-bit-rate is multiplied with the number of bits in each component, according to their datasheets, thus yielding

$$N_{\mathrm{total}} = N_{\mathrm{SEU}} \cdot N_{\mathrm{bits}}. \tag{3.3}$$

4 Results

The simulations feature silicon sensitive volumes (SVs) for the three region of interests (ROIs), the Controller, the DIG and the FCRT as seen in figure 4.1. The sizes of these SVs are chosen to represent the physical sizes of the relevant regions regarding SEU sensitivity. They are constructed as a large USRBIN for fluence scoring, divided into sub-volumes as previously indicated in figure 3.6, that are easily scalable to the real volumes of the studied FPGAs, RAMs and processors.
The total fluence in the ROIs is averaged to the sub-volumes. This resembles a conservative approach as the fluence will vary the farther away from the beam center the components or bins are located, but was deemed as accurate enough for the estimation. Also, with this approach there is more sensitive volume compared to the real components which leads to a known overestimation of the rates. This averaged fluence is then used to calculate the SEU rates according to the equations from section 2.2.3. All presented fluences and SEU rates in this section are normalized to $3 \cdot 10^{10}$ primary protons, which represents the typical particle rates used in a treatment fraction. Of course, in a treatment the total particle count is composed of particles at several different energies, so simulating all particles at a single energy results in a conservative approach as well. Also, the statistical uncertainty of the fluences shown in this section is below 10 % (indicated by the error bars) which means that the results can be considered reliable according to the definitions presented in table 3.1 in section 3.2.3.

Before getting into the results, it is necessary to understand the directions that are used to describe them. Figure 4.2 is an illustration that shows the Cartesian coordinates in relation to the beam direction, including the beam angles used in the simulations. In this setup the beam angle is defined relative to the z-axis and the 0° position relates to particles travelling in the $-z$-direction. It has to be noted that the beam only travels in the $y-z$-plane so an x-component to the particle fluence is only due to scattering of the beam.

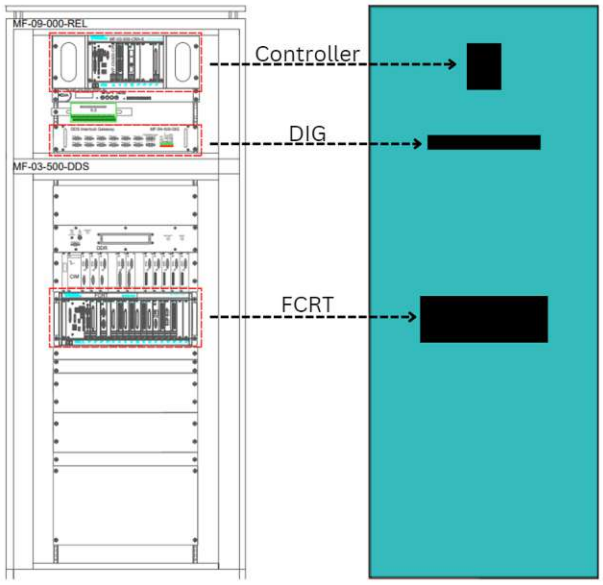

Figure 4.1: An illustration of the SVs representing the according ROIs. The sizes of the SVs on the right have been chosen to represent the physical sizes of the relevant regions regarding SEU sensitivity of the Controller, the DIG and the FCRT in the rack.

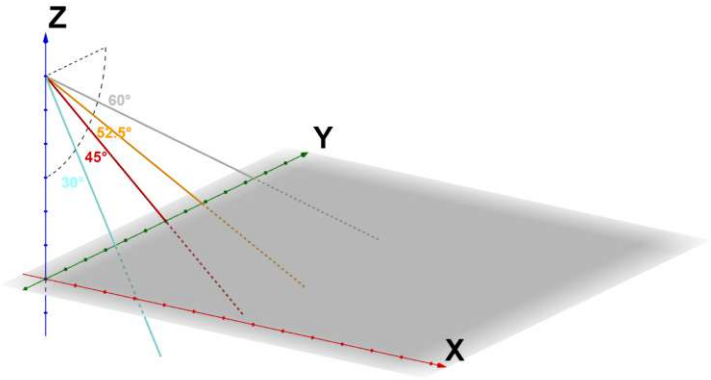

Figure 4.2: An illustration showing the alignment of the axes and the direction of the beam at the different angles in a Cartesian coordinate system. It is to note that the beam only travels in the $y - z$-plane.

The necessity to study SEU rates in the DDS rack arose from the suspicion that a significant amount of secondary particles reaches its position for a 60° beam. As it turns out, the suspicion was correct, and the location of the rack is sub-optimal for the new beam angle, as illustrated in figure 4.3. Especially figure 4.3c highlights that a significant amount of particles is stopped in the rack. This is indicated by the lighter color, showing the missing particles behind as a sort of 'shadow', when compared to the general color gradient in the picture.

(a) Front View **(b)** Side View

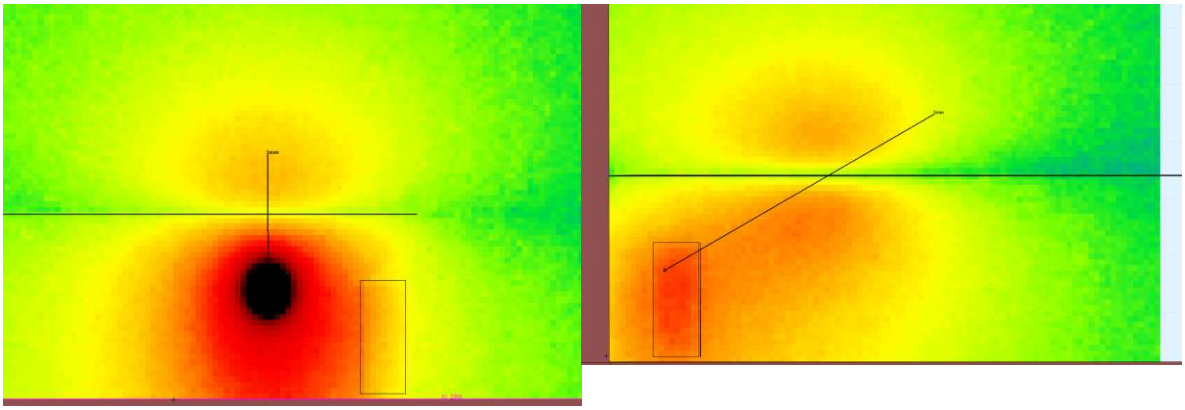

(c) Top View **(d)** 3D View

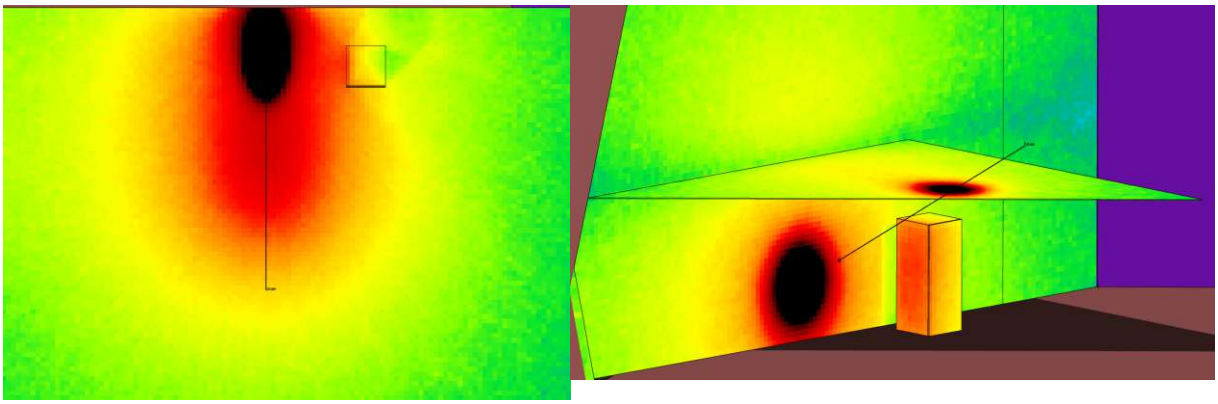

Figure 4.3: Plot of the HEHeq fluence in the IR4 for a 250 MeV proton beam at a 60° beam angle superimposed on the actual simulation geometry. It can be seen that a significant amount of particles is lost in the DDS rack.

Two fundamentally different simulation setups have been used in this thesis, namely simulations with and without a target in the beam line, as illustrated in figure 4.4. A target in the beam line, whether it is a water target, a concrete dump, or a patient, is equal to a normal scenario. No target in the beam line resembles an accident scenario

where someone forgot to include a target, for example, during quality assurance.
A first important step in analysing the results is, to check for the influence of this target on the fluence scored in the ROIs. Figure 4.4 shows the setup for the simulation in the case of a target, indicated as dark blue block in figure 4.4a and without a target in figure 4.4b. The target is a water cylinder with a radius of 15 cm and a height of 40 cm which is used as a water phantom, to simulate a patient lying on the treatment table.
Positioning of the target is chosen in such a way that the beam always intercepts the cylinder in its center, no matter which angle the beam is aimed at. This leads to paths of different length for the beam particles in water and in turn a different amount of particles deposited along the way, illustrated in figure 4.5. The length is shortest at 90° and longest at 37°, which is when the beam travels diagonally through the target.

(a) Setup with a target **(b)** Setup without a target

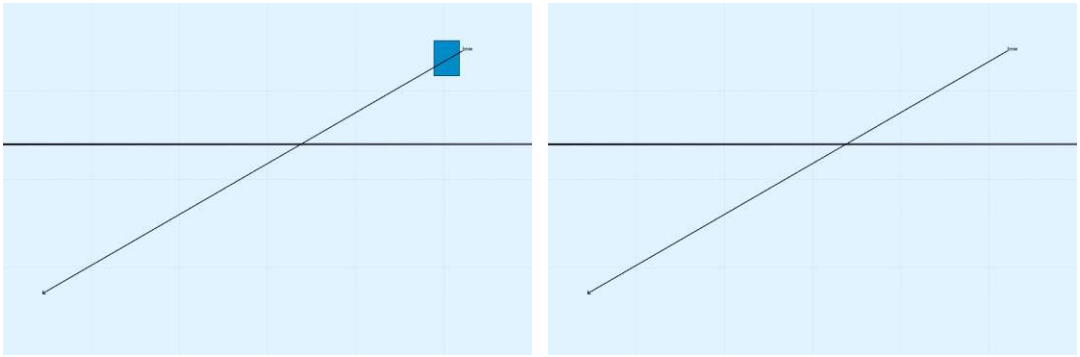

Figure 4.4: Comparison of the setup (a) with and (b) without a target. The target is positioned in such a way that the beam intercepts the center of the water cylinder.

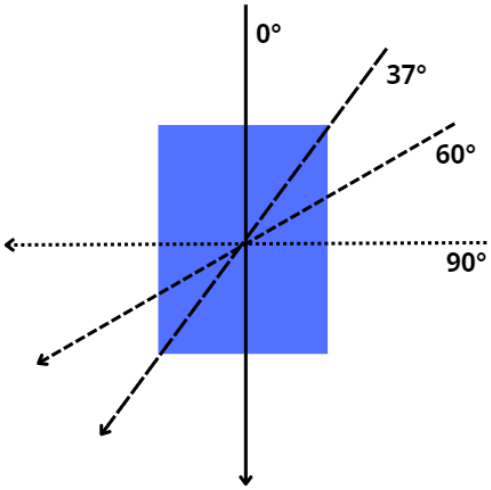

Figure 4.5: Illustration of the different path lengths of a proton beam in the target for beam angles of 0°, 37°, 60° and 90°. It can be seen that the length varies greatly, being the shortest for 90° and the longest for when the beam travels diagonally through the target, corresponding to around 37° for the dimensions of the target in use.

Figure 4.6 shows the comparison between the HEHeq fluence in the FCRT of a 250 MeV proton beam at a 60° angle with and without a water target in the beam line. It can be seen that the fluence for the 'no target' case is far higher (almost a factor of 2 at the highest value) than for the simulation with a target for 250 MeV protons at 60°. The 1D fluence plots are generated using flair and it was chosen that the values are averaged over the axes not shown, so for the fluence in the x-direction it is averaged over the bins in the y and z-direction.

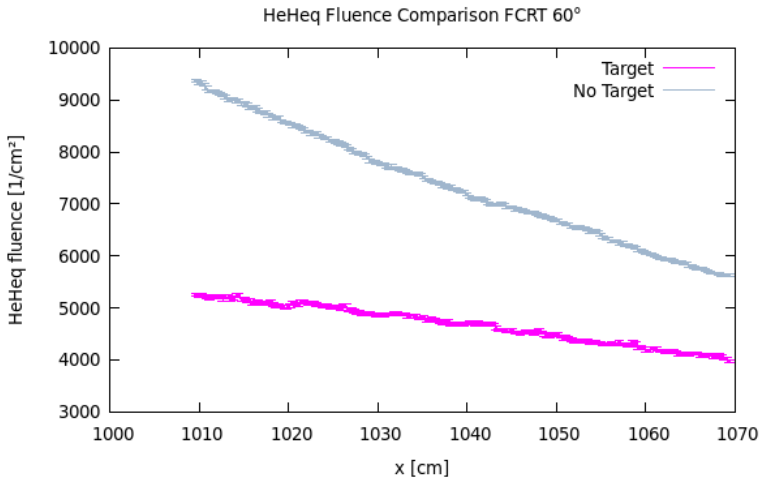

Figure 4.6: Comparison of the HEHeq fluence in the x-direction of the FCRT at 250 MeV and 60° beam angle with and without a target. FLUKA averages the results over the directions not shown in the plot, so for the x-direction the values are averaged over the bins in the y and z-direction of the ROI.

Now that the impact of a target on the fluence is defined, the results for each region of interest can be studied. Since the goal is to find a 'worst case' scenario in regards to SEUs, simulations without a target are studied in relation to a benchmark simulation for 250 MeV protons at 0° beam angle with a target. This benchmark setup is chosen as a comparison because, in practice, no SEUs have been observed during operation with this radiation setup [10].

4.1 Single Event Upset Rate versus Beam Angles

Simulations at various angles are performed to gain an understanding of the importance of the beam angle in terms of SEU rates. The goal is to find a 'critical angle' at which the fluence of the HEHeq and THN, and subsequently, the SEU rate, is the highest. For this purpose, only the highest energy, 250 MeV, and no target were used. The studied angles include the in figure 4.2 depicted angles of 30°, 45°, 52.5°, and the new angle 60°.

To present an overview of the obtained fluences in the ROIs, a summation of the angular dependence of the fluence is shown in figure 4.7. It presents the HEHeq and THN fluences without a target in the x-direction (normal to the particle beam) in the Controller (figure 4.7a + 4.7b), the DIG (figure 4.7c + 4.7d), and the FCRT (figure 4.7e + 4.7f) for the above mentioned angles. It can be seen that the HEHeq fluence is highest for a

beam angle of 60° in all the ROIs. The decrese of the fluence when getting farther away from the beam is as expected and in a range of approximately 15 % for the HEHeq and THN fluence in the Controller. In the DIG, where the z-direction is the smallest and the y-direction is the biggest of all ROIs due to the shape of the rack slot, the fluence drop off is quite noticeable with approximately 30 %. It has to be noted that the overall fluence in the DIG is the lowest of all ROIs. An angle of 60° and 52.5° is fairly similar for the HEHeq fluences in the FCRT. This is due to the fact that the FCRT is the lowest ROI of the three. The drop off is approximately 20 % for the HEHeq fluence and approximately 30 % to 35 % for the THN fluence.

(a) HeHeq fluence in Controller

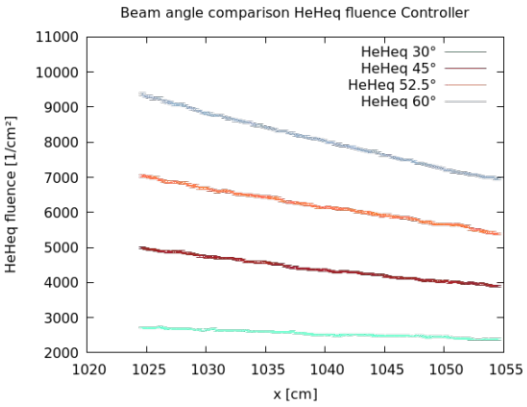

(b) THN fluence in Controller

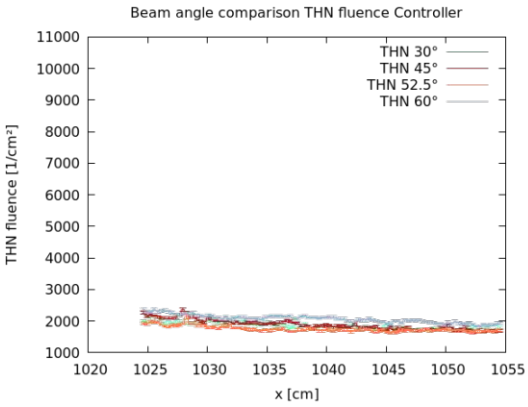

(c) HeHeq fluence in DIG

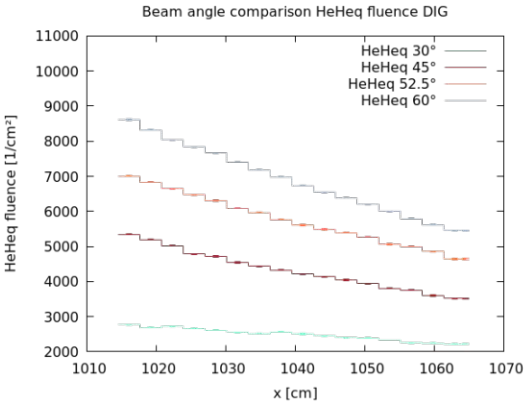

(d) THN fluence in DIG

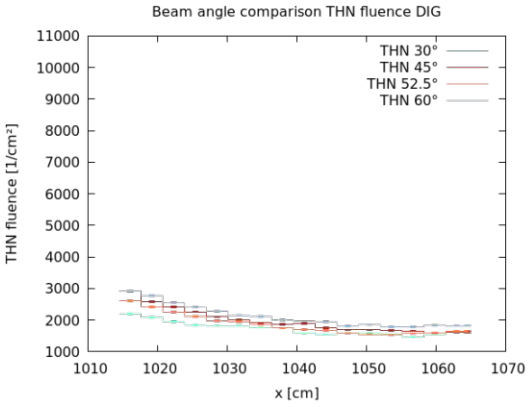

(e) HeHeq fluence in FCRT

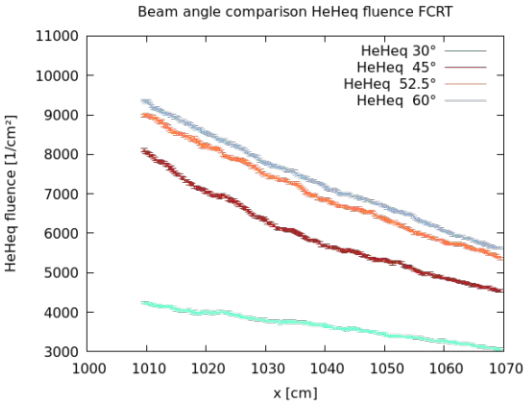

(f) THN fluence in FCRT

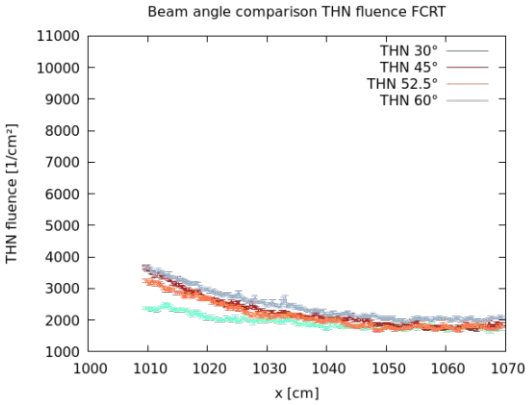

Figure 4.7: Comparison of the HEHeq and THN fluence in the x-direction (a)+(b) in the Controller, (c)+(d) in the DIG and (e)+(f) in the FCRT for different beam angles. Shown is the projection of the fluence on the x-axis of the ROIs which is the average of the fluence in the other two directions.

Controller

Figure 4.8 shows the comparison of the HEHeq fluence in the sensitive volume of the Controller for the case of no target in the beam line for the different beam angles. According to this data, the fluence is highest for a beam angle of 60°.
The 2D plots in figure 4.9 show the fluence in each subvolume. The values of each bin are obtained by averaging the values of all subvolumes in the direction not shown in the plot. In the x-y-plot, for example, the values are averaged over the z-direction. These plots are not used as an indicator of the fluences at the exact locations of the RAM, FPGA and processor, but more as an indicator of the fluence drop-off through the ROI. Figure 4.9a shows a much more gradual drop-off than figure 4.9b, as demonstrated by this comparison.

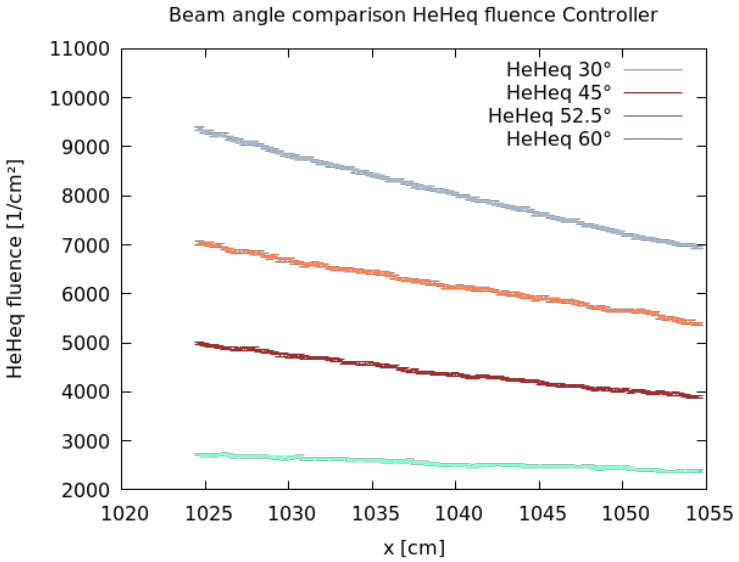

Figure 4.8: Comparison of the HEHeq fluence for beam angles of 30°, 45°, 52.5° and 60° in the x-direction in the sensitive volume of the Controller without a target.

(a) HeHeq fluence

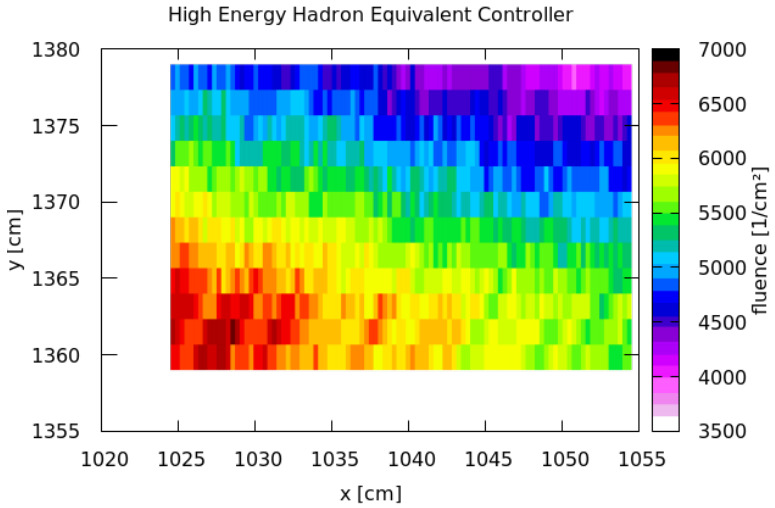

(b) THN fluence

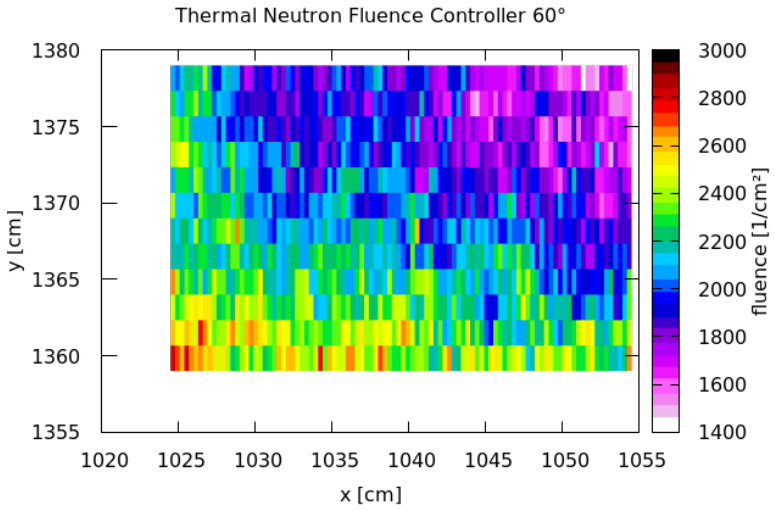

Figure 4.9: 2D plots of the (a) HEHeq and (b) THN fluence for beam angles of $60°$ without a water target in the $x-y$-direction in the sensitive volume of the Controller. The individual subvolumes can be seen. The values in the individual cells are obtained by averaging over the third direction, which is not included in the plot. These plots are only used to show the gradient of the SEU rate inside the ROI. Looking at the exact bin where the components are located is not possible, since the position of the rack and the positions of the components in the rack is connected to a lot of measurement uncertainties.

Based on the simulated fluences, the average per-bit SEU rates for a simulation of 250 MeV protons at 60° with and without a target and 0° with a target in the Controller are presented in table 4.1.

			Controller
SEU/bit at	60°	without target	$2.490(103) \cdot 10^{-10}$
		with target	$1.653(114) \cdot 10^{-10}$
	0°	with target	$2.984(523) \cdot 10^{-11}$

Table 4.1: Calculated SEU per bit rates in the Controller for simulations at 60° without a target and at 60° and 0° with a target in the beam line.

Based on these per-bit values, the total SEU rates for each component are calculated. In comparison to the simulations at 60° (rows 1+2 in table 4.2), the row 'SEUs at 0° with a target' shows the SEU rates for a the simulation used as a benchmark. These rates are multiplied by the number of bits for each component of interest, acquired from their respective datasheets, found in the first row of table 4.2 to obtain the total SEU rates for the different setups in table 4.2.

			Controller		
			FPGA PXI-7813	**i5**	**RAM**
		Nr. of bits	1728 kbit	209 kbit	68 Gbit
SEUs at	60°	without target	$8.6 \cdot 10^{-4}$	$5.2 \cdot 10^{-5}$	136.9
		with target	$5.71 \cdot 10^{-4}$	$3.45 \cdot 10^{-5}$	90.87
	0°	with target	$8.12 \cdot 10^{-5}$	$4.91 \cdot 10^{-6}$	12.9

Table 4.2: The amount of bits in the different components according to their datasheets in the Controller and the calculated SEU rates. The first two rows are for a 60° beam angle and the last row features rates for a 0° angle with a target and is used as a benchmark. All results are at a primary energy of 250 MeV and 3×10^{10} primary particles.

Even if the SEU rates in table 4.2 are an overestimation, due to the conservative approaches taken, the SEU rate at 60° and no target is by a factor of around 10 higher than for the benchmark case of 0° and no target.

Comparing the two simulations with a target, the risk is still about 7 times as high for the 60° simulation as for the benchmark case.
The RAM has by far the highest number of bits, which also leads to the high SEU rates calculated. According the the MDS division, high SEU rates in RAMs are not as fatal as high rates in other components, because they are normally not utilized at 100 % capacity, which would make the 'effective number of bits' lower. Also, state-of-the-art RAM generally is equipped with safety features like Error Correction Code (ECC), which is able to detect and correct bit errors in real time. Still, the considerably increased risks of SEUs in the processor and FPGA have to be considered, when planning the use of the gantry at the new angle.

DDS Interlock Gateway

As with the Controller, figure 4.10 shows the comparison of the fluence at different angles for the DIG without a target. The fluence for the 60° beam in the plot of figure 4.10 is used to calculate the values in table 4.4 for the row 'SEUs at 60° without a target'. In comparison to these rates, the results for the simulation with a target can be seen in the row 'SEUs at 60° with a target' of table 4.4. For reference, the values for the benchmark simulation are added in the row 'SEUs at 0° with target'.

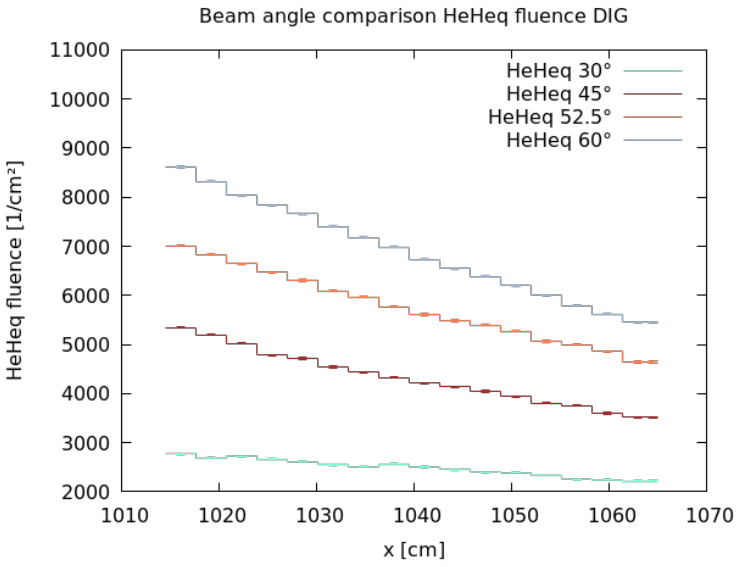

Figure 4.10: Comparison of the HEHeq fluence for beam angles of 30°, 45°, 52.5° and 60° in the x-direction in the sensitive volume of the DIG without a target.

(a) HeHeq fluence

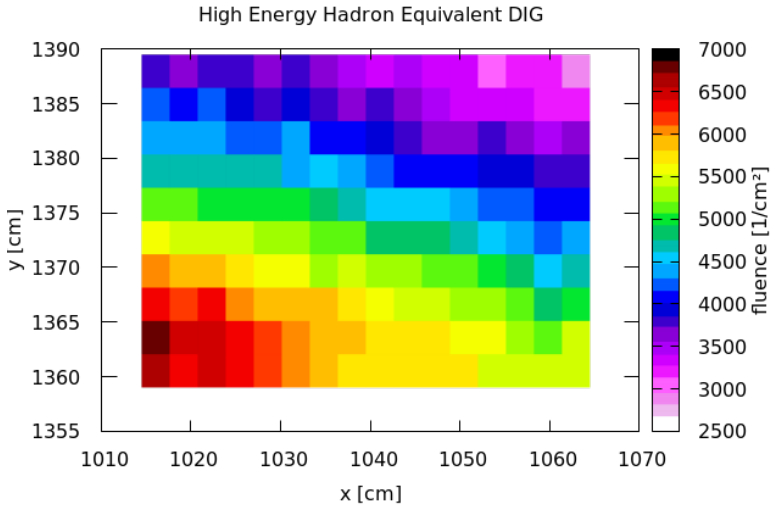

(b) THN fluence

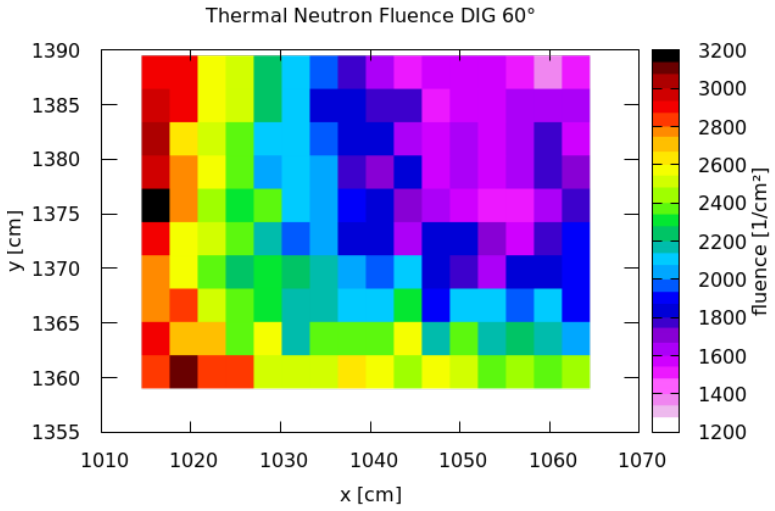

Figure 4.11: 2D plots of the (a) HEHeq and (b) THN fluence for beam angles of 60° without a water target in the x-y-direction in the sensitive volume of the DIG. The individual subvolumes can be seen.

The average per-bit SEU rates calculated for a simulation of 250 MeV protons at 60°

with and without a target and 0° with a target in the DIG are presented in table 4.3.

			DIG
SEU/bit at	60°	without target	$2.143(53) \cdot 10^{-10}$
		with target	$1.455(497) \cdot 10^{-10}$
	0°	with target	$2.250(221) \cdot 10^{-11}$

Table 4.3: Calculated SEU per bit rates in the DIG for simulations at 60° without a target and at 60° and 0° with a target in the beam line.

Multiplying these rates by the number of bits for the component of interest, found in the first row of table 4.4, leads to the total SEU rates in rows 2-4 of table 4.4.

			DIG
		Nr. of bits	144 kbit
SEUs at	60°	without target	$3.09 \cdot 10^{-5}$
		with target	$2.09 \cdot 10^{-5}$
	0°	with target	$3.24 \cdot 10^{-6}$

Table 4.4: The amount of bits in the FPGA used in the DIG and the calculated SEU rates for a 60° beam angle, as well as for the benchmark simulation of an angle of 0° with a target for 250 MeV protons and normalized to 3×10^{10}primary particles.

As with the Controller, the SEU rates for the components in the DIG in table 4.2 might be an overestimation, due to the conservative approaches taken. Even if this is correct, the SEU rate at 60° and no target is approximately 10 times higher than for the benchmark case of 0° and no target.
When comparing the simulations with a target, the rate for the 60° simulation is about six times as high as for the 0° case. Even if no SEUs are observed with a 0° beam angle in practice, the increased risk might lead to SEUs at the new angle.

Fast Controller Real-Time

As with the other two ROIs, figure 4.12 shows the comparison of the fluences obtained by simulations at different beam angles. Using this fluence, the per-bit SEU rates are calculated. In this ROI the HEHeq fluence for a simulation without a target and a beam angle of 52.5° is higher than for the 60° simulation without a target. This might be due to the scattering happening inside the water target. Figure 4.13 presents the gradient of the HEHeq fluence (fig.4.13a) and the THN fluence (fig.4.13b) in the FCRT. The individual values in the cells are obtained by averaging over all bins in the direction not shown in the plot.

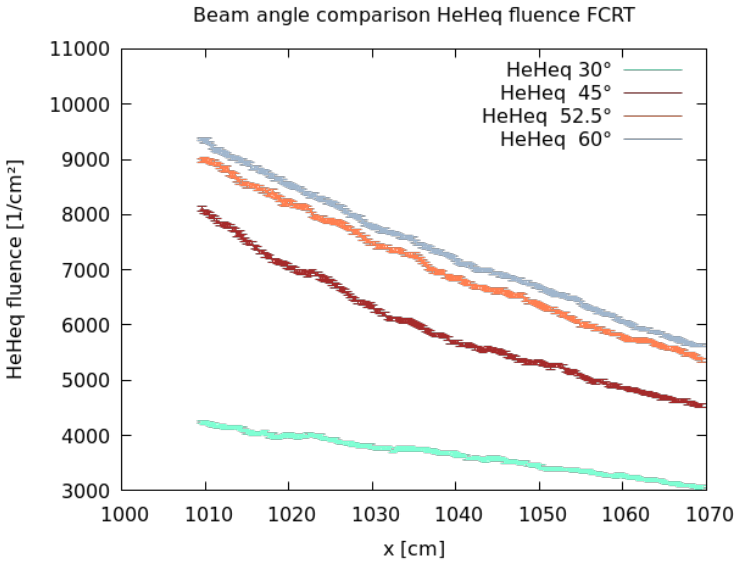

Figure 4.12: Comparison of the HEHeq fluence for beam angles of 30°, 45°, 52.5° and 60° in the x-direction in the sensitive volume of the FCRT without a target.

(a) HeHeq fluence

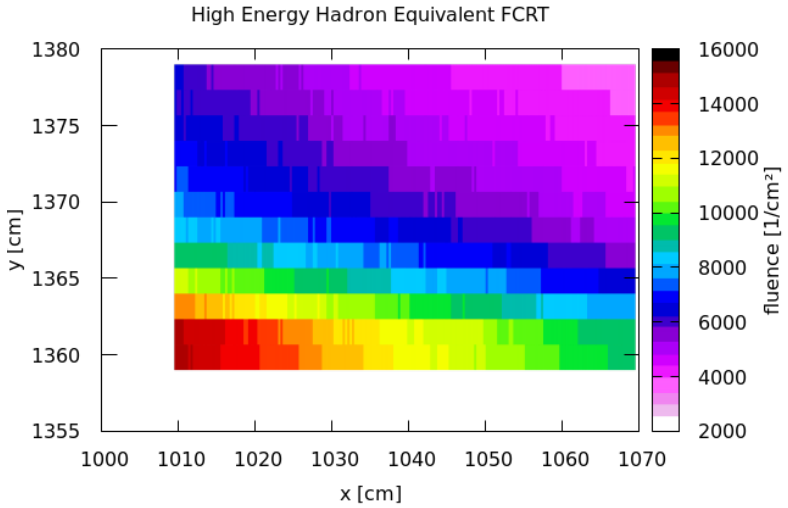

(b) THN fluence

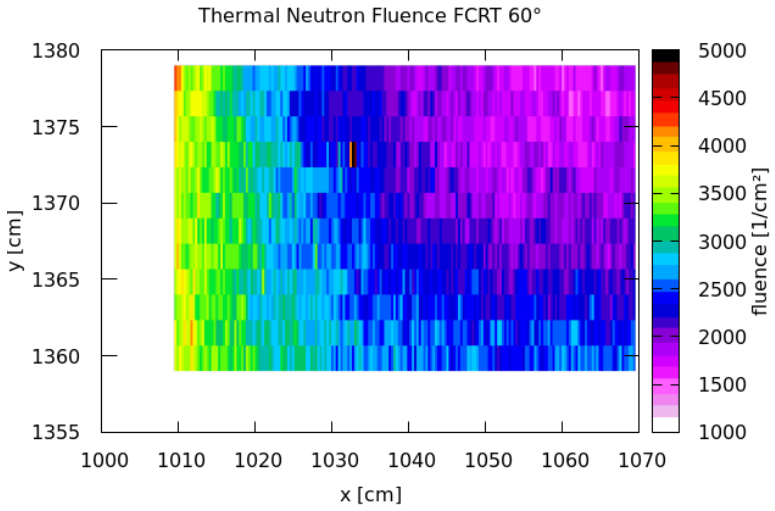

Figure 4.13: 2D plots of the (a) HEHeq and (b) THN fluence for beam angles of $60°$ without a water target in the $x-y$-direction in the sensitive volume of the FCRT. The individual subvolumes can be seen.

The calculated average per-bit SEU rates obtained for a simulation of 250 MeV beam at 60° with and without a target and 0° with a target in the FCRT are presented in table 4.5. By multiplying these rates by the number of bits for the component of interest,

			FCRT
SEU/bit at	60°	without target	$2.272(105) \cdot 10^{-10}$
		with target	$1.432(109) \cdot 10^{-10}$
	0°	with target	$2.984(523) \cdot 10^{-11}$

Table 4.5: Calculated SEU per bit rates in the FCRT for simulations at 60° without a target and at 60° and 0° with a target in the beam line.

found in the first rows of tables 4.6 and 4.7, leads to the total SEU rates in rows 3-5 of tables 4.6 and 4.7.

			FCRT			
			FPGA PXI-7813	FPGA PXI-7811	FPGA big PXI-6534	FPGA small PXI-6534
Nr. of bits			1728 kbit	720 kbit	393 kbit	327 kbit
SEUs at	60°	without target	$7.85 \cdot 10^{-4}$	$3.27 \cdot 10^{-4}$	$8.93 \cdot 10^{-5}$	$7.43 \cdot 10^{-5}$
		with target	$4.94 \cdot 10^{-4}$	$2.06 \cdot 10^{-4}$	$5.62 \cdot 10^{-5}$	$4.68 \cdot 10^{-5}$
	0°	with target	$1.03 \cdot 10^{-4}$	$4.3 \cdot 10^{-5}$	$1.17 \cdot 10^{-5}$	$9.76 \cdot 10^{-6}$

Table 4.6: The amount of bits in the different FPGAs in the FCRT and the calculated SEU rates for a 60° beam angle at 250 MeV, as well as for the benchmark simulation of an angle of 0° with a target.

			FCRT		
			RAM PXI-6534	i5	RAM
Nr. of bits			536 Mbit	209 kbit	68Gbit
SEUs at	60°	without target	0.24	$4.75 \cdot 10^{-5}$	124.92
		with target	0.15	$2.99 \cdot 10^{-5}$	78.72
	0°	with target	$3.2 \cdot 10^{-2}$	$6.24 \cdot 10^{-6}$	16.41

Table 4.7: The amount of bits in the rest of the components in the FCRT and the calculated SEU rates for a 60° beam angle at 250 MeV, as well as for the benchmark simulation of an angle of 0° with a target.

For the FCRT, the SEU rates for the 'no target' case are higher by a factor of approximately 8, compared to the 0° simulation with a target. In the case of a target in the beam line, the rates are still increased by a factor of approximately 5. Since the FCRT is constructed of many different components, high rates in this ROI might be detrimental to the operation of the beam line at this angle. This slightly increased risk of bit-flips has to be considered in detail by the MDS division at MedAustron when planning for the commissioning of this new angle.

According to the different plots provided in this section, it can be seen that the fluence in the ROIs is highest for a beam angle of 60°. This results in an increased risk of SEUs occurring during operation of the gantry at this angle. The obtained SEU rates for the 60° and no target simulations are higher by a factor of $8 - 10$, compared to the benchmark simulation. Even when using a target in the beam line, the risk is still increased by a factor of approximately $5 - 7$, when comparing the two angles of 0° and 60°.
Now that the impact of the angle on the SEU rate is analyzed, and 60° is identified as the 'worst case' setup regarding SEUs, the influence of another parameter, the particle energy, has to be looked at.

4.2 Single Event Upset Rate versus Beam Energies

According to data collected during the months of June and July of 2022, shown in figure 4.14, the energies most used for clinical application range from 70 MeV to 110 MeV, shown in figure 4.14a. Particle rates for clinical use are defined as particles used between 6 a.m. and 11 p.m. Including QA and other non-clinical uses, the most particles are used with an energy of 60 MeV, around 90 MeV to 100 MeV, 110 MeV, 130 MeV, 200 MeV and 250 MeV, see figure 4.14b. Since simulating all energies would be very time-consuming, a few energies in this range have been picked to present a qualitative overview of the behavior. Five different energies have thus been chosen for simulations, consisting of the highest and lowest used energies in therapy, 250 MeV and 60 MeV and three intermediate energies, 200 MeV, 150 MeV, and 100 MeV. Since an angle of 60° is found as the 'worst case' angle with regards to SEUs in the section 4.1, all these simulations are executed for this 60° beam angle and without a water target in the beam line.

(a) Protons rates for clinical use

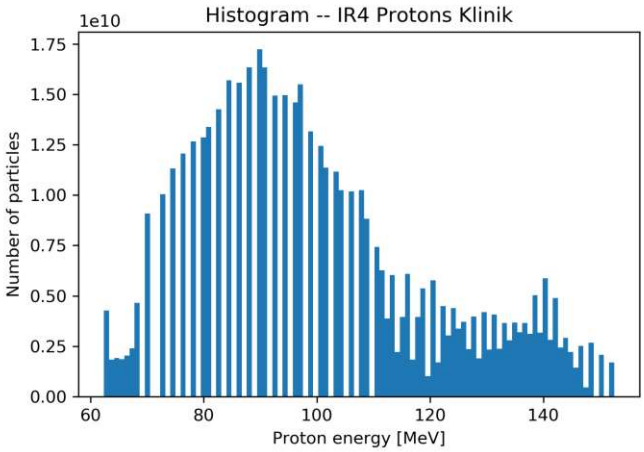

(b) Overall proton rates

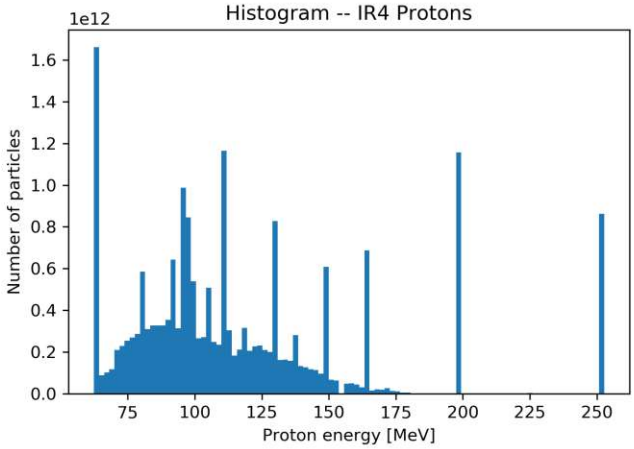

Figure 4.14: The particle rates for (a) clinical and (b) overall use during June to July of 2022. For the clinical rates, only particles used between 6 a.m. and 11 p.m., which are the typical operating hours at MedAustron, are taken into account.

As figure 4.15 demonstrates, the energy has a high impact on the SEU rates as lower energies result in a much lower HEHeq fluence in the ROIs. The HEHeq fluence for 100 MeV protons is already lower by a factor of about 6 than for 250 MeV protons. Resulting from this, operation of the gantry at 60° and energies below 100 MeV, even without a target, should pose no threat to the electronics in the rack.

(a) Controller

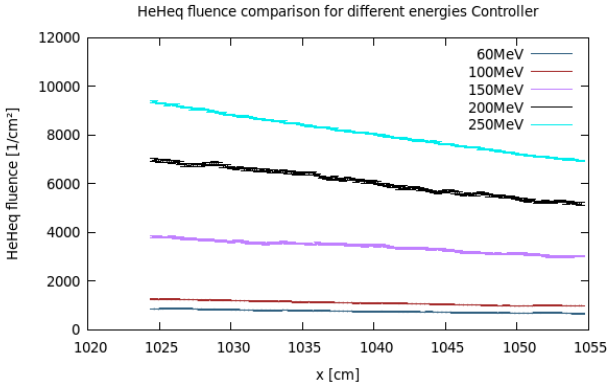

(b) DIG

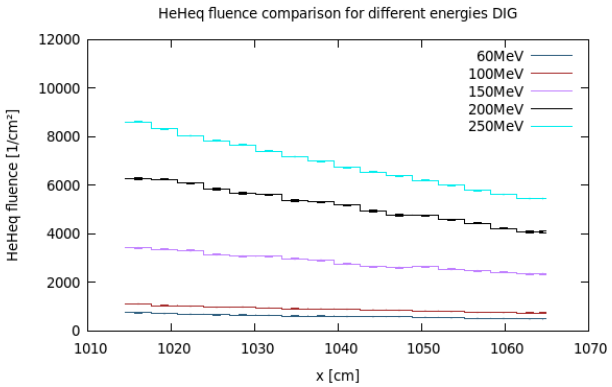

(c) FCRT

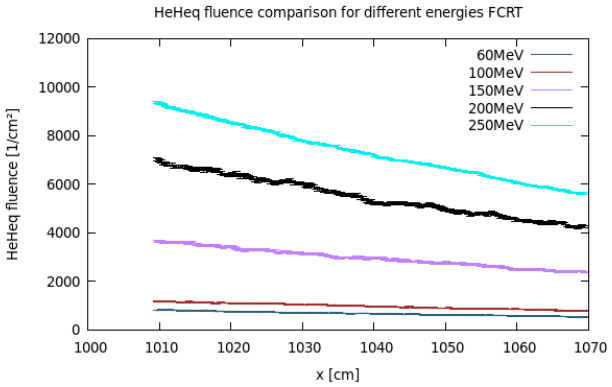

Figure 4.15: Plots of the HEHeq fluence for proton energies of $250\,\mathrm{MeV}$, $200\,\mathrm{MeV}$, $150\,\mathrm{MeV}$, $100\,\mathrm{MeV}$ and $60\,\mathrm{MeV}$ at $60°$ beam angle without a target.

Controller

Based on the HEHeq fluences shown in figure 4.15a, combined with the according THN fluences, per-bit SEU rates for the different energies, 60° beam angle and no target are calculated and listed in table 4.8.

	SEUs/bit
250 MeV	$2.490(103) \cdot 10^{-10}$
200 MeV	$1.871(314) \cdot 10^{-10}$
150 MeV	$1.068(233) \cdot 10^{-10}$
100 MeV	$3.471(478) \cdot 10^{-11}$
60 MeV	$2.397(485) \cdot 10^{-11}$

Table 4.8: The calculated per-bit SEU rates in SV of the Controller for energies of 60 MeV to 250 MeV, normalized to 3×10^{10} primary particles.

By multiplying these rates by the number of bits for the component of interest, found in the first row of table 4.9, the total SEU rates in the rows at each energy are calculated and listed in table 4.9.

		Controller		
		FPGA PXI-7813	i5	RAM
	Nr. of bits	1728 kbit	209 kbit	68Gbit
SEUs at	250 MeV	$8.6 \cdot 10^{-4}$	$5.2 \cdot 10^{-5}$	136.9
	200 MeV	$6.4 \cdot 10^{-4}$	$3.9 \cdot 10^{-5}$	102.85
	150 MeV	$3.69 \cdot 10^{-4}$	$2.23 \cdot 10^{-5}$	58.77
	100 MeV	$1.2 \cdot 10^{-4}$	$7.25 \cdot 10^{-6}$	19.08
	60 MeV	$8.28 \cdot 10^{-5}$	$5.01 \cdot 10^{-6}$	13.18

Table 4.9: The amount of bits in the different components according to their datasheets in the Controller and the calculated SEU rates for 60° beam angle at 250 MeV, 200 MeV, 150 MeV, 100 MeV and 60 MeV primary protons without a target.

Comparing these results to the angular dependence from table 4.2, 60 MeV protons pose the same threat to operation as when using the benchmark setup of 250 MeV protons with a target at 0°, with rates lower by a factor of approximately 10 compared to the 'worst case'. Simulations of 100 MeV protons lead to rates that are lower by a factor of approximately 7, when compared to the 'worst case'. At 200 MeV, SEU rates are lower by a factor of ≈ 1.3 and at 150 MeV by a factor of ≈ 1.8, compared to the SEU rates calculated for the 'worst case', which is still a considerable increase when looking at the rates for the benchmark simulation. Between 100 MeV to 150 MeV a sharp drop-off in the SEU rate is noticed, indicating decreased risk for components at energies below this threshold.

DDS Interlock Gateway

The calculated energy-dependent average per-bit SEU rates for a simulation of a beam at 60° without a target in the DIG are presented in table 4.10.

	SEUs/bit
250 MeV	$2.143(53) \cdot 10^{-10}$
200 MeV	$1.567(154) \cdot 10^{-10}$
150 MeV	$8.815(1144) \cdot 10^{-11}$
100 MeV	$2.848(242) \cdot 10^{-11}$
60 MeV	$1.939(312) \cdot 10^{-11}$

Table 4.10: The calculated per-bit SEU rates in SV of the DIG for energies of 60 MeV to 250 MeV, normalized to 3×10^{10} primary particles.

Multiplying these rates by the number of bits for the component of interest, found in the first row of table 4.11, leads to the total SEU rates at each energy in table 4.11.

	DIG	
	Nr. of bits	144 kbit
SEUs at	250MeV	$3.09 \cdot 10^{-5}$
	200MeV	$2.26 \cdot 10^{-5}$
	150MeV	$1.27 \cdot 10^{-5}$
	100MeV	$4.1 \cdot 10^{-6}$
	60MeV	$2.79 \cdot 10^{-6}$

Table 4.11: The amount of bits in the different components according to their datasheets in the DIG and the calculated SEU rates for a 60° beam angle at 250 MeV, 200 MeV, 150 MeV, 100 MeV and 60 MeV primary protons without a target.

In the DIG, simulations of 100 MeV protons lead to rates that are lower by a factor of approximately 7.5, when compared to the 'worst case'. In general, the comparison of the energy-dependent rates with the angular-dependent rates shows the same behavior as in the Controller. The rate of 2.79×10^{-6} $\frac{\text{SEUs}}{\text{fraction}}$ in the FPGA for 60 MeV protons at

60° is slightly lower than the rate of the benchmark case of $3.24 \times 10^{-6} \frac{\text{SEUs}}{\text{fraction}}$, found in table 4.4. At 200 MeV, SEU rates are lower by a factor of ≈ 1.4 and at 150 MeV by a factor of ≈ 2.4, compared to the 'worst case'. Between 100 MeV to 150 MeV a drop-off of the SEU rate of approximately 3 is calculated.

Fast Controller Real-Time

For the FCRT, the energy-dependent average per-bit SEU rates for a simulation of a beam at 60° without a target are calculated and presented in table 4.12.

	SEUs/bit
250 MeV	$2.272(105) \cdot 10^{-10}$
200 MeV	$1.722(639) \cdot 10^{-10}$
150 MeV	$9.251(2284) \cdot 10^{-11}$
100 MeV	$3.113(479) \cdot 10^{-11}$
60 MeV	$2.141(469) \cdot 10^{-11}$

Table 4.12: The calculated per-bit SEU rates in SV of the DIG for energies of 60 MeV to 250 MeV, normalized to 3×10^{10} primary particles.

These rates are again multiplied by the number of bits for the component of interest, found in the first rows of table 4.13 and 4.14, leading to the total SEU rates in the rows at each energy in table 4.13 and 4.14.

		FCRT			
		FPGA PXI-7813	FPGA PXI-7811	FPGA big PXI-6534	FPGA small PXI-6534
Nr. of bits		1728 kbit	720 kbit	393 kbit	327 kbit
SEUs at	250MeV	$7.85 \cdot 10^{-4}$	$3.27 \cdot 10^{-4}$	$8.93 \cdot 10^{-5}$	$7.43 \cdot 10^{-5}$
	200MeV	$5.95 \cdot 10^{-4}$	$2.48 \cdot 10^{-4}$	$6.77 \cdot 10^{-5}$	$5.63 \cdot 10^{-5}$
	150MeV	$3.2 \cdot 10^{-4}$	$1.33 \cdot 10^{-4}$	$3.64 \cdot 10^{-5}$	$3.03 \cdot 10^{-5}$
	100MeV	$1.08 \cdot 10^{-5}$	$4.48 \cdot 10^{-5}$	$1.22 \cdot 10^{-5}$	$1.02 \cdot 10^{-5}$
	60MeV	$7.4 \cdot 10^{-5}$	$3.08 \cdot 10^{-5}$	$8.42 \cdot 10^{-6}$	$6.99 \cdot 10^{-6}$

Table 4.13: The amount of bits in the different FPGAs according to their datasheets in the FCRT and the calculated SEU rates for a 60° beam angle at 250 MeV, 200 MeV, 150 MeV, 100 MeV and 60 MeV primary protons without a target.

		FCRT		
		RAM PXI-6534	i5	RAM
Nr. of bits		536 Mbit	209 kbit	68Gbit
SEUs at	250MeV	0.24	$4.75 \cdot 10^{-5}$	124.92
	200MeV	0.18	$3.6 \cdot 10^{-5}$	94.7
	150MeV	0.1	$1.93 \cdot 10^{-5}$	50.86
	100MeV	0.03	$6.51 \cdot 10^{-6}$	17.11
	60MeV	0.02	$4.47 \cdot 10^{-6}$	11.77

Table 4.14: The amount of bits in the rest of the components according to their datasheets in the FCRT and the calculated SEU rates for a 60° beam angle at 250 MeV, 200 MeV, 150 MeV, 100 MeV and 60 MeV primary protons without a target.

For the FCRT, the calculated rate at 60 MeV is lower by a factor of ≈ 11 compared to the 'worst case' setup. SEU rates at 200 MeV and 150 MeV are lower than for the 'worst case' by a factor of 1.3 and 2.5 respectively. Between 100 MeV to 150 MeV a sharp drop-off in the SEU rate is happening.
Analyzing these energy-dependent SEU rates shows that an energy of 60 MeV at 60° without a target leads to approximately the same amount of SEUs as the benchmark setup using 250 MeV at 0° with a target.
Energies around 100 MeV, which are mostly used during clinical operation, only provide a slightly increased risk of SEUs, whereas primary particles with energies of 150 MeV and upward bear a significantly higher risk of bit errors, compared to the benchmark simulation.

5 Discussion

Using MC simulations to score the fluence of HEHeq particles and THNs in the sensitive regions of the DDS rack leads to the conclusion that for several possible setups, an increased amount of SEUs has to be expected. Simulating two fundamentally different setups, one containing a target in the beam line and indicating a normal radiation scenario, and one without a target and indicating an accident scenario, shows that SEU rates of a more severe magnitude are expected when using the gantry at 60° without a target and proton energies of 150 MeV and upward, compared to setups already in use.
Since the goal was to get an understanding of the magnitude of SEUs the approach was to identify the gantry angle with the most severe impact first and then check for the influence of the beam energy afterwards. In order to quantify the results and to reduce the number of simulations required, it was decided to compare the rates obtained through simulations without a target with a benchmark setup in which no SEUs are observed in practice. This benchmark setup consists of a 250 MeV proton beam at 0° gantry angle with a water target.
All the plots and tables in chapter 4 indicate a strong dependence of the SEU rate on the beam angle and the primary particle energy. When compared to the benchmark case, the particle fluence in the ROIs is significantly higher for the 'worst case' radiation setup. Using the gantry at the to-be-commissioned angle of 60° with 250 MeV protons and no target results in an up to tenfold increase in SEU rates, significantly increasing the possibility of faults in critical components of the DDS during operation.
As for the primary particle energy as a variable, protons at 60° with energies of 150 MeV and upwards lead to the most notable increase of SEU rates. The calculated SEU rates are higher by a factor of approximately 4-9 in the case of the DIG compared to the benchmark case. Between 100 MeV to 150 MeV a sharp decrease in the fluence and in turn SEU rates is seen, resulting in a fairly low risk of SEUs for primary particles with energies below this threshold.
To present an overview of the relationship between the beam angle, the energy and the per-bit SEU rate, heatmaps, like in figure 5.1, were prepared. They present a convenient way to compare these quantities and provide the possibility of a visual differentiation. Looking at these plots, it can be seen that the SEU rate for all simulated cases is by far lowest for 60 MeV protons at 60°. The rates in the Controller and the DIG at 250 MeV and 52.5° are fairly similar to the SEU rates obtained for protons at 200 MeV and 60°. A steeper gradient of the SEU rate is seen for the variation of the beam energy than for the beam angle.

(a) Controller

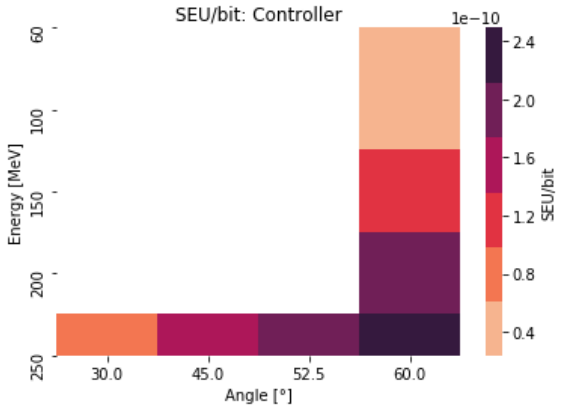

(b) DDS Interlock Gateway (DIG)

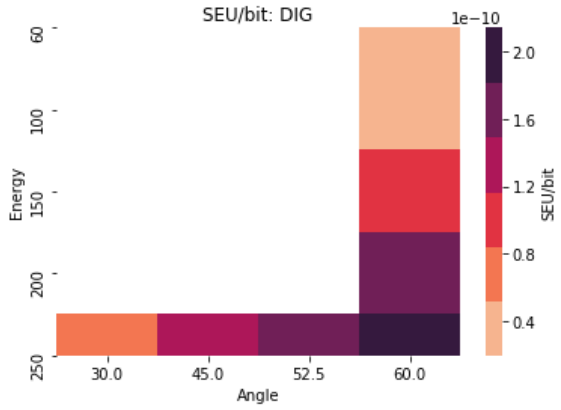

(c) Fast Controller - Real Time (FCRT)

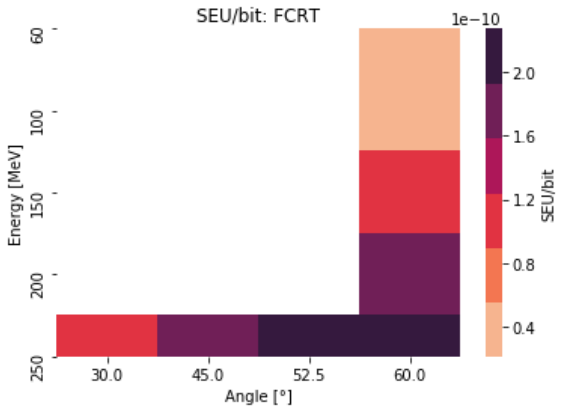

Figure 5.1: Heatmaps showing the relation between primary particle energy, beam angle and the SEU/bit rate for the simulated cases in the three ROIs. The steeper gradient is seen in the variation of the particle energy. All simulations used to obtain these values are executed using no target in the beam line.

In summary, using particles with energies above 150 MeV at the to-be-commissioned angle of 60° leads to a significant increase in the calculated SEU rates and thus an increased risk to the operation of the beam line.

Calculating the SEU rates for 3×10^{10} primary particles per fraction at the highest available energy is a conservative assumption, because a normal treatment would consist of a particle mix with protons at several different energies and angles, adding up to the total number of 3×10^{10} primary particles per fraction. This different composition of the total particle count would lead to SEU rates well below the studied 'worst case' scenario of 3×10^{10} protons per fraction at 250 MeV and 60° without a target. To be able to estimate how much lower the expected SEU rates are compared to the 'worst case' scenario, SEU rates for a typical energy distribution can be calculated. A histogram for the typical energy mix for clinical operation can be seen in figure 5.2a and a histogram for the overall energy mix can be seen in figure 5.2b. Both histograms contain data recorded in June and July of 2022. Using these typical energy distributions, an SEU rate for a more realistic use case can be calculated.
By using the simulated fluences for the energies in the 60 MeV to 150 MeV range, an approximation for the SEU rate for a typical clinical fraction can be calculated by splitting the 3×10^{10} primary particles according to the percentage distribution outlined in figure 5.2a. This leads to an SEU rate resulting from 6×10^9 primary particles at 60 MeV, 1.83×10^{10} primaries at 100 MeV, and 5.7×10^9 primaries at 150 MeV. The calculated per-bit rate in the DIG of such a typical mix is $3.8 \times 10^{-11}\ \frac{\text{SEUs}}{\text{bit}}$. This is lower by a factor of approximately 5.6 compared to $2.143 \times 10^{-10}\ \frac{\text{SEUs}}{\text{bit}}$ for the accident scenario.
Doing the same for the total particle count shown in figure 5.2b leads to a per-bit SEU rate of $5.6 \times 10^{-11}\ \frac{\text{SEUs}}{\text{bit}}$. Compared to the 'worst case', this rate is lower by a factor of approximately 3.8.
These calculations show that a typical irradiation scenario, even as an approximation with fluences obtained at only 60° and without a target, provides a significantly decreased threat to the electronics of the DDS rack compared to the 'worst case'.
To show the insignificance of the obtained rates, an example calculation for the FPGA in the DIG is done. It would take approximately 32360 fractions for one SEU to occur, even when using the 'worst case' setup. At about 30 fractions per day in the IR4, it would take about 1078 days, or almost 3 years, of operation with an accident scenario for an SEU to be noticed. For higher rates, in for example the FPGA in the NI PXI-7813 module of the FCRT with a rate of $7.85 \times 10^{-4}\ \frac{\text{SEUs}}{\text{fraction}}$, it would take about 42 days of radiation in the accident scenario. When considering the particle mix for a sample treatment, this time frame increases to about 245 days of only using an angle of 60° without a target.
The practical significance of an accident scenario is assumed to be rather low. Using the maximum possible energy at the worst possible angle (60°) with no target for a complete fraction can happen once in a while, but is very unlikely to happen repeatedly.

(a) Proton rates, clinical use

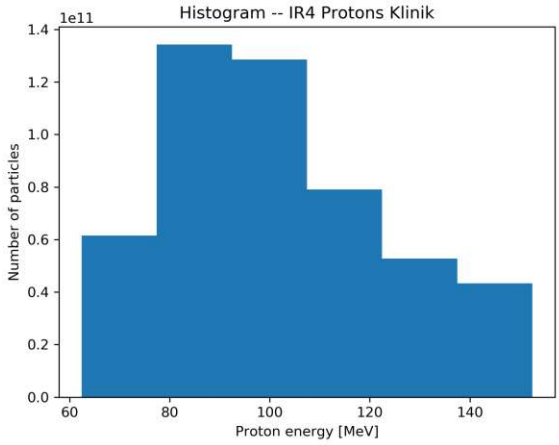

(b) Proton rates, overall

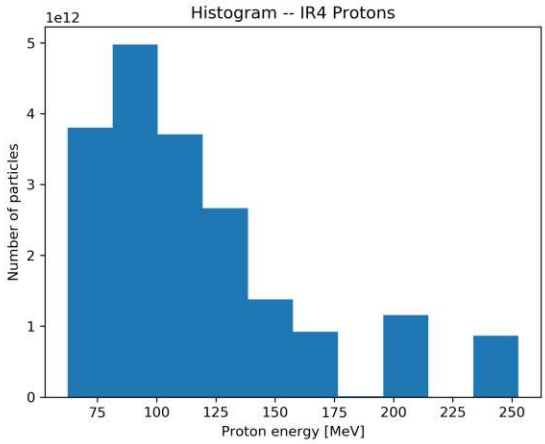

Figure 5.2: Rebinned particle rates for the calculation of the approximate $\frac{\text{SEUs}}{\text{bit}}$ rate for a clinical particle mix and for an overall mix. The rates are obtained for fractions from June to July of 2022. The clinical rates in (a) are recorded between 6 a.m. and 11 p.m.

For example, during a QA session, no target or beam dump may be set up, and test fractions may be performed. Using the beam line for many hours a day allows for great routine during clinical usage. The chances of not having a target in the beam line during clinical operation are slim to nonexistent. A higher chance of not having a target in the beam line is during quality assurance procedures. Higher fluences in the RAM in the

Controller and the FCRT should not pose as big of a threat compared to higher rates in FPGAs, due to most modern RAM being equipped with Error Correction Code (ECC), which is able to detect and correct bit errors in real time. According to a Medical Device Safety (MDS) system architect [10], all the bits in the FPGAs are necessary for reliable operation of the system. This means that for the FPGAs and processors, MedAustron's MDS division must determine whether the obtained rates can have an actual implication on the operation of the beam line with the gantry at this specific angle. If these rates do pose a threat, mitigation measures have to be considered. Relocation of the rack would be a suitable option for SEU mitigation, if somehow possible. Other mitigation measures would include using modules with special radiation-hardened components.

While a comparison of the obtained SEU rates with SEU rates obtained in other theses or publications concerned with this topic would be compelling in order to check for reliability, it is not meaningful. This is due to the completely different setups, geometries, and the level of detail with which the geometry is implemented in. These factors will vary greatly from setup to setup and strongly influence the obtained results.
Given the choice of the SVs for the ROIs, the obtained fluences and thus SEU rates are most likely an overestimation. By having a larger sensitive volume, due to the selection of the volumes representing the whole ROI instead of individual components, even if it is normalized to the volume of these components, more fluence is scored in total. Still, because the purpose of this thesis was to determine the magnitude of the expected SEU rates, a simulation setup with large sensitive volumes for the ROIs was chosen. A more detailed geometry would have reduced the possible number of different scenarios that could be studied because the simulation time increases significantly with the amount of detail. It was expected that, even with conservative assumptions, such as the volumes of the ROI and the maximum energy, the calculated SEU rates would be negligible.
The analysis of the results shows that this is the case, but if even more reliable results are of interest, the geometry can be implemented in greater detail. The simulation of a more detailed geometry would require more precise measurements for the position of the rack and the exact positions of the sensitive components inside the rack. For example, the approximate dimensions of the SV of a RAM are $20\,\mathrm{mm} \times 10\,\mathrm{mm} \times 3\,\mathrm{mm}$, putting the required precision in the mm range. Additionally, the whole geometry of the used NI modules would have to be implemented, including the circuit boards.

6 Conclusion and Outlook

For this thesis, several MC simulations using FLUKA have been conducted in order to score the high energy hadron equivalent (HEHeq) and thermal neutron (THN) fluence in sensitive regions of the DDS rack, namely the regions of the Controller, the DDS Interlock Gateway (DIG) and the Fast Controller - Real Time (FCRT). These components are important parts of the Dose Delivery System used for the proton gantry in irradiation room 4 at MedAustron. Since this system is responsible for steering the beam and cross-checking the dose in real time, it is of interest to understand the risk of experiencing Single Event Upsets (SEUs) in RAM, FPGAs, and processors when using the proton gantry at a new angle of 60°. Since a 'worst case' scenario was of interest, the modified parameters of the simulation are the primary particle energy, ranging from 60 MeV to 250 MeV and the beam angle, from 0° to 60°. For the different energies and beam angles, the fluence in these ROIs varies greatly, showing the highest fluences and thus SEU rates for a setup consisting of 250 MeV primary protons at an angle of 60° without a target in the beam line. To analyze these rates, a benchmark setup of 250 MeV protons at 0° and a target in the beam line, where no SEUs are observed in practice, is used to quantify the calculated rates. The obtained rates for such a 'worst case' are up to approximately 10 times as high as those for the benchmark case, indicating an increased risk of bit errors during operation.
Usually, for the RAM in the ROIs the high fluences should not be as detrimental for operation as for the FPGAs and processors, since they often are equipped with special features that help in detecting and correcting unwanted changes of data. The goal was to get an understanding of the increased risk of the occurrence of SEUs in these sensitive components. The interpretation of the rates and the assessment of the risk are in the hands of the Medical Device Safety (MDS) division of MedAustron. If the obtained rates are deemed too high, further simulations can be conducted with the geometry of the components implemented in greater detail. This will significantly increase the simulation time but will also increase the reliability of the obtained results. Another thing that can be considered are mitigation measures. This would include relocation of the DDS rack as first idea or the use of radiation hardened components in the individual modules. Overall, the assumptions made to decide on the geometry that was used for these simulations revealed a non-negligible risk of SEUs at different angles and energies when compared to the benchmark settings, where, in practice, no SEUs are observed.

Bibliography

[1] M. Stock, D. Georg, A. Ableitinger, A. Zechner, A. Utz, M. Mumot, G. Kragl, J. Hopfgartner, J. Gora, T. Böhlen, L. Grevillot, P. Kuess, P. Steininger, H. Deutschmann, and S. Vatnitsky. "The technological basis for adaptive ion beam therapy at MedAustron: Status and outlook". In: *Zeitschrift f Medizinische Physik* 28 (2018), pp. 196–210. DOI: 10.1016/j.zemedi.2017.09.007.

[2] *Bragg Peak and dose distribution*. https://www.shi.co.jp/industrial/en/product/medical/proton-therapy/what-is-proton-therapy.html. 2022.

[3] M. Durante and H. Paganetti. "Nuclear physics in particle therapy: A review". In: *Reports on Progress in Physics* 79 (2016), p. 096702. DOI: 10.1088/0034-4885/79/9/096702.

[4] D. P. Urschütz. *Hoffnung - Forschung - MedAustron*. https://ag4physik.files.wordpress.com/2015/11/hoffnung-forschung-medaustron.pdf. 2015.

[5] G. Kowarik. *COMMISSIONING OF THE DOSE DELIVERY SYSTEM AT MEDAUSTRON*.

[6] T. P. Ringbæk, U. Weber, A. Santiago, G. Iancu, A. Wittig, L. Grzanka, N. Bassler, R. Engenhart-Cabillic, and K. Zink. "Validation of new 2D ripple filters in proton treatments of spherical geometries and non-small cell lung carcinoma cases". en. In: *Phys. Med. Biol.* 63 (2018), p. 245020.

[7] B. Schaffner. "Proton dose calculation based on in-air fluence measurements". en. In: *Phys. Med. Biol.* 53 (2008), pp. 1545–1562.

[8] V. Giacometti, A. R. Hounsell, and C. K. McGarry. "A review of dose calculation approaches with cone beam CT in photon and proton therapy". In: *Physica Medica* 76 (2020), pp. 243–276. DOI: https://doi.org/10.1016/j.ejmp.2020.06.017.

[9] M. E. Warren Miller. *Cogenda*. https://www.cogenda.com/article/SEE.

[10] DI Dr. Oliver Triebl. *Private conversation about the estimation process using a benchmark simulation*.

[11] P. McLellan. *Single Event Upsets*. https://semiwiki.com/x-subscriber/silvaco/3604-single-event-upsets/.

[12] W. D. Newhauser and R. Zhang. "The physics of proton therapy". In: *Physics in Medicine and Biology* 60 (2015), R155–R209. DOI: 10.1088/0031-9155/60/8/r155.

[13] V. Morisbak and F. Ould-Saada. "Search for New Physics with ATLAS at LHC - Z' dilepton resonance at high mass". In: (2022).

[14] G. Sgouros, W. E. Bolch, A. Chiti, Y. K. Dewaraja, D. Emfietzoglou, R. F. Hobbs, M. Konijnenberg, K. Sjögreen-Gleisner, L. Strigari, T.-C. Yen, and R. W. Howell. "ICRU REPORT 96, Dosimetry-Guided Radiopharmaceutical Therapy". In: *Journal of the ICRU* 21 (2021), pp. 1–212. DOI: 10.1177/14736691211060117.

[15] B. N. Laboratory. *NSRL User Guide: Bragg Curves and Peaks*. https://www.bnl.gov/nsrl/userguide/bragg-curves-and-peaks.php. 2022.

[16] R. A. Gruen. "Impact of tissue specific parameters on the predition of the biological effectiveness for treatment planning in ion beam therapy". RADIOLOGY AND NUCLEAR MEDICINE. PhD thesis. 2014.

[17] J. Ziegler. "The Stopping and Range of Ions in Matter". In: 2–6 (2012). DOI: 10.1016/B978-0-12-780621-1.50005-8.

[18] *Interaction of radiation with matter*. https://radiologykey.com/interaction-of-radiation-with-matter/. 2022.

[19] A. Lechner. "Particle interactions with matter". In: *CERN Yellow Rep. School Proc.* 5 (2018). Ed. by B. Holzer, p. 47. DOI: 10.23730/CYRSP-2018-005.47.

[20] P. E. R. F.R.S. "LXXIX. The scattering of a and ß particles by matter and the structure of the atom". In: *The London, Edinburgh, and Dublin Philosophical Magazine and Journal of Science* 21 (1911), pp. 669–688. DOI: 10.1080/14786440508637080.

[21] H. A. Bethe. "Molière's Theory of Multiple Scattering". In: *Phys. Rev.* 89 (6 1953), pp. 1256–1266. DOI: 10.1103/PhysRev.89.1256.

[22] P. Abratenko. *Evaluating the Performance of Multiple Coulomb Scattering-Based Momentum Reconstruction with MicroBooNE Data*. en. Tech. rep. 2018, FERMILAB–SLIDES–18–136–ND, 1496030. DOI: 10.2172/1496030.

[23] J. I. Dickmann. "Low-dose imaging for particle therapy with fluence-modulated proton computed tomography". 2021.

[24] R. Nave. *Coulomb Barrier for Fusion*. http://hyperphysics.phy-astr.gsu.edu/hbase/NucEne/coubar.html.

[25] V. Zerkin. *Evaluated Nuclear Data File (ENDF)*. https://www-nds.iaea.org/exfor/servlet/E4sMakeE4.

[26] D. Prelipcean. "Comparison between measured radiation levels and FLUKA simulations at CHARM and in the LHC tunnel of P1-5 within the R2E project in Run 2". PhD thesis. 2021. DOI: 10.13140/RG.2.2.20010.13766.

[27] L. Papiez and J. J. Battista. "Radiance and particle fluence". In: *Physics in Medicine and Biology* 39 (1994), pp. 1053–1062. DOI: 10.1088/0031-9155/39/6/011.

[28] INFN. *Advanced FLUKA Course - Materials & Related Scorings*. https://agenda.infn.it/event/20624/contributions/105900/attachments/68621/85097/AdvancedMaterialsScoring2019.pdf.

[29] K. Roed, V. Boccone, M. Brugger, A. Ferrari, D. Kramer, E. Lebbos, R. Losito, A. Mereghetti, G. Spiezia, and R. Versaci. "FLUKA Simulations for SEE Studies of Critical LHC Underground Areas". en. In: *IEEE Transactions on Nuclear Science* 58 (2011), pp. 932–938. DOI: 10.1109/TNS.2010.2097605.

[30] S. Uznanski, B. Todd, A. Dinius, Q. King, and M. Brugger. "Radiation Hardness Assurance Methodology of Radiation Tolerant Power Converter Controls for Large Hadron Collider". In: *Nuclear Science, IEEE Transactions on* 61 (2014), pp. 3694–3700. DOI: 10.1109/TNS.2014.2368149.

[31] M. Cecchetto. "Experimental and Simulation Study of Neutron-Induced Single Event Effects in Accelerator Environment and Implications on Qualification Approach". Presented 13 Apr 2021. 2021.

[32] R. Alia, M. Brugger, S. Danzeca, J. Mekki, and A. Thornton. "SEE cross section calibration and application to quasi-monoenergetic and spallation facilities". In: *EPJ Web of Conferences* 153 (2017), p. 08015. DOI: 10.1051/epjconf/201715308015.

[33] M. Cecchetto, R. Alia, F. Wrobel, M. Tali, O. Stein, G. Lerner, K. Bilko, L. Esposito, C. Bahamonde Castro, Y. Kadi, S. Danzeca, M. Brucoli, C. Cazzaniga, M. Bagatin, S. Gerardin, and A. Paccagnella. "Thermal Neutron Induced SEUs in the LHC Accelerator Environment". In: *IEEE Transactions on Nuclear Science* PP (2020), pp. 1–1. DOI: 10.1109/TNS.2020.2997992.

[34] R. Corp. *Life Data Analysis Reference*. en.

[35] A. Kizilersü, M. Kreer, and A. W. Thomas. "The Weibull distribution". en. In: *Significance* 15 (2018). DOI: 10.1111/j.1740-9713.2018.01123.x.

[36] M. A. Dymova, S. Y. Taskaev, V. A. Richter, and E. V. Kuligina. "Boron neutron capture therapy: Current status and future perspectives". In: *Cancer Commun (Lond)* 40 (2020), pp. 406–421.

[37] K. Hu, Z. Yang, L. Zhang, L. Xie, L. Wang, H. Xu, L. Josephson, S. H. Liang, and M.-R. Zhang. "Boron agents for neutron capture therapy". In: *Coordination Chemistry Reviews* 405 (2020), p. 213139. DOI: 10.1016/j.ccr.2019.213139.

[38] C. Poivey. *RADIATION EFFECTS IN SPACE ELECTRONICS*. en. https://project-cms-rpc-endcap.web.cern.ch/rpc/ChambersandIntegration/Integration/RadiationExposure/TOTAL%20IONIZING%20AND%20NON-IONIZING%20DOSE%20RADIATION%20HARDNESS%20ASSURANCE.pdf.

[39] H. Barnaby and M. Marinella. *Total Ionizing Dose and Displacement Damage Effects in Embedded Memory Technologies*. en.

[40] C. Chong, H. Liu, S. Wang, and X. Wu. "Research on Total Ionizing Dose Effect and Reinforcement of SOI-TFET". en. In: *Micromachines* 12 (2021), p. 1232. DOI: 10.3390/mi12101232.

[41] V. Subert-Maulerova, I. Dawson, M. Moll, A. Himmerlich, and Y. Gurimskaya. *NIEL(non-ionizing energy loss)*. en.

[42] S. Golubov, A. Barashev, and R. Stoller. "1.13 - Radiation Damage Theory". In: *Comprehensive Nuclear Materials*. Ed. by R. J. Konings. Oxford: Elsevier, 2012, pp. 357–391. DOI: 10.1016/B978-0-08-056033-5.00029-X.

[43] F. Salvat-Pujol. "Radiation-induced displacement damage in FLUKA (a very general introduction)". en. In: (), p. 26.

[44] G. H. Kinchin and R. S. Pease. "The Displacement of Atoms in Solids by Radiation". In: *Reports on Progress in Physics* 18 (1955), pp. 1–51. DOI: 10.1088/0034-4885/18/1/301.

[45] M. J. Norgett, M. T. Robinson, and I. M. Torrens. "A proposed method of calculating displacement dose rates". In: *Nuclear Engineering and Design* 33 (1975), pp. 50–54. DOI: 10.1016/0029-5493(75)90035-7.

[46] *AN-600 Understanding Latch-Up in Advanced CMOS Logic*. en.

[47] *Help: Single event upsets*. https://www.spenvis.oma.be/help/background/creme/creme.html.

[48] *SEECA - Section 4*. https://radhome.gsfc.nasa.gov/radhome/papers/seeca4.htm.

[49] S. Buchner and D. McMorrow. "Overview of Single Event Effects". en. In: . *Environments* (2015), p. 79.

[50] *PHYSICS, VOLUME 2, 5TH ED*. Wiley India Pvt. Limited, 2007.

[51] S. Parker. *McGraw-Hill Encyclopedia of Physics*. Henley Management. McGraw-Hill, 1993.

[52] M. A. Islam. "Einstein–Smoluchowski Diffusion Equation: A Discussion". In: *Physica Scripta* 70 (2004), pp. 120–125. DOI: 10.1088/0031-8949/70/2-3/008.

[53] W. Shockley and W. T. Read. "Statistics of the Recombinations of Holes and Electrons". In: *Phys. Rev.* 87 (5 1952), pp. 835–842. DOI: 10.1103/PhysRev.87.835.

[54] T. Ayalew. "SiC semiconductor devices technology, modeling and simulation". PhD thesis. 2004.

[55] M. M. Mano, C. R. Kime, and T. Martin. *Logic and computer design fundamentals*. en. Fifth Edition. Boston: Pearson, 2016.

[56] Y. Aguiar, A. Zimpeck, and C. Meinhardt. "Reliability Evaluation of Combinational Circuits from a Standard Cell Library". In: 2016.

[57] F. L. Kastensmidt. *SEE Mitigation Strategies for Digital Circuit Design Applicable to ASIC and FPGAs*. en.

[58] M. E. Warren Miller. *In Space No One Can Hear Electronics Scream*. https://eu.mouser.com/applications/space-hear-electronics-scream/.

[59] A. Jilani, D. Sharma, and R. Naaz. "Single Event Upset". In: 2021.

[60] K. Xi, C. Geng, Z.-G. Zhang, M.-D. Hou, Y.-M. Sun, J. Luo, T.-Q. Liu, B. Wang, B. Ye, Y.-N. Yin, and J. Liu. "Monte Carlo predictions of proton SEE cross-sections from heavy ion test data". en. In: *Chinese Physics C* 40 (2016), p. 066001. DOI: 10.1088/1674-1137/40/6/066001.

[61] P. Caron, C. Inguimbert, L. Artola, F. Bezerra, and R. Ecoffet. "New SEU Modeling Method for Calibrating Target System to Multiple Radiation Particles". en. In: *IEEE Transactions on Nuclear Science* 67 (2020), pp. 44–49. DOI: 10.1109/TNS.2019.2953995.

[62] E. Pedroni, R. Bearpark, T. Böhringer, A. Coray, J. Duppich, S. Forss, D. George, M. Grossmann, G. Goitein, C. Hilbes, M. Jermann, S. Lin, A. Lomax, M. Negrazus, M. Schippers, and G. Kotrle. "The PSI Gantry 2: a second generation proton scanning gantry". In: *Zeitschrift für Medizinische Physik* 14 (2004), pp. 25–34. DOI: 10.1078/0939-3889-00194.

[63] M. Stock, P. Georg, R. Mayer, T. Böhlen, and S. Vatnitsky. "Development of Clinical Programs for Carbon Ion Beam Therapy at MedAustron". In: *International Journal of Particle Therapy* 2 (2015). DOI: 10.14338/IJPT-15-00022.1.

[64] M. Benedikt and A. Wrulich. "MedAustron—Project overview and status". In: *The European Physical Journal Plus* 126 (2011), p. 69.

[65] E. Pedroni, D. Meer, C. Bula, S. Safai, and S. Zenklusen. "Pencil beam characteristics of the next-generation proton scanning gantry of PSI: design issues and initial commissioning results". en. In: *Eur. Phys. J. Plus* 126 (2011), p. 66. DOI: 10.1140/epjp/i2011-11066-0.

[66] A. Koschik. "The MedAustron Proton Gantry". en. In: (2012), p. 3.

[67] W. Petra. *Fotokatalog IRRADIATION ROOMS 2022*. https://insider.medaustron.at/pr/SiteAssets/SitePages/PR%20Bibliothek/Fotokatalog_IRRADIATION%20ROOMS_2022_small.pdf.

[68] S. Giordanengo, M. A. Garella, F. Marchetto, F. Bourhaleb, M. Ciocca, A. Mirandola, V. Monaco, M. A. Hosseini, C. Peroni, R. Sacchi, R. Cirio, and M. Donetti. "The CNAO dose delivery system for modulated scanning ion beam radiotherapy". In: *Med Phys* 42 (2015), pp. 263–275.

[69] S. A. Dupree and S. K. Fraley. *A Monte Carlo Primer: A Practical Approach to Radiation Transport*. en. Google-Books-ID: EJsACAAAQBAJ. Springer Science & Business Media, 2012.

[70] Y. e. a. Liang. "A general-purpose Monte Carlo particle transport code based on inverse transform sampling for radiotherapy dose calculation". In: *Scientific Reports* 10 (2020), p. 9808. DOI: 10.1038/s41598-020-66844-7.

[71] F. Verhaegen and J. Seco. *Monte Carlo Techniques in Radiation Therapy: Introduction, Source Modelling and Patient Dose Calculations*. en. 2nd ed. Boca Raton: CRC Press, 2021. DOI: 10.1201/9781003211846.

[72] G. Battistoni, T. Boehlen, F. Cerutti, P. W. Chin, L. S. Esposito, A. Fassò, A. Ferrari, A. Lechner, A. Empl, A. Mairani, A. Mereghetti, P. G. Ortega, J. Ranft, S. Roesler, P. R. Sala, V. Vlachoudis, and G. Smirnov. "Overview of the FLUKA code". In: *Annals of Nuclear Energy* 82 (2015). Joint International Conference on Supercomputing in Nuclear Applications and Monte Carlo 2013, SNA + MC 2013. Pluri- and Trans-disciplinarity, Towards New Modeling and Numerical Simulation Paradigms, pp. 10–18. DOI: 10.1016/j.anucene.2014.11.007.

[73] G. Battistoni, T. Boehlen, F. Cerutti, P. W. Chin, L. S. Esposito, A. Fassò, A. Ferrari, A. Lechner, A. Empl, A. Mairani, A. Mereghetti, P. G. Ortega, J. Ranft, S. Roesler, P. R. Sala, V. Vlachoudis, and G. Smirnov. "Overview of the FLUKA code". In: *Annals of Nuclear Energy* 82 (2015). Joint International Conference on Supercomputing in Nuclear Applications and Monte Carlo 2013, SNA + MC 2013. Pluri- and Trans-disciplinarity, Towards New Modeling and Numerical Simulation Paradigms, pp. 10–18. DOI: 10.1016/j.anucene.2014.11.007.

[74] F. Ballarini et al. "The FLUKA Code: an Overview". In: *"J. Phys. Conf. Ser."* "41" (2006). Ed. by R. C. Johnson, "151–160". DOI: 10.1088/1742-6596/41/1/014.

[75] R. J. Glauber. *High-energy collision theory*. Singapore: World Scientific, 1987.

[76] R. J. "Glauber and G. Matthiae. "High-energy scattering of protons by nuclei". In: *"Nucl. Phys. B"* 21 (1970), pp. 135–157. DOI: 10.1016/0550-3213(70)90511-0.

[77] M. Anselmino, E. Predazzi, S. Ekelin, S. Fredriksson, and D. B. Lichtenberg. "Diquarks". In: *Rev. Mod. Phys.* 65 (4 1993), pp. 1199–1233. DOI: 10.1103/RevModPhys.65.1199.

[78] L. Bertocchi. "Graphs and glauber". In: *Il Nuovo Cimento A (1965-1970)* 11 (1972), pp. 45–62. DOI: 10.1007/BF02722777.

[79] V. N. "Gribov. "Interaction of gamma quanta and electrons with nuclei at high-energies". In: *Zh. Eksp. Teor. Fiz.* 57 (1969), pp. 1306–1323.

[80] V. N. Gribov. "Glauber corrections and the interaction between high-energy hadrons and nuclei". In: *Sov. Phys. JETP* 29 (1969), pp. 483–487.

[81] A. Ferrari and P. R. Sala. *The physics of high energy reactions*. Singapore: World Scientific, 1998.

[82] A. "Ferrari, P. R. Sala, A. Fasso, and J. Ranft. "FLUKA: A multi-particle transport code (Program version 2005)". In: (2005). DOI: 10.2172/877507.

[83] A. Koning and H. Akkermans. "PRE-EQUILIBRIUM NUCLEAR REACTIONS: An introduction to classical and quantum-mechanical models". In: 1999.

[84] M. Blann. "Hybrid Model for Pre-Equilibrium Decay in Nuclear Reactions". In: *Phys. Rev. Lett.* 27 (6 1971), pp. 337–340. DOI: 10.1103/PhysRevLett.27.337.

[85] M. Blann. "Importance of the Nuclear Density Distribution on Pre-equilibrium Decay". In: *Phys. Rev. Lett.* 28 (12 1972), pp. 757–759. DOI: 10.1103/PhysRevLett.28.757.

[86] M. Blann and H. K. Vonach. "Global test of modified precompound decay models". In: *Phys. Rev. C; (United States)* 28:4 (1983). DOI: 10.1103/PhysRevC.28.1475.

[87] M. Blann. "Precompound analyses of spectra and yields following nuclear capture of stopped π^-". In: *Phys. Rev. C* 28 (4 1983), pp. 1648–1662. DOI: 10.1103/PhysRevC.28.1648.

[88] V. Weisskopf. "Statistics and Nuclear Reactions". In: *Phys. Rev.* 52 (4 1937), pp. 295–303. DOI: 10.1103/PhysRev.52.295.

[89] A. Ferrari, J. Ranft, S. Roesler, and P. R. Sala. "Cascade particles, nuclear evaporation, and residual nuclei in high energy hadron-nucleus interactions". In: (1995). DOI: 10.48550/ARXIV.NUCL-TH/9509039. arXiv: nucl-th/9509039 [nucl-th].

[90] V. Vlachoudis. *flair for FLUKA*. http://www.fluka.org/flair/.

[91] P. Saracco and M. Pia. "Progress with Uncertainty Quantification in generic Monte Carlo simulations". In: *2013 IEEE Nuclear Science Symposium and Medical Imaging Conference (2013 NSS/MIC)*. 2013, pp. 1–6. DOI: 10.1109/NSSMIC.2013.6829453.

[92] CERN. *Uncertainty quantification in generic Monte Carlo Simulation: a mathematical framework*. https://indico.cern.ch/event/284391/contributions/646540/attachments/525477/724684/CERNPresentation20131125.pptx.

[93] INFN. *Advanced FLUKA Course - Introduction to Monte Carlo*. https://indico.cern.ch/event/923742/contributions/3897685/attachments/2052323/3440361/02_Introduction_to_Monte_Carlo_2020_online.pdf.

Appendix

Here some of the 2D fluence plots for the three ROIs for different angles are presented.

Controller

(a) HEHeq fluence for 30°

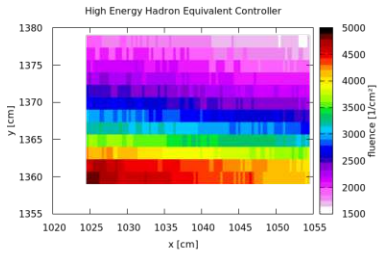

(b) THN fluence for 30°

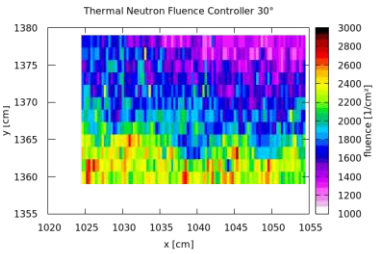

(c) HEHeq fluence for 45°

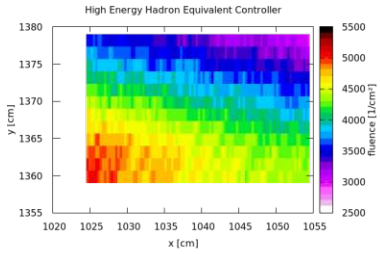

(d) THN fluence for 45°

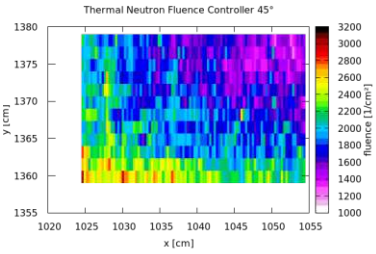

(e) HEHeq fluence for 52.5°

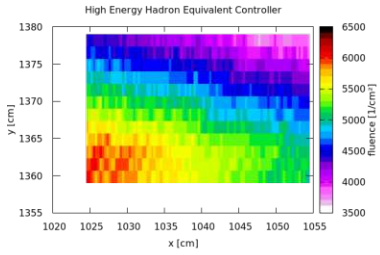

(f) THN fluence for 52.5°

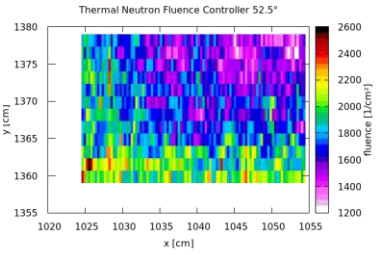

Figure A.1: 2D Plots of the fluence for angles of 30°, 45°, and 52.5° in the Controller.

DDS Interlock Gateway

(a) HEHeq fluence for $30°$

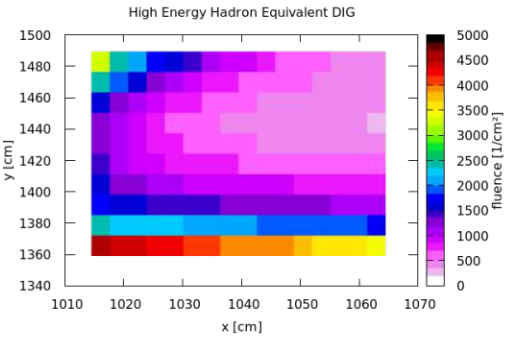

(b) THN fluence for $30°$

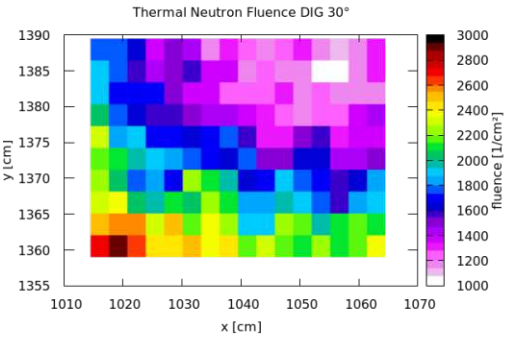

(c) HEHeq fluence for $45°$

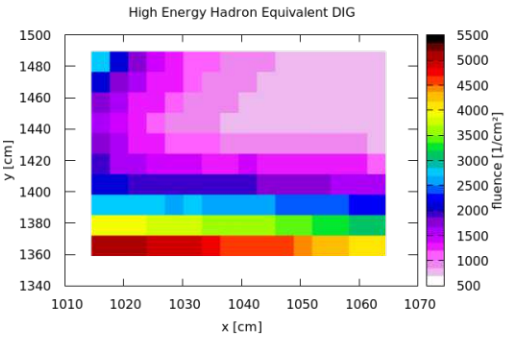

(d) THN fluence for $45°$

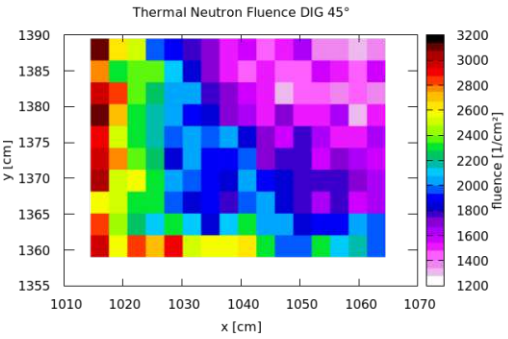

(e) HEHeq fluence for $52.5°$

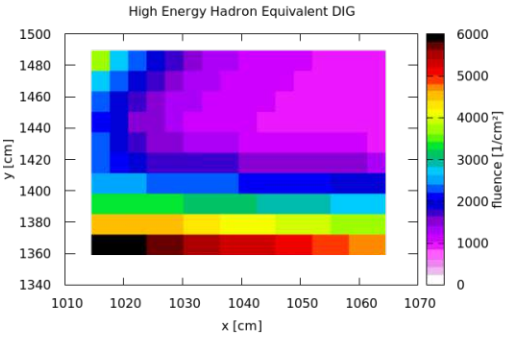

(f) THN fluence for $52.5°$

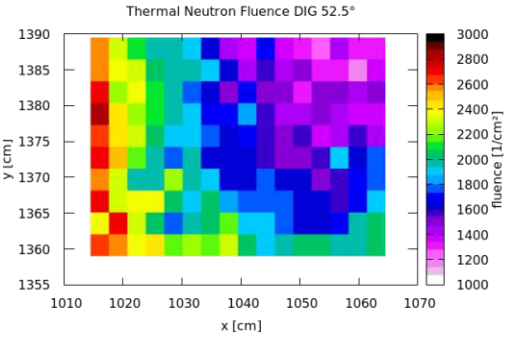

Figure A.2: 2D Plots of the fluence for angles of $30°$, $45°$, and $52.5°$ in the DIG.

Fast Controller Real Time

(a) HEHeq fluence for $30°$

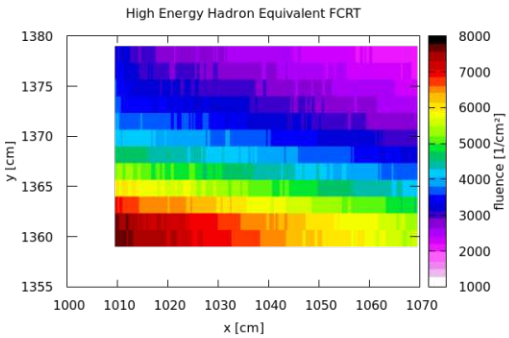

(b) THN fluence for $30°$

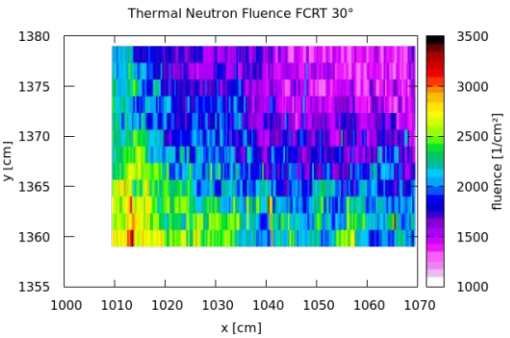

(c) HEHeq fluence for $45°$

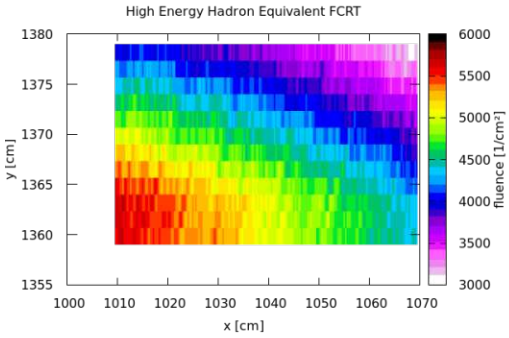

(d) THN fluence for $45°$

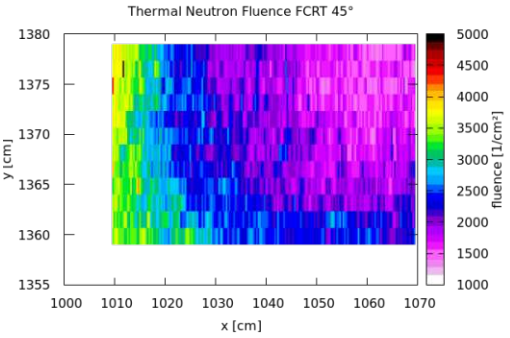

(e) HEHeq fluence for $52.5°$

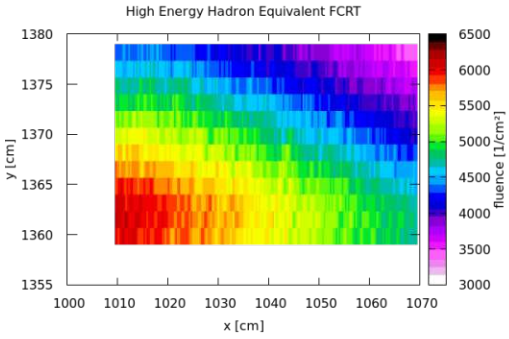

(f) THN fluence for $52.5°$

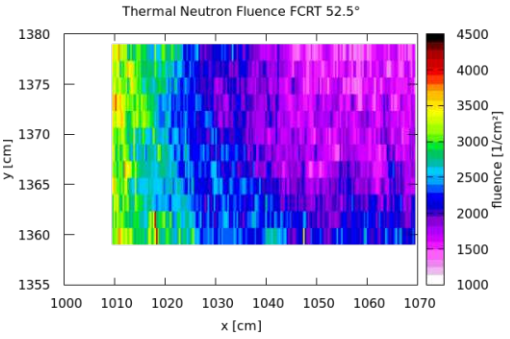

Figure A.3: 2D Plots of the fluence for angles of $30°$, $45°$, and $52.5°$ in the FCRT.

List of Figures

List of Tables

List of Acronyms

MC Monte Carlo

ROI region of interest

SEE Single Event Effect

SEU Single Event Upset

SEL Single Event Latchup

SET Single Event Transient

TID total ionizing dose

SV sensitive volume

FPGA field programmable gate array

RAM random access memory

SRAM static RAM

PCB printed circuit board

MAPTA MedAustron Particle Therapy Accelerator

LINAC linear accelerator

DDS Dose Delivery System

FLUKA FLUktuierende KAskade

THN thermal neutron

HEH high energy hadron

IN intermediate energy neutron

HEHeq high energy hadron equivalent

LET linear energy transfer

ECR electron cyclotron resonance

IR irradiation room

IR4 irradiation room 4

CERN European Organisation for Nuclear Research

INFN Italian Institute for Nuclear Physics

RPP Rectangular Parallelpiped

rad radiation absorbed dose

DD displacement damage

NIEL non-ionizing energy loss

DPA displacement per atom

MOSFET metal-oxide semiconductor field-effect transistor

NMOS n-channel

PMOS p-channel

ICRU International Commission on Radiological Units and Measurements

flair FLuka Advanced InteRface

DIG DDS Interlock Gateway

FCRT Fast Controller - Real Time

MCNP Monte Carlo N-Particle Transport Code

Geant4 GEomentry ANd Tracking 4

PHITS Particle and Heavy Ion Transport Code System

ECC Error Correction Code

MDS Medical Device Safety

LEBT Low Energy Beam Transfer

MEBT Medium Energy Beam Transfer

HEBT High Energy Beam Transfer

CDF cumulative distribution function

ENDF Evaluated Nuclear Data File

INC IntraNuclear Cascade

(G)INC (Generalized) IntraNuclear Cascade

NI National Instruments

PET positron emission tomography

MDR Medical Device Regulation

RP radiation protection

CSDA continuous slowing down approximation

SBOP spread out Bragg peak

CH condensed history